# NON-CONTACT PHYSIOLOGICALLY RELATED MOTION SENSING WITH ULTRA-WIDEBAND IMPULSE RADAR

A Dissertation
Presented to
The Academic Faculty

By

Van Nguyen

In Partial Fulfillment
of the Requirements for the Degree
Doctor of Philosophy in the
School of Electrical and Computer Engineering

Georgia Institute of Technology

December 2016

**NON-CONTACT PHYSIOLOGICALLY RELATED MOTION SENSING WITH ULTRA-WIDEBAND IMPULSE RADAR**

Approved by:

Dr. Mary Ann Weitnauer, Advisor
School of Electrical and Computer Engineering
*Georgia Institute of Technology*

Dr. Aaron D. Lanterman
School of Electrical and Computer Engineering
*Georgia Institute of Technology*

Dr. Brani Vidakovic
School of Industrial and Systems Engineering, and Department of Biomedical Engineering
*Georgia Institute of Technology*

Dr. David V. Anderson
School of Electrical and Computer Engineering
*Georgia Institute of Technology*

Dr. Omer T. Inan
School of Electrical and Computer Engineering
*Georgia Institute of Technology*

Date Approved: November 1, 2016

To my Parents.

## ACKNOWLEDGEMENTS

I would like to express my deepest gratitude to my advisor, Dr. Mary Ann Weitnauer, without whose tremendous help and support I would not have the opportunities I have today.

My special thanks go to the members of my thesis committee, Dr. Brani Vidakovic, Dr. Aaron D. Lanterman, Dr. David V. Anderson, and Dr. Omer T. Inan, for their insightful comments and questions.

I also express my appreciation to Vietnam Education Foundation and Sensiotec Inc. for their partial financial support. I thank Dr. Davis Pan for everything he taught me during my internships at Bose Corporation.

Thanks to all my labmates and friends from Centergy, who have been so kind helping me through this journey and from whom I have learned so much. I thank Dr. Abdul Q. Javaid and Philippe Laban for their fruitful collaboration. Thank you, Dr. Zubin Mevawalla.

To my Mom and sisters, thank you all for having been great support for me during this journey. To my late Dad, we have not met since I was four, but I have never stopped feeling your love and pride in me, and during difficult times thinking of you gave me strength. Finally, I would like to take the opportunity to thank all my teachers and staff at Georgia Tech.

## TABLE OF CONTENTS

## LIST OF TABLES

## LIST OF FIGURES

## SUMMARY

Impulse Radio Ultrawideband (IR-UWB) radar is a promising tool for non-contact, non-invasive sensing of physiological parameters, which could be valuable in identifying or preventing clinical disorders. This research investigates the use of IR-UWB radar in monitoring of physiological parameters, e.g. respiration rate, heart rate, and cardiopulmonary chest wall displacement. The dissertation has two major parts. The first part consists of novel theoretical analysis of the radar received signal due to arbitrary periodic displacement patterns of the heart and lungs. To the best of the author's knowledge, this is the first reported analytical model on the analog radar received signal as it arrives at the received antenna, i.e., before any processing, such as sampling. Closed-form expressions of the complex amplitudes and frequency locations of the spectral components are derived. The analysis shows that the received spectrum contains clusters that are not just scaled versions of each other; rather they have complex variations that if measurable, could enable estimation of parameters such as displacement amplitude; such variations are not apparent in the existing aliased spectrum model, which has just one cluster. The degree to which existing models for an aliased version of the received spectrum differ from the author's model is analyzed. Some practical aspects of the spectral model, such as the number of significant components in a spectral cluster and computational complexity of the theoretical model are investigated.

The second part consists of algorithm development, where estimation methods are developed to estimate a range of physiological parameters. In particular, for heart rate detection, estimation algorithms ranging from heuristic regime to sequential Bayesian filtering have been developed, leveraging HR harmonics, tracking, and motion artifact removal. The performance of these algorithms are evaluated with real-world experimental data from human subjects lying on a bed with an under-the-mattress UWB radar. The heart rate is the focus of the design of these algorithms, because the heart-related signal is contaminated

by interference from the stronger respiration rate harmonics, noise, and other un-modeled phenomena in the system. On the other hand, respiration-related signal is stronger and free from interference from the heart rate harmonics, thus it is a simple task to estimate respiration rate.

This research is also concerned with the reconstruction of the chest wall displacement from the IR-UWB radar signal. There are several novel aspects of the proposed method. First, only a tiny fraction of the bandwidth of the received spectrum is needed to reconstruct the entire displacement pattern. Since only a tiny fraction of the UWB bandwidth needs to be retained, the required sampling rate is substantially reduced. This is a significant advantage over the commonly used time-domain correlation method, where sub-nanosecond or even sub-picosecond sampling period is needed to retain the pulse morphologies to feed into the correlator to compute the pulse delays, thereby deriving the displacement. Second, the maximum likelihood estimator of the displacement is investigated, and the Cramér-Rao lower bound is derived. Third, in order to further improve estimation accuracy, a denoising method such as empirical mode decomposition is applied on the maximum likelihood estimates.

In addition, a method that quantifies body-macro movement, such as limb movement, and detects a posture change has been developed in this dissertation. The method is set up as a hypothesis test, where the decision threshold between the null and alternative hypotheses are calculated from statistics obtained from experimental data.

# CHAPTER 1
# INTRODUCTION

## 1.1 Importance of monitoring of physiological parameters

Continuous at-home monitoring of physiological parameters is valuable and in demand, especially for the increasing aging population. Continuous logging of these parameters can help identify or preventing clinical disorders. A patient's heart rate (HR) and respiration rate (RR) are fundamental vital signs and are essential in identifying clinical disorders; these signs should be monitored consistently and accurately [1]. Chest wall displacement caused by lungs breathing or by motion of the heart inside the thorax while holding breath could help identifying clinical disorders such as obstructive sleep apnea or cardiac malfunctioning. Currently, the most common form of heartbeat monitoring is pulse oximetry, in which a sensor is clipped on the patients finger or ear lobe, and electrocardiography, where multiple adhesive electrodes are placed on the patients skin by a trained technician. Respiration rate is commonly obtained by a nasal cannula or respiration mask. Chest wall displacement is typically measured by a thorax band or an abdomen band, or both. All these methods require some form of attachment to the skin. Attaching sensors to a patient's body for continuous or frequent monitoring restricts movement and can cause discomfort, distress, or pain [2]. Furthermore, some patients, such as burn patients, cannot accept skin attachments, but benefit from continuous vital signs monitoring. Fig. 1.1 shows the most common vital signs monitoring methods.

In addition, motion level, or motion score, and posture change indication could be clinical metrics that helps with prevention of skin ulcer or bed sores development. Skin ulcers are typically developed when the skin is pressed against a surface for a prolonged period of time, thus depriving the blood supply to the tissues. This is a common problem


ECG Pulse oximetry Nasal cannula

Figure 1.1: Most common vital signs monitoring methods.

among bed-ridden patients. To prevent this problem, these patients need to turn, or be turned by a caregiver, frequently. However, the patients or even the caregivers can forget to conduct the needed turns and in the case of immobile patients that solely depend on caregivers, manually logging of turn events is time-consuming and prone to mistakes. Thus, an automatic continuous monitor of motion level and posture change could be valuable for skin ulcer prevention.

## 1.2 What is IR-UWB? Why is it suitable for biomedical applications?

IR-UWB radar is a carrier-free radar technology that emits extremely short pulses. To qualify to be UWB, the signal must have a $10$ dB bandwidth that is at least $20\%$ of the center frequency or at least 500 MHz [3]. The UWB transmit power spectral density limit is $-41.3$ dBm/MHz [3]. The UWB spectrum mask regulated by FCC is shown in Fig. 1.2. Because of its extremely wide bandwidth and extremely low power, IR-UWB transmitters make negligible interference on other types of radio in its band of 3.1 to 10.6 GHz and IR-UWB receivers are very robust to multipath and to interference from other types of radios in this band [3]. IR-UWB is non-ionizing and has the ability to transmit through obstacles like clothes, bed frame, and blankets [4]. Furthermore, it has extremely high temporal resolution. These advantages make IR-UWB particularly well-suited for home health care, emergency room, intensive care units, hospitals, pediatric monitoring, rescue operation,

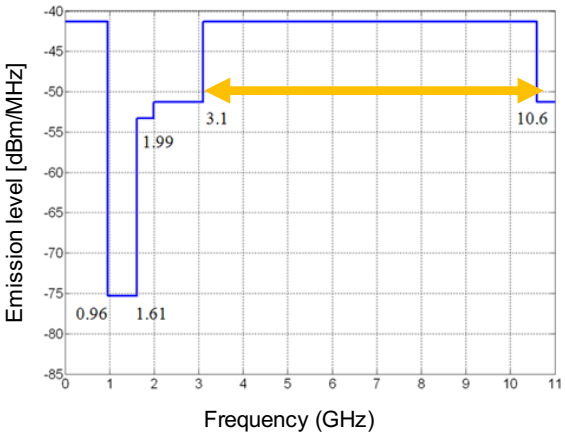


Figure 1.2: IR-UWB spectrum mask

etc. [4].

Impulse Radio Ultra-Wideband (IR-UWB) radar is known to be a safe and promising tool for continuous-time, non-contact, non-invasive measurement of HR and RR. In typical set up, the IR-UWB radar vital signs sensor can be located at a short distance from the patient, such as under a mattress, above a bed, or behind a chair, as shown in Fig. 1.3.

## 1.3 How does it work?

Thanks to its excellent spatial resolution, IR-UWB radar is able to sense, in a non-contact manner, the minute chest movements induced by lungs breathing and heart beating, and thereby produce HR and RR estimates [4, 5, 6, 7, 8, 9, 10, 11]. An IR-UWB system transmits a series of extremely low power and extremely short electromagnetic (i.e., radio) pulses, typically on the order of a nanosecond wide. When these pulses fall on boundaries between materials with different dielectric properties, such as the skin-air interface, the pulses are reflected back to the IR-UWB receiver. The time of arrival of a reflected pulse is related to the round trip distance between the IR-UWB system and the boundary that reflected the pulse. Movements of the interface caused by breathing and heartbeats will induce changes in the round trip propagation delays; hence the radar received signal is delay-modulated. In the frequency domain, spectral components centered at multiples of

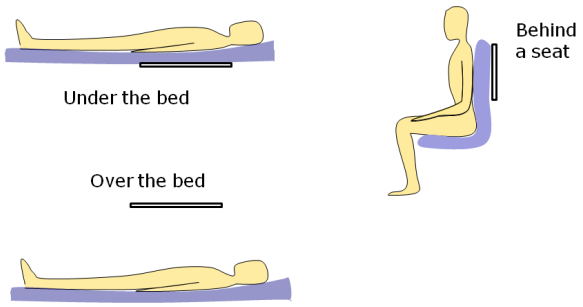


Figure 1.3: Placements of IR-UWB radar in vital signs monitoring.

RR, multiples of HR, and their intermodulation products $m \times \text{RR} + l \times \text{HR}$, where $m, l$ are integers, are present in the spectrum of the radar received signal, as has been shown in the mathematical framework in [12, 9] and experiment results in [9]. This is expected since delay modulation is a type of nonlinear modulation.

## 1.4 Hardware used in the experiments of this thesis

A logical approach is to perform direct sampling on the received waveform and extract the times of arrival through correlation with a reference pulse, thereby estimate the HR and RR [13, 14, 15]. However, this approach is expensive in terms of hardware, memory, and computational complexity, because an extremely high sampling rate (on the order of tens of GHz) is needed. A lower cost, alternative hardware design has been implemented [5], and this is the device used to generate the experimental data for this dissertation. Fig. 1.4 shows a simplified diagram of this radar receiver. A more detailed schematic can be found in Fig. 6 of [5]. The IR-UWB radar signal is first time-gated, to allow radar returns from only the selected span of distances, then down-converted to baseband. The RF front-end comprises several hardware filters including two bandpass filters with passbands of 0.2-0.7 Hz and 0.5-8 Hz for the respiration-related signal and heart-related signal. Each of these two filter outputs is fed into an ADC with sampling rate of 128 Hz. A stream of respiration-related ADC samples and a stream of heart-related ADC samples are obtained.

The narrowband filtering indicates that only a fraction of the UWB signal bandwidth is

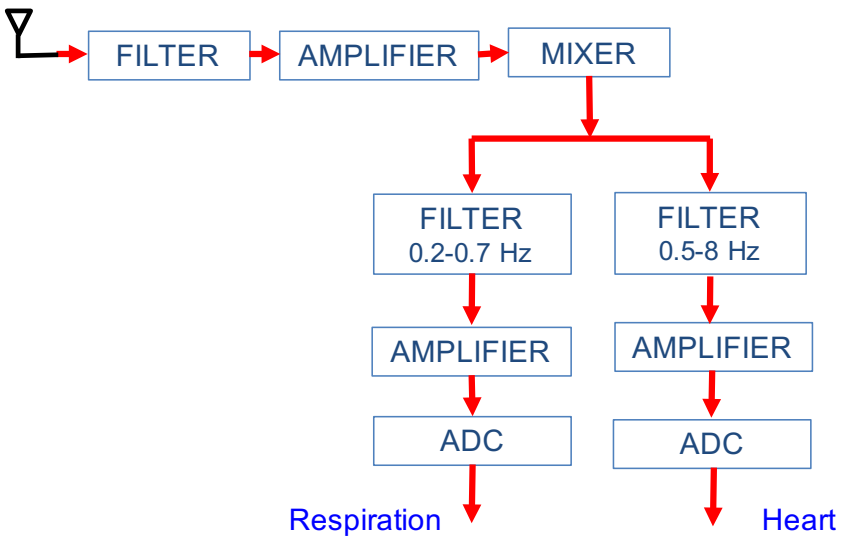


Figure 1.4: Schematic of the UWB radar receiver, simplified from that in[5].

retained. This results in significant reduction in sampling rate, which in turns reduces the hardware cost. The Nyquist criterion is still satisfied for estimation of HR and RR. Since only a fraction of the UWB signal bandwidth is retained, pulse delays cannot be obtained from this system by performing correlation with a reference pulse.

Full characterization of the radar system, including the pulse shape and specifications of some filters, is not available. For the purpose of HR and RR estimation, we have demonstrated that only a fraction of the UWB signal bandwidth is sufficient, both theoretically [12] and experimentally [6, 7].

## 1.5 Scope and organization of the dissertation

In this dissertation, the use of IR-UWB radar in non-contact sensing of physiological parameters is investigated. A summary of the related work is presented in Chapter 2. The dissertation research can be organized into two categories, theoretical modeling and algorithm development, with the emphasis on the latter. In Chapter 3, the first generic theoretical framework for modeling the IR-UWB radar received signal for arbitrary periodic displacement of the reflective interface such as the chest wall is presented.

For algorithm development, a few methods have been designed and implemented to estimate a range of clinical physiological parameters. In Chapter 4, two heuristic HR and RR estimation algorithms are presented. In Chapter 5, sequential Bayesian filtering is applied to the HR estimation problem. A body movement and posture change detector is described in Chapter 6. All these algorithms are evaluated with experimental data. In Chapter 7, morphology of the chest wall displacement is estimated from a tiny fraction of the received bandwidth using maximum likelihood estimation and empirical mode decomposition. The bias and Cramér-Rao lower bound (CRLB) of the maximum likelihood estimator are also analyzed.

# CHAPTER 2
# LITERATURE SURVEY

This chapter contains a review of the literature on the use of IR-UWB radar to extract physiological parameters. This review is organized as follows. Section 2.1 provides an overview of techniques currently used for non-contact or non-invasive vital signs monitoring. The latest work in IR-UWB radar signal modeling is discussed in Section 2.2. In Section 2.3, the state-of-the-art for algorithm development in HR and RR estimation is presented. Current literature on measuring chest displacement morphology is reviewed in Section 2.4. In Section 2.5, recent advances in body movement and posture detection are discussed. Finally, Section 2.6 discusses the challenges that this dissertation addresses.

## 2.1 Techniques for non-contact or non-invasive vital signs monitoring

Many techniques have emerged for continuous and unobtrusive monitoring of physiological signs. Photoplethysmography (PPG) has gained popularity in home healthcare [16]. Contact PPG, whose most popular forms are the pulse oximeter and wrist bands, requires firm attachment to the skin. Non-contact camera-based PPG has been proposed to estimate HR by detecting the subtle temporal variation of the skin color due to heart beating [17, 18, 19, 20] and RR by detecting the subtle skin motion due to breathing [18, 19]. However, this method possesses inherent disadvantages. First, it requires the subject (or part of the subject) being monitored to be well-illuminated, causing inconvenience, especially during sleeping. Second, it requires a line-of-sight between the camera and the part of the subject being monitored. For example a blanket or clothes can easily mask the body's subtle motions due to breathing. Furthermore, this disadvantage prevents the flexibility of sensor locations. Third, privacy is violated.

An acoustics-based method that uses a sensor attached to the chest has been proposed to

extract the RR and other related parameters such as inhale-to-exhale ratio from the breathing sound [21]. Movements of the body caused by respiration and heart beating can also be measured using the Ballistocardiogram (BCG). BCG pressure sensors such as electromagnetic film (EMFi) [22] and micro-bend optic fiber [23] have been used to extract respiration and heart rates from the BCG.

In contrast, radar-based techniques can offer continuous monitoring, in addition to non-invasiveness and non-contact-ness. Doppler radar and UWB are two popular radar technologies for vital signs estimation. UWB has an advantage over Doppler radar techniques in that the former is not only robust against interference from coexisting systems but also causes negligible interference to these systems, because of its extremely low power spectral density. IR-UWB radar has been demonstrated to be a promising candidate for continuous, non-contact, and non-invasive monitoring of vital signs[4, 5, 6, 7, 12, 9, 8, 10, 11, 24, 14, 15, 25, 26].

### 2.2 IR-UWB signal modeling

Three different research groups [8, 9, 10] have derived analytical models of the IR-UWB radar received signal spectrum. The theoretical analysis in [8] shows that the IR-UWB radar signal, delay-modulated by the minute chest movement, contains the RR harmonics, assuming the chest cavity displacement is solely due to breathing. Mabrouk *et al* [10] expand this analytical framework by modeling the pulse-reflecting surface as the sum of both chest and abdomen displacements, resulting in a spectrum model that contains spectral components also at multiples of RR. Lazaro [9] expands the analysis in [8] by also incorporating the heart beating into the overall chest displacement; the resulting spectrum model contains spectral components at multiples of RR, multiples of HR, and their intermods.

However, these models are derived under rather restrictive assumptions. First, these models restrict to one or two sinusoids to model the breathing and heartbeating displacements; these displacement models are quite simplified versions of actual human displace-

ment patterns. Second, the initial phases of all the sinusoids in these displacement models are assumed to be equal and zero at the beginning of the observation. That is, the phases of the sinusoidal breathing-induced displacement and the sinusoidal heart-induced displacement are assumed to be equal and zero [9]; the phase of the chest movement [8] or chest and abdomen displacements [10] due to breathing are also assumed to be zero. In reality, there is no guarantee that, at data acquisition time, the breathing phase is zero and the relative phase of the heart and breathing is zero. A non-zero phase in the displacement model generally introduces an additional sinusoid, and existing analytical models cannot be applied and rederivation is needed. There appears to be no easy way and no guidance from these authors on how to convert the results if the reflecting-surface model changes, e.g., the model is a cosine waveform instead of a sine, or more generally, a non-zero phase is present in the sine(s) in the model, or when the sinusoids do not have equal phase. Thus, when a new pulse delay model is of interest, one generally has to re-derive the expressions in [8, 9, 10]. In contrast, the model proposed in Chapter 3 of this dissertation eliminates these restrictive assumptions by allowing an arbitrary periodic displacement pattern. In addition, this model has final expressions that can be easily modified to accommodate changes.

A few other distinctions between this model and [8, 9, 10] should also be noted. First, the analytical spectrum expressions in [8, 9, 10] are for an *undersampled* version of the radar received signal. Undersampling causes the spectrum to be aliased, and generally the operation is not invertible [27]. In contrast, our model provides the un-aliased spectrum and it will be shown that the aliased and un-aliased spectra are significantly different. Second, the coefficients of the spectral components in [8, 9, 10] do not have closed form expressions, in general. The distinctions between the proposed model of this dissertation and [8, 9, 10] are addressed in more detail in Section 3.3.3.

## 2.3 Estimation of HR and RR

The challenging attributes of vital-signs-bearing signal acquired from non-contact radar sensors require careful algorithm design. Time domain approaches, e.g. peak counting, cycle counting, or zero crossing, are usually used for ECG signal since the beats can be easily identified. For signal with low signal-to-noise ratio or with crosstalk, such as the vital-signs-bearing signal from the non-contact noise-like IR-UWB radar (Fig. 5.2bi,iii) or continuous wave Doppler radar, estimating HR with these approaches is difficult. Frequency-domain method is more suitable for this case and is in fact used by most HR estimation works with radar signal [9, 6, 7, 28, 29, 30, 31, 32].

Most only focus on detecting the heart fundamental peak in the spectrum of the radar received signal and overlook its harmonics [30, 31, 32], where the HR is selected to be the highest peak in a valid HR range. While the RR fundamental can be detected by simply selecting the highest peak in the spectrum, extracting the HR peak faces several challenges. The breathing motion is much stronger than the heart motion in amplitude. Some strong RR harmonics and (possibly) the intermodulation products between HR and RR can fall into the valid HR frequency band and interfere with the HR peak due to "leakage" phenomenon [33]. This interference can cause the HR peak to be displaced, detrimentally attenuated, or even completely canceled. Body movement such as that caused by limbs cause artifacts in the heart and respiration signals. In these cases, the peak-selection HR estimation method will have some error which might become very large if the HR is not the highest peak in the valid HR range.

Several groups have addressed this interference issue by canceling the RR harmonics from the received signal [9, 28] or simply rejecting a frequency candidate to be the HR estimate if it is equal to a RR harmonic [29]. In [9], a harmonic canceller filter is proposed to eliminate the RR harmonics from the IR-UWB radar received signal spectrum. The HR is then selected to be the highest peak over the valid HR range in the "respiration-free"

spectrum. However, such method does not work for certain combinations of the subject's true RR and true HR, as given in detail in [15]. A simple example is when the HR is approximately a multiple of the RR, the HR fundamental (and its next harmonics) will also be cancelled or attenuated together with the respiration harmonics. An alternative method [28] was proposed to cancel RR harmonics from the Doppler radar received signal. The respiration-induced signal is reconstructed with tuning and then subtracted from the original signal. This method requires a relatively long observation time window (100-150 s). In all these works [9, 28, 29], the correct HR will not be detected when HR and RR are harmonically related, a case that is not uncommon.

One alternative solution for the RR interference problem is to exploit the useful information in the HR harmonics. Taking advantage of the harmonics in a spectrum has been shown to be advantageous of identifying the fundamental frequency [34, 35, 6, 7]. Schroeder [34] proposes to construct a harmonic-product spectrum by adding up the logarithmic amplitudes of the harmonics of each fundamental frequency candidate. Similarly, Walmsley [35] defines a harmonic transform that sums the powers of the harmonic. Our earlier path-search algorithms [6, 7] were the first reported algorithms to exploit HR harmonics to improve accuracy of HR estimation from IR-UWB radar signal. HAPA [6] tries to identify a set of three or more consecutive approximately equally spaced spectral peaks, such that their frequencies are approximately an integer multiple of the average inter-peak distance in terms of frequency; that distance of the most powerful path is the HR estimate. However, in some spectra, a path cannot be established due to nonappearance of one or a collection of harmonic peaks because they are masked by noise or interference. The SHAPA algorithm [7] attempts to fix this shortcoming to recover such missing peaks by merging the current spectrum with a virtual spectrum synthesized from the past spectra to establish a harmonic path.

Another limitation of current HR estimation methods from UWB radar signal is the lack of tracking, i.e., HR is estimated using data from only the current frame. Tracking

enhances robustness of an estimation algorithm. SHAPA [7] is our early effort to move towards tracking, but it is a rather *ad-hoc* approach. To our knowledge, there is no other work reported that performs HR tracking from UWB radar signal. Methods of HR tracking, however, have been proposed for other pulse rate sensors such as ECG, ABP, and PPG.

For ECG and ABP, tracking of HR has been implemented using sequential Bayesian filtering methods [36, 37, 38]. In these methods, the measured time-domain signal waveform is modeled as a summation of multiple harmonically related components (sinusoids). This measurement model necessitates a state vector that contains the HR fundamental frequency and the amplitudes these harmonic components. These approaches have high computational complexity because the state vector is highly dimensional, and the state vector is estimated every signal sampling interval. Furthermore, adaptive selection of the model parameters is recommended to reduce modeling error, using grid search [37]. In this adaptive selection approach, the recursive estimates of the state vector over a time interval are repeatedly computed for each possible set of parameter values, and the set for which the reconstructed signal best fits the measured signal is selected. This adaptive selection process further multiplies the computation complexity of the time-domain multi-harmonic model.

Applying the above tracking methods to UWB radar signal causes several problems. First, to track the HR, a plethora of nuisance state variables also need to be tracked; this results in high dimensional state vector and therefore high complexity, as explained above. Furthermore, interference from RR harmonics also needs to be modeled, requiring adding another set of RR harmonically-related components, thus further increases the state dimension. Second, the presence of random body movements causes very large noise variance in the multi-harmonic measurement model. Unmodeled phenomena such as multiple layers of body, possible nonlinearities in the radar RF front end and external interference also increases the noise variance. Example of a range of our measurements are shown in Figures 5.2a and 5.2b.

Several HR tracking methods have been proposed for contact PPG sensors such as PPG

wristbands [39, 40, 41, 42]. In [39], a successive motion artifacts canceling filter is first applied on two PPG signal channels to remove macro body motion artifacts. Then, a HR peak tracking rule that relies on the presence of the highest peaks in the vicinities of the first three harmonics of the previous HR estimate, and several selection rules are proposed to compute the HR estimate from the frequency locations of these peaks. This tracking scheme is rather heuristic and might not be amenable to UWB radar signal, which can have missing HR harmonics (including the fundamental) and strong RR harmonic track. Motion artifacts removal and HR tracking rules were also proposed in [40, 41], however these algorithms involve solving a high-dimensional linear inverse problems for sparse spectrum estimation of PPG signal [40] and joint sparse spectrum estimation of PPG and accelerometer signals [41]. High complexity is another issue in these estimation algorithms. The algorithm used to solve these linear inverse problems, FOCUSS [43], increases the average processing time by 124 s for a signal frame of only 8 s [39]. The algorithm in [39], although is shown to significantly outperform [40, 41] in terms of processing time, takes 6 s for the same frame duration. Furthermore, all these processing time values were obtained for an Intel Core i7-4930 K CPU@3.40 GHz PC, thus the processing time of these algorithms will be significantly greater for resource-limited embedded systems, precluding practicality of real-time vital signs monitoring. In addition, in all these algorithms [39, 40, 41, 42], accelerometer data obtained simultaneously with PPG data is required to remove motion artifacts. In contrast, for the purpose of non-contact monitoring, accelerometry is not used in our experiments. Also, these tracking methods solely based on the HR estimate in the previous frame. In contrast, sequential Bayesian filtering approach, information from all the past frames are naturally carried over to the current frame.

Besides, the ECG, ABP, and PPG signals targeted in the tracking algorithm design of [36, 37, 38, 39, 40, 41, 42] do not share characteristics of UWB radar signal. The ECG signal presented as experimental results in [36, 38] is said to contain a high level of noise and is one of the noisiest signal in the MIMIC database on PhysioNet [44]. However, the

spectrogram presented in the works shows that the first six HR harmonics are the strongest peaks, the higher order HR harmonics have significant energy, and the noise level is much lower the signal (harmonics) levels. In contrast, the SNR in our UWB heart-related data is much lower: significant peaks are present at locations other than the HR harmonics locations (Fig. 5.2bc). This low SNR is due to the *non-contact* sensing of the weak heart-related displacement. This is one of the major challenges of developing an accurate and robust HR estimation algorithm for non-contact radar sensors. The PPG pulsatile signal is modulated directly by the heart pumping action, similar to ECG. On the other hand, the radar received signal is directly modulated by not only heart beating but also (a much stronger) breathing motion. In fact, RR harmonics interference that can mask or displace the HR fundamental has not been reported as a source of artifact in PPG signal. The ECG and PPG signals, obtained from sensors in contact with the skin, have higher SNR than the signal obtained from the non-contact IR-UWB radar signal.

In order to tackle the challenges of low signal-to-noise, interference issue, and unmodeled phenomena in our measurements, we propose to use data to build the state transition and likelihood models required for Bayesian tracking. Our state is scalar, and observation is defined as a spectral feature that leverages the HR harmonics and knowledge of RR harmonic.

In existing HR estimation algorithms with UWB radar, the number of subjects and data length per subject reported are small, limited to one subject [9, 6] to eight subjects [7]. In [29], the experimental results are reported for only four subjects, who were sitting-still under lab-controlled condition, and all the data sets are less than 100 seconds. Signal morphology changes from one individual to another, and from time to time for a single individual, thus a sufficiently long duration of data and a larger number of subjects are desired. In this dissertation, the algorithm performance is evaluated with 26 subjects of both genders with a range of demographics. During certain intervals of time some some of the subjects do certain activities that represent some natural behaviors of patients in bed

such as picking up a book, turning pages, talking over cell phone, moving hands or arms, and turning to the side or the stomach.

Existing UWB vital signs estimation methods [31, 9, 15, 11, 45] use sub-nanosecond sampling intervals, corresponding to sampling rate on the order of tens of GHz in order to recover the RR and HR frequencies which are on the order of only a few Hz (human RR ranges from 0.2 to 0.7 Hz, and HR ranges from 0.75 to 3 Hz). These methods organize recorded signal into a matrix where a row (called "fast-time") contains a received waveform corresponds to one transmitted pulse, and a column (termed "slow-time") corresponds to the time instances when the waveforms are received. Then, the column with highest energy is identified and the conventional periodogram method is used to estimate the rate from that column. These methods use tens of GHz sampling rate and down-sample to on the order of pulse repetition frequency (kHz-MHz). The memory requirement is also huge. In summary, except the work of the authors, to our knowledge, the existing methods use tens of GHz sampling rate and ignore HR harmonics.

Another limitation with most existing works is the lack of cross validation to avoid overfitting of algorithm parameters to the specific data sets used. This is worrisome if the number of subjects/amount of data is small. In this dissertation, we implement $k$-fold cross validation [46], which is a commonly used method in machine learning to predict the error performance on new (unseen) data, i.e., data that have not been used in the design of a model or algorithm.

In summary, this dissertation presents a novel HR estimation algorithm that leverages tracking, HR harmonics, RR harmonics, and motion artifact removal. Bayesian filtering with training is applied to learn the required density functions. Cross-validation is used to better evaluate the potential of applying our algorithm on unseen data. Since adding up harmonic powers [34, 35] is less restrictive than relying on the presence of consecutive peaks at around the HR harmonics locations [6, 7], we adopt the harmonic power aggregation approach in [34, 35], but also propose to incorporate the knowledge of possible presence

of the RR harmonic. We focus on HR estimation because RR estimation is easy.

## 2.4 Estimation of chest displacement morphology

Chest displacement morphology is currently obtained using the respiratory inductance band. With excellent temporal/spatial resolution, IR-UWB radar has been used to extract such morphology by the correlation method. Specifically, the pulse delays are estimated using by correlating the received pulses with a pule template, and the displacement is then computed from the pulse delays [47, 13]. The correlation approach has extremely high computational complexity as it requires sub-nanosecond sampling rate. In addition, no Cramér-Rao lower bounds for the chest displacement estimates have been derived.

## 2.5 Detection of body motion and posture change

Pressure ulcers or bed-sores are common but preventable problems in nursing homes especially for physically impaired elderly patients [48]. These ulcers can be caused in-part by immobility of the subjects [48]. Laying in one posture for a long period of time can impede blood flow and decrease the supply of oxygen and nutrients to the concerned muscles [48]. The development of pressure ulcers can interfere with the recovery process and also lead to premature mortality in some patients. The cost associated with the treatment of these ulcers is also high and causes significant burden on annual healthcare expenditure [48].

One solution to prevent these pressure ulcers is to monitor and make sure that patients have changed posture periodically [49]. Many researchers [50, 51, 52, 53] have studied detection of body postures with pressure sensor sheets. The pressure applied by the body as the patient lays on such a sensor sheet creates a pressure image, which changes with a change in posture. In these methods, a large number of sensors, hundreds or even thousands [52, 51], are needed to improve the classification resolution. Therefore, the amount of data that needs to be processed in the pressure image analysis is enormous, leading to high computational cost and excessive delay. Some studies have proposed methods for posture

detection using wearable accelerometer sensors [54, 55]. Electrocardiogram sensors have also been used for posture detection as morphology of the QRS-complex in ECG changes with the body posture [56, 57]. However, the drawback associated with these types of sensors is that they require some contact with the skin / body in the form of adhesive electrodes or other attaching mechanisms. These contact sensors may raise concerns about discomfort and hygienic conditions of the patient.

The UWB radar received signal contains information about the periodic movement of chest wall caused by breathing and heartbeat. Since chest displacement introduces time-varying round trip propagation delays in the received pulses, presence of motion related artifacts caused by subject movement degrades the signal-to-noise ratio (SNR) of the received signal and affects the accuracy of estimated HR and RR. Thus, the detection and quantification of these motion-corrupted parts is not only important for consistent and accurate estimation of vital signs parameters but this information can also be leveraged to detect posture changes.

Many researchers have focused on detection of motion and posture from an IR-UWB radar along with the vital signs sensing. Khan *et al* [58] implement a motion detector on an IR-UWB vital signs monitor based on an autocorrelation approach. Ota *et al* [59] compute the changes in the power-range profile of the IR-UWB received signal over time to detect various motion types of the subject, such as in-bed motion (sitting up) and motion that is outside of the bed but inside the room (wandering and going in and out of the door). Another approach to detect the type of motion similar to the latter is presented in [60]. In this approach, a threshold decision method based on energy detection is used to detect the human motion that involves moving from one range cell to another such as walking or running. All these methods use very high sampling rates (tens of GHz) for the radar signal and are also hampered by large storage requirements for the recorded data.

## 2.6 Challenges faced with the measured data

In this dissertation, there were a few challenges associated with the real-world experimental data that was used for algorithm development. Details for how we deal with these challenges are described in the following chapters. Here, we summarize these challenges.

- Low SINR: Heart pumping motion is much weaker than respiration motion. Filtering out the low frequency components belonging to the valid human RR cannot completely eliminate respiration interference, since some RR harmonics fall into the heart frequency band and interfere with the HR fundamental and harmonics. Body macro movements such as those caused by limbs is another source of interference that corrupts data. Cardiopulmonary information is imposed into the received signal by the minute displacement of the chest wall due to heart and lungs movement. The FCC regulation on the maximum transmitted power spectral density level and the non-contact sensing nature of the radar makes the power of the signal component very weak.

- Hardware limitation: We are not able to make changes to the hardware. Our ADC sampling rate is only 128 Hz, which prevents us from obtaining the radar received signal with sub-nanosecond resolution. This sampling rate, however, is sufficient for detecting the HR and RR.

- Limited sample of true HRs: The subjects HRs do not span the whole range of human valid HRs. This can cause bias of the estimation algorithms towards the HRs in our data, thereby hinders the statistical significance of our methods.

- Limited data to improve statistical significance of estimation methods

- Errors in ground-truth device (the pulse oximeter)

# CHAPTER 3

# IR-UWB RADAR SPECTRUM FOR A PERIODICALLY MOVING REFLECTOR - APPLIED TO VITAL SIGNS SENSING

The moving chest wall imparts a delay modulation onto the reflected IR-UWB radar signal, making the radar return a nonlinear function of chest wall displacement. Existing theoretical spectral models of the IR-UWB radar reflections from the human chest wall have restrictive assumptions that preclude realistic modeling of chest wall displacement and assume an aliased version of the radar signal. This chapter presents a novel theoretical analysis of the un-aliased spectrum, without the restrictive assumptions of previous works. Potential applications not specifically treated in this dissertation, but illustrative of the novelty and broader scope of the presented analysis, include heart-induced displacements that are realistically more bursty in nature and breathing-induced displacements consistent with, for example, non-unity inspiration-to-expiration ratios (IERs) characteristic of asthma; neither of these could be analyzed using previous models. As is well known, the un-aliased spectrum cannot generally be recovered from the aliased spectrum. In particular, it will be shown that the clusters of the non-aliased spectrum are not just scaled versions of each other; rather they have complex variations that if measureable, could enable estimation of parameters such as displacement amplitude; such variations are not apparent in the aliased spectrum, which has just one cluster. The degree to which the aliased model differs from the non-aliased model is analyzed. The chapter also addresses some practical aspects of the spectral model, such as the number of significant components in a spectral cluster and computational complexity of the theoretical model.

## 3.1 Introduction

We present the first generic spectral model of the IR-UWB signal as it arrives at the radar receive antenna, for an arbitrary periodically moving chest interface. The work presented was an effort to reverse-engineer the hardware (e.g. RF front-end and analog filter chain) of the commercial IR-UWB radar device used in the experiments of this dissertation from its ADC samples. To our knowledge, all existing analytical models were derived for aliased signals [8, 9, 10]. In contrast, a model that can apply to a type of direct down-conversion radar receiver that produces un-aliased samples [5] is needed. Since the spectrum of the original continuous signal cannot generally be constructed from the aliased spectrum, the models of [8, 9, 10] cannot simply be applied to our problem. In fact, it will be shown in this chapter that the aliased spectrum is significantly different from the un-aliased spectrum. Furthermore, more realistic models of typical chest movements than are available in these existing analytical models are of interest. For example, the inspiration or inhalation period of a normal breathing pattern is approximately half the expiration or exhalation period, and for asthma patients experiencing symptoms the disparity is much greater [61, 62]. Such a breathing pattern is not consistent with the breathing displacement models treated in [8, 9, 10], which consists of one or two sinusoidal components. Similarly, heart beating is a bursty activity [63, 64], not modeled well with just one sinusoid [9]. Therefore, there is a need for an unaliased IR-UWB spectral model that accommodates an arbitrary periodic chest displacement pattern, i.e., a pattern with an arbitrary number of sinusoidal components.

The presented analysis approach, which avoids the "fast time, slow time" formulation in [8, 9, 10], yields a model that is amenable to various applications. This model presents the Fourier coefficients in closed-form for a transmitted periodic impulse waveform and a single planar reflecting interface. The resulting expressions constitute a tool that other researchers can use to analyze any periodic transmit waveform, e.g., periodic pseudo-random

binary sequences [65], any periodic displacement pattern of the interface, and any planar multi-layered reflecting interface by applying well-known Fourier techniques. The model exposes the effects of aliasing and of different breathing and heart beating patterns. The chapter gives an example of these applications and also analyzes model complexity. And since the presented model captures the signal as it arrives at the receiver antenna, it can be put with any RF front end model to provide the radar received signal. In other words, the presented delay-modulated base model is a critical core component that enables a full system model.

In the context of vital signs sensing, the reflecting interface is the chest, assumed to be planar. The human thorax tissues have many layers [66, 67], composed of, e.g., skin, fat, muscle, cartilage, lung, heart, and blood. Theoretically, there is an echo return from each interface between two layers. However, in this analysis, we consider only reflection from one interface, the skin-air interface, because the majority of the reflected energy is from this interface, rather than from the interfaces inside the body. For example, at 3.1 GHz, reflected energy from lung and reflected energy from heart are 58 dB and 90 dB below that from skin, respectively; at 5 GHz, reflected energy from lung and reflected energy from heart are 87 dB and 130 dB below that from skin, respectively [67]. Nevertheless, extension to the case where the reflections come from multiple reflecting layers, such as lung walls and heart wall, is straightforward by the principle of superposition.

The chest is assumed to be planar and its displacement is assumed to depend on the periodic lung displacement and the periodic heart displacement. Since the presented model is a decomposition of the signal part of the radar received spectrum, receiver noise will be ignored in our analysis, but noise can always be added to the model presented herein. An example plot of the Fourier spectrum produced by our model is shown in Fig. 3.1. The RR fundamental component ($f_b$) and its next harmonics ($2f_b, 3f_b$), the HR fundamental ($f_h$), and some intermodulation products (*intermods*), e.g., $f_b + f_h$, are clearly observed. Unfortunately, a fully characterized IR-UWB radar system that would enable a comparison

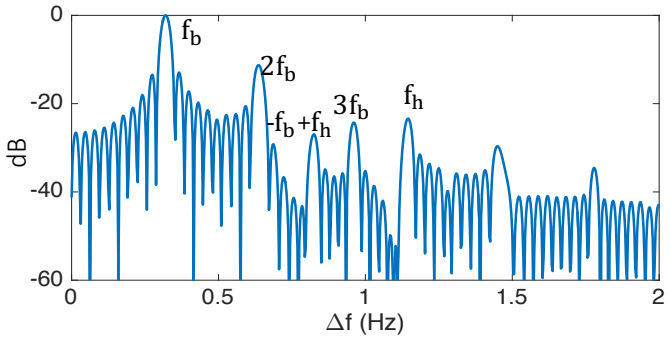


Figure 3.1: An example of a radar received spectrum obtained with the new model.

of the presented theoretical spectrum and a measured spectrum is not available. However, the spectrum produced by the presented model in Fig. 3.1 does compare favorably to the measured spectrum shown in Fig. 13b in [9]. For Fig. 3.1, we tried to match the parameters of the measured spectrum in [9]. In particular, we set the observation window to be rectangular with a length of 32 s, the HR is the ground truth HR reported in [9], and the RR is selected to be the frequency of the highest peak in the measured spectrum since its ground-truth is not provided in [9]. We also selected the displacement amplitudes to give similar relative heights of the peaks at the breathing and heart fundamentals. These values are listed in Table 3.3.

The UWB pulse used is a Gaussian monocycle [68] of order 7 with the bandwidth scaling factor of $0.3$ ns, whose waveform is similar to the pulse waveform in [9]. The pulse shape and its Fourier transform are plotted in Fig. 3.2. Other parameters for this example are discussed in Section 3.3.2.

The proposed framework should have several other uses. Signal models are essential in the development of signal processing techniques. Spectral analysis is a common approach for radar-based vital signs estimation, but typical schemes focus only on the location of spectral peaks as a means of estimating rates [9, 8, 11, 6, 7] and ignore peak heights. In contrast, the model reported herein will allow investigation into how breathing and heart *patterns* of movement impact the *shape* of the IR-UWB spectrum. For example, our findings show that the heights of the spectral peaks in the received spectrum depend on the

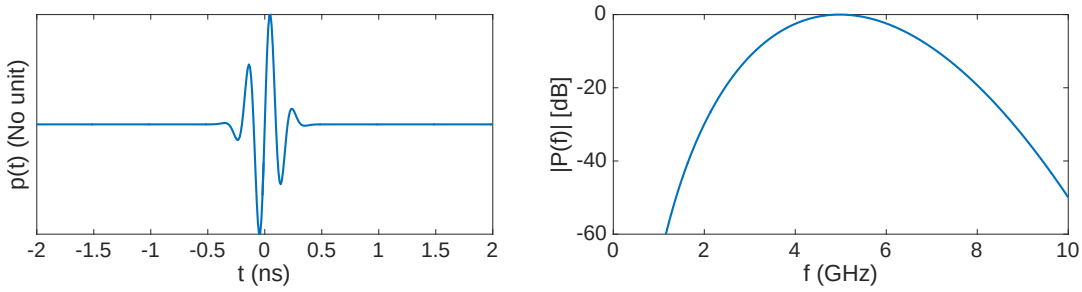


(a) (b)

Figure 3.2: Gaussian monocycle of order 7 and bandwidth scaling factor of $0.3$ ns. (a) Time-domain waveform $p(t)$. (b) Spectrum or Fourier Transform, $P(f)$, of $p(t)$.

maximum chest displacement; we note this is not a trivial dependence in delay modulation, which is a non-linear modulation. In addition, our model is not restricted to only the moving planar chest wall, but is also applied to any electro-magnetic wave reflected by a planar interface that displaces periodically. For example, a potential application could be detection of certain motors or machines by their vibration pattern.

The remaining of this chapter is organized as follows. Section 3.2 presents our general result. The special case of the sum-of-two-sinusoids chest displacement model considered in [9] is addressed in Section 3.3. Practicality on the usage of our analytical spectrum model is discussed in Section 3.4, where a numerical check on the accuracy of our mathematical derivation is also conducted. Computational complexity comparison with direct application of the continuous-time Fourier transform is discussed in Section 3.5. Section 3.6 concludes the work.

## 3.2 Derivation of the general case

This section starts with a base model, derived for the case of transmitted perfect impulses and a rectangular observation window of infinite length. We then show how the base model is readily modified for any UWB pulse or burst shape, any observation window of finite length, and when the received signal comprises back-scattered components from multiple layers of the thorax. Finally, an example of model usage is given.

The received signal is assumed to contain only the reflection from the air-skin interface, modeled as an infinite plane [1]. The periodic chest displacement is modeled as a summation of a periodic breathing-induced displacement and a periodic heartbeat-induced displacement, each of which is represented by a Fourier series expansion. Therefore, the round-trip propagation delay caused by chest displacement of an UWB pulse or burst can be modeled as

$$\tau_d(t) = A_0 + \sum_{p=1}^{N_b} \left[ B_p^b \sin 2\pi(pf_b)t + A_p^b \cos 2\pi(pf_b)t \right] + \sum_{q=1}^{N_h} \left[ B_q^h \sin 2\pi(qf_h)t + A_q^h \cos 2\pi(qf_h)t \right], \quad (3.1)$$

where $f_b$ is the respiration rate [Hz], $f_h$ is the heart rate [Hz], $N_b$ and $N_h$ are the numbers of non-DC Fourier series coefficients of the breathing-induced delay and the heartbeat-induced delay, respectively. $A_0$ combines the DC components of the breathing-induced and heartbeat-induced delays and the delay due to the nominal distance between the radar and the subject's chest. Note that there is no assumption on the phase of the breathing-induced delay and the phase of the heartbeat-induced delay; they are incorporated in the Fourier series coefficients $\{B_p^b, A_p^b, B_q^h, A_q^h : p = 1, \ldots, N_b; q = 1, \ldots, N_h\}$.

The IR-UWB radar system transmits pulses or short bursts with the repetition period of $T_r$. Assuming the chest location is constant for the duration of the pulse or burst, the round-trip delay of the $n$-th pulse or burst can be represented as the $n$-th sample of $\tau_d(t)$ with the time sampling interval equal to $T_r$: $\tau_{d,n} = \tau_d(nT_r)$, where $\tau_d(t)$ is given in (3.1).

[1] As in [8, 9, 10], we assume that the environment is static so the only motion that modulates the radar signal is from the movement induced by breathing and heart beating. Each recorded waveform is a superposition of a pulse reflected from the moving chest and pulses reflected from the static clutter. A "motion filter" [8, 9] suppresses the static clutter-reflected pulses but retains the moving-chest-reflected pulses.

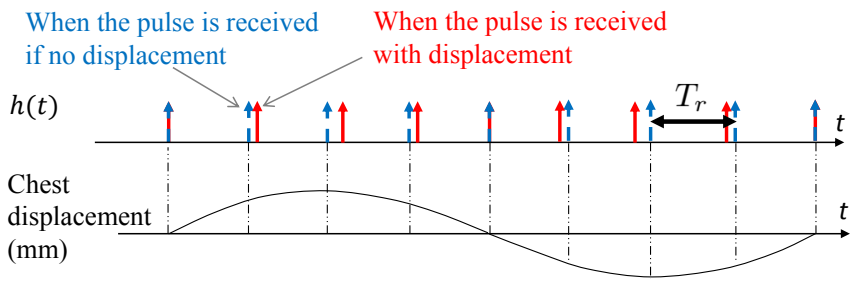


Figure 3.3: The channel response of the physiological sensing IR-UWB radar system to a series of impulses for sinusoidal chest displacement.

### 3.2.1 Base model - Perfect impulses are transmitted

Assuming that motion filtering rejects static clutter [8, 9], a planar chest model, and that the received signal contains only reflection from the skin-air interface, the sole channel effect is one time-varying delay, so the impulse response is simply a delayed Dirac delta function such that the delay is a periodic function of time. Constant amplitude reductions, e.g. due to path loss, are ignored, since they would have the effect of simply scaling the received signal spectrum.

The channel response to a periodic train of impulses with period $T_r$, is

$$h(t) = \sum_{n=-\infty}^{\infty} \delta(t - nT_r - \tau_{d,n})$$

and is illustrated in Fig. 3.3 for the chest displacement modeled as a sine waveform.

The continuous time Fourier transform (CTFT) of $h(t)$ is $H(f) = \sum_{n=-\infty}^{\infty} e^{-j2\pi f(nT_r+\tau_{d,n})}$ and is derived using Fourier theory and Jacobi-Anger expansions to be

$$H(f) = \sum_{i} \sum_{k_1} \cdots \sum_{k_{N_b}} \sum_{k'_1} \cdots \sum_{k'_{N_b}} \sum_{l_1} \cdots \sum_{l_{N_h}} \sum_{l'_1} \cdots \sum_{l'_{N_h}} c(f_{\mathbf{z}})\, \delta\Big(f - f_{\mathbf{z}}\Big), \qquad (3.2)$$

where $\mathbf{z} = [k_1, \ldots, k_{N_b}, k'_1, \ldots, k'_{N_b}, l_1, \ldots, l_{N_h}, l'_1, \ldots, l'_{N_h}, i]$,

$$f_{\mathbf{z}} = \Big[\sum_{p=1}^{N_b} p(k_p + k'_p)\Big] f_b + \Big[\sum_{q=1}^{N_h} q(l_q + l'_q)\Big] f_h + i f_r, \text{ and}$$

$$c(f) = f_r (-1)^{\sum_{p=1}^{N_b} k_p + \sum_{q=1}^{N_h} l_q} (-j)^{\sum_{p'=1}^{N_b} k'_{p'} + \sum_{q'=1}^{N_h} l'_{q'}} e^{-j2\pi A_0 f}$$
$$\times \prod_{p=1}^{N_b} J_{k_p}(2\pi B_p^b f) \prod_{p'=1}^{N_b} J_{k'_{p'}}(2\pi A_{p'}^b f) \prod_{q=1}^{N_h} J_{l_q}(2\pi B_q^h f) \prod_{q'=1}^{N_h} J_{l'_{q'}}(2\pi A_{q'}^h f),$$

where $f_r = 1/T_r$ is the pulse repetition frequency.

*Proof*: To reduce complexity, assume the DC component in Eq. (3.1) is zero, i.e., $A_0 = 0$. When $A_0 \neq 0$, the resulting expression will be simply multiplied by $e^{-j2\pi A_0 f}$. We will use the following notations: $\Omega = 2\pi f, \Omega_b = 2\pi f_b, \Omega_h = 2\pi f_h$. We begin with $H(f) = \sum_{n=-\infty}^{\infty} e^{-j\Omega n T_r} e^{-j\Omega \tau_{d,n}}$. Into $e^{-j\Omega\tau_{d,n}}$, we substitute $\tau_{d,n} = \tau_d(nT_r)$ using (3.1), and apply the property $\exp\{\sum_k \alpha_k\} = \prod_k \exp\{\alpha_k\}$ to get a product with four factors of similar form; two of them are $\prod_{p=1}^{N_b} \exp\{-j\Omega B_p^b \sin p\Omega_b n T_r\}$ and $\prod_{q'=1}^{N_h} \exp\{-j\Omega A_{q'}^h \cos q'\Omega_h n T_r\}$. Based on the Jacobi–Anger expansion $e^{jz\sin\theta} = \sum_{n=-\infty}^{\infty} J_n(z) e^{jn\theta}$ and $e^{jz\cos\theta} = \sum_{n=-\infty}^{\infty} j^n J_n(z) e^{jn\theta}$, where $J_n(z)$ is the Bessel function of the first kind of order $n$, it is trivial to prove that $e^{-jz\sin\theta} = \sum_{n=-\infty}^{\infty} J_n(z) e^{-jn\theta}$ and $e^{-jz\cos\theta} = \sum_{n=-\infty}^{\infty} j^{-n} J_n(z) e^{-jn\theta}$. Applying these, we may express $e^{-j\Omega\tau_{d,n}}$ as

$$\prod_{p=1}^{N_b} \sum_{k_p=-\infty}^{\infty} J_{k_p}(\Omega B_p^b) e^{-jk_p p\Omega_b n T_r} \prod_{p'=1}^{N_b} \sum_{k'_{p'}=-\infty}^{\infty} J_{k'_{p'}}(\Omega A_{p'}^b) j^{-k'_{p'}} e^{-jk'_{p'} p'\Omega_b n T_r}$$
$$\times \prod_{q=1}^{N_h} \sum_{l_q=-\infty}^{\infty} J_{l_q}(\Omega B_q^h) e^{-jl_q q\Omega_h n T_r} \prod_{q'=1}^{N_h} \sum_{l'_{q'}=-\infty}^{\infty} J_{l'_{q'}}(\Omega A_{q'}^h) j^{-l'_{q'}} e^{-jl'_{q'} q'\Omega_h n T_r}.$$

After applying the distributive law across all summations (there are $2N_b + 2N_h + 1$ of them

in general) and defining the following notations

$$\sum_{\mathbb{K}} = \sum_{k_1}\sum_{k_2}\cdots\sum_{k_{N_b}}\sum_{k'_1}\sum_{k'_2}\cdots\sum_{k'_{N_b}}\sum_{l_1}\sum_{l_2}\cdots\sum_{l_{N_h}}\sum_{l'_1}\sum_{l'_2}\cdots\sum_{l'_{N_h}},$$

where $\mathbb{K} = [k_1, \ldots, k_{N_b}, k'_1, \ldots, k'_{N_b}, l_1, \ldots, l_{N_h}, l'_1, \ldots, l'_{N_h}]$,

$$\begin{aligned}\mathbb{J}(\alpha, \mathbb{K}, \Omega) = {} & J_{\alpha k_1}(\Omega B_1^b) J_{\alpha k_2}(\Omega B_2^b) \ldots J_{\alpha k_{N_b}}(\Omega B_{N_b}^b) \\ & \times J_{\alpha k'_1}(\Omega A_1^b) J_{\alpha k'_2}(\Omega A_2^b) \ldots J_{\alpha k'_{N_b}}(\Omega A_{N_b}^b) \\ & \times J_{\alpha l_1}(\Omega B_1^h) J_{\alpha l_2}(\Omega B_2^h) \ldots J_{\alpha l_{N_h}}(\Omega B_{N_h}^h) \\ & \times J_{\alpha l'_1}(\Omega A_1^h) J_{\alpha l'_2}(\Omega A_2^h) \ldots J_{\alpha l'_{N_h}}(\Omega A_{N_h}^h) \\ & \times j^{-\alpha(k'_1 + k'_2 + \ldots + k'_{N_b} + l'_1 + l'_2 + \ldots + l'_{N_h})}, \end{aligned} \tag{3.3}$$

$$\begin{aligned}\bullet &= \big((k_1 + k'_1) + 2(k_2 + k'_2) + \ldots + N_b(k_{N_b} + k'_{N_b})\big) f_b \\ &\quad + \big((l_1 + l'_1) + 2(l_2 + l'_2) + \ldots + N_h(l_{N_h} + l'_{N_h})\big) f_h \\ &= \left[\sum_{p=1}^{N_b} p(k_p + k'_p)\right] f_b + \left[\sum_{q=1}^{N_h} q(l_q + l'_q)\right] f_h,\end{aligned}$$

where $\alpha \in \{-1, 1\}$, it is tedious but straightforward to show that

$$H(f) = \sum_{\mathbb{K}} \mathbb{J}(1, \mathbb{K}, 2\pi f) \sum_n e^{-j2\pi(f+\bullet)nT_r}. \tag{3.4}$$

Applying $\sum_{n=-\infty}^{\infty} e^{-j2\pi fnT} = \frac{1}{T}\sum_{m=-\infty}^{\infty} \delta\left(f - \frac{m}{T}\right)$ to the last summation in (3.4), and

using $f_r = 1/T_r$, we obtain:

$$\begin{aligned} H(f) &= \sum_{\mathbb{K}} \mathbb{J}(1, \mathbb{K}, 2\pi f) f_r \sum_{i=-\infty}^{\infty} \delta\left(f + \bullet - i f_r\right) \\ &= f_r \sum_{\mathbb{K}} \sum_{i} \mathbb{J}(1, \mathbb{K}, 2\pi f)\, \delta\left(f + \bullet - i f_r\right) \\ &= f_r \sum_{\mathbb{K}} \sum_{i} \mathbb{J}(-1, \mathbb{K}, 2\pi f)\, \delta\left(f - \bullet - i f_r\right). \end{aligned} \tag{3.5}$$

Since $J_{-n}(x) = (-1)^n J_n(x)$ for $n \in Z$, (3.5) becomes

$$H(f) = \sum_{\mathbb{K}} \sum_{i} f_r (-1)^{k_1 + k_2 + \ldots + k_{N_b} + l_1 + l_2 + \ldots + l_{N_h}} \mathbb{J}(1, \mathbb{K}, 2\pi f)\, \delta\left(f - \bullet - i f_r\right).$$

By moving the summation $\sum_i$ to the front, replacing $\mathbb{J}(1, \mathbb{K}, 2\pi f)$ with its definition in (3.3), and including $e^{-j2\pi A_0 f}$, we obtain Eq. (3.2).

The above model maps a decomposition of the displacement model into a decomposition of the received spectrum. Several observations can be made about the spectral decomposition.

1. The spectral component locations, represented by $f_{\mathbf{z}}$, are multiples of RR, multiples of HR, multiples of the pulse repetition frequency, and their intermods $kf_b + lf_h + if_r$, where $k, l, i$ are integers. In existing models, the frequencies do not contain multiples of the pulse repetition frequency.

2. The coefficients are expressed in closed-form. Existing models express the spectral coefficients as an integral over the entire bandwidth of the product of the pulse spectrum and one [8], two [9], or three [10] Bessel functions, or even more for a higher number of sinusoids in the pulse delay model, which does not have closed form.

3. The coefficients are a function of $f_b, f_h, f_r$, and the Fourier series coefficients in the delay model (3.1). This allows investigation into how breathing and heart patterns of movement impact the shape of the IR-UWB received spectrum. In existing models,

the coefficients do not depend on $f_b, f_h, f_r$.

This spectrum model, derived for a single-tap channel model with unity coefficient, can be easily extended to the case of a multi-tap channel model with arbitrary time-varying coefficients by using the principle of superposition. Such an extended model could be applied to a multi-layer model of the human thorax. Further details on the extension will be presented in Section 3.2.3.

### 3.2.2 Extension to practical transmission and receiving operations

The base model assumes transmission of Dirac impulses and an observation window of infinite length. In practice, UWB pulses or bursts are transmitted and only a finite duration of the signal is observed. The base model can be easily extended to these practical cases.

*UWB pulses or burst waveforms are transmitted*

Let $p(t)$ be the transmit UWB burst waveform and $P(f)$ be its CTFT[2]. The radar received signal is $y(t) = p(t) * h(t)$ and its CTFT is $Y(f) = P(f)H(f)$. It follows that $Y(f)$ is equal to the right hand side of (3.2) after replacing $c(f_{\mathbf{z}})$ with $g(f_{\mathbf{z}}) = c(f_{\mathbf{z}})P(f_{\mathbf{z}})$. The observations in Section 3.2.1 also apply here.

*Finite observation window*

The model in (3.2) assumes an infinite record of the received signal. Let $w(t)$ be the observation window of finite duration and $W(f)$ be its Fourier transform. In the case of a finite observation window, the channel response to a periodic train of impulses is $h_w(t) = h(t)w(t)$. Its CTFT is $H_w(f) = H(f) * W(f)$ and is equal to the right hand side of (3.2) after replacing "$\delta$" with "$W$".

Similarly, the channel response to a periodic train of UWB bursts, observed over a finite time window is expressed as $y_w(t) = y(t)w(t)$, and its CTFT is $Y_w(f) = Y(f) * W(f)$,

[2]for instance, $p(t)$ can be a pseudo-random binary-modulated waveform or just a simple pulse, as in [8, 9, 10]

Table 3.1: Extension to practical transmission and receiving operations

| | Spectrum | Change in right hand side of (3.2) |
|---|---|---|
| Impulses, infinite window | $H(f)$ | |
| Impulses, finite window | $H_w(f)$ | replace "$\delta$" with "$W$" |
| UWB burst, infinite window | $Y(f)$ | replace $c(f_{\mathbf{z}})$ with $c(f_{\mathbf{z}})P(f_{\mathbf{z}})$ |
| UWB burst, finite window | $Y_w(f)$ | replace "$\delta$" with "$W$" and $c(f_{\mathbf{z}})$ with $c(f_{\mathbf{z}})P(f_{\mathbf{z}})$ |

where $Y_w(f)$ is equal to the right hand side of (3.2) after replacing "$\delta$" with "$W$" and "$c(f_{\mathbf{z}})$" with "$g(f_{\mathbf{z}})$" $= c(f_{\mathbf{z}})P(f_{\mathbf{z}})$.

Table 3.1 summarizes how the base model (3.2) can be readily extended to these practical operations by making simple changes to its right hand side.

### 3.2.3 Extension to a multi-layer chest model

Let $S$ be the number of body tissues layers that move periodically due to breathing and/or heart beating. For the infinite observation window case, the channel response to a periodic train of impulses is $h(t) = \sum_{n=-\infty}^{\infty} \sum_{s=1}^{S} \mu^{(s)}(t)\ \delta(t - nT_r - \tau_{d,n}^{(s)}) = \sum_{s=1}^{S} \mu^{(s)}(t) \sum_{n=-\infty}^{\infty} \delta(t - nT_r - \tau_{d,n}^{(s)})$, where $\mu^{(s)}(t)$ and $\tau_{d,n}^{(s)}$ are the amplitude and delay of the tap modeling the $s^{\text{th}}$ layer.

By Fourier Transform and the principle of superposition, the CTFT of $h(t)$ is $H(f) = \sum_{s=1}^{S} \mathscr{F}\{\mu^{(s)}(t)\} * H^{(s)}(f)$ where $H^{(s)}(f)$ is (3.2).

The extension for the variations of $H(f)$, $\tilde{H}(f), Y(f)$ and $\tilde{Y}(f)$, can be done in a similar straightforward manner.

### 3.2.4 Example of model usage

Our model describes how each component in the Fourier decomposition of the displacement model contributes to the received the spectrum. Each sinusoidal term in the delay model in Eq. (3.1) corresponds to a summation in the radar received spectrum model in Eq. (3.2) (and its variations $\tilde{H}(f), Y(f)$ and $\tilde{Y}(f)$), as shown in Table 3.2. In other words,

Table 3.2: Mapping between a term in (3.1) and a summation in (3.2)

| (3.1) | $\sin 2\pi(pf_b)t$ | $\cos 2\pi(pf_b)t$ | $\sin 2\pi(qf_h)t$ | $\cos 2\pi(qf_h)t$ |
|---|---|---|---|---|
| (3.2) | $\sum_{k_p}$ | $\sum_{k'_p}$ | $\sum_{l_q}$ | $\sum_{l'_q}$ |

if the displacement model lacks a particular sinusoidal component, the corresponding summation will not be needed in the spectrum. For example, assume that $\tau_d(t) = B^b \sin 2\pi f_b t + A_1^h \cos 2\pi f_h t + A_2^h \cos 4\pi f_h t$. In this example, the delay due to breathing-induced displacement is modeled as a sine, and the delay due to heartbeat-induced displacement is modeled as a sum of two cosines whose frequencies are the HR and its next harmonic. The spectrum model in (3.2) becomes $H(f) = \sum_i \sum_{k_1} \sum_{l'_1} \sum_{l'_2} c(f_{\mathbf{z}})\, \delta(f - f_{\mathbf{z}})$, where $f_{\mathbf{z}} = k_1 f_b + (l'_1 + 2l'_2) f_h + i f_r$ and $c(f) = f_r (-1)^{k_1} (-j)^{l'_1 + l'_2} J_{k_1}(2\pi B_1^b f) J_{l'_1}(2\pi A_1^h f) J_{l'_2}(2\pi A_2^h f)$.

This example and discussion illustrate how this model, unlike the models of [8, 9, 10], do not have to be rederived as the chest displacement model changes.

### 3.3 Special case of sinusoidal breathing and heart beating

In this section, application of the general model in Section 3.2 to the special case of sinusoidal breathing and sinusoidal heart beating is presented, and features that differentiate our model from existing aliased models are clarified.

Specifically, we will use the displacement model assumed in [9], which is a sum of two sines with zero phase representing the breathing-induced and heartbeat-induced displacements, respectively. Mathematically, the delay due to this chest displacement model is written as

$$\tau_d(t) = A_0 + A_b \sin 2\pi f_b t + A_h \sin 2\pi f_h t, \tag{3.6}$$

where $A_0$ is the delay due to the nominal distance between the radar and the chest[9].

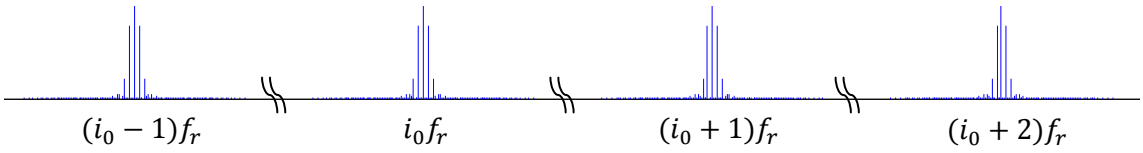


Figure 3.4: An example of $|H(f)|$. In this example, $i_0 = 20,000$ and $f_r = 250$ kHz, thus the clusters are in the vicinity of 5 GHz. The space between the cluster has been shrunk to aid visibility of the spectrum components within each cluster.

Table 3.3: Example simulation parameter values

| | | |
|---|---|---|
| Pulse repetition period | $f_r$ | 250 kHz |
| Window length | $T_w$ | 32 s |
| Maximum breathing displacement | $m_b$ | 5 mm |
| Respiration rate | $f_b$ | 0.3199 Hz |
| Maximum heart displacement | $m_h$ | 0.3571 mm ($m_b$/14) |
| Heart rate | $f_h$ | 1.14 Hz |

### 3.3.1 Infinite observation window

From (3.2), the CTFT of the channel response to the periodic train of impulses with period $T_r$ can be expressed as

$$H(f) = \sum_{i=-\infty}^{\infty} \sum_{k=-\infty}^{\infty} \sum_{l=-\infty}^{\infty} c(f_{\mathbf{z}}) \cdot \delta(f - f_{\mathbf{z}}), \tag{3.7}$$

where $f_{\mathbf{z}} = kf_b + lf_h + if_r$ and $c(f) = f_r(-1)^{k+l} J_k(2\pi A_b f)\, J_l(2\pi A_h f) e^{-j2\pi A_0 f}$.

The radar received signal spectrum with a received burst shape $p(t)$, $Y(f)$, is equal to the right hand side of (3.7) after replacing $c(f_{\mathbf{z}})$ with $g(f_{\mathbf{z}}) = c(f_{\mathbf{z}})P(f_{\mathbf{z}})$.

As an example, suppose $f_r$, $f_b$, $f_h$, the breathing-induced chest displacement amplitude $m_b$, and the heartbeat-induced chest displacement amplitude $m_h$ take the values in Table 3.3. $A_b = 2m_b/\nu$, $A_h = 2m_h/\nu$, where $\nu = 3 \times 10^8$ m/s, $A_0 = 2d/\nu$, where the nominal distance between the radar and subject is $d = 30$ cm. The expression in (3.7) is evaluated with this parameter set over the frequency range of several multiples of $f_r$ in the GHz range. The magnitude of the resulting spectrum, $|H(f)|$, is plotted in Fig. 3.4.

A clustered structure with great sparsity is observed; the spectrum contains clusters centered at multiples of $f_r$, each of which contains spectral components that are away from the cluster center by $kf_b+lf_h$, where $k, l \in Z$. The magnitudes of the spectrum components in the cluster centered at $i_0 f_r = 5$ GHz, normalized to the magnitude of the cluster center component, are plotted in Fig. 3.5a. The normalized components that are less than $-50$ dB are plotted in black. The rapid decay of the spectrum components as their order ($|k|$ and $|l|$) increases is observed. If $-50$ dB relative power level is considered as the lowest significant power, there are only 17 significant spectral components in this example, spanning just a few Hz, whereas the separation between the clusters is 250 kHz ($f_r$).

Although not obvious in Fig. 3.4, there is change in the magnitudes of the spectrum components from one cluster to the next. Fig. 3.5b plots the magnitudes of the cluster center, $f_b$, and $f_h$ components (which are $|c(f_{00i})|, |c(f_{10i})|,$ and $|c(f_{01i})|$, respectively) across the clusters in the frequency range of 3-7 GHz. In addition to the parameter set above, the plots include $m_b$ set to two other values of $3.62$ mm and $7.96$ mm, $m_h = m_b/14$, while the other parameters stay the same. Fig. 3.5b shows that the clusters are not simply scaled versions of each other. In particular, for example, for $m_b = 7.96$mm, which corresponds to the last three entries in the legend (i.e., the thickest, green curves), the cluster center component ($|c(f_{00i})|$, solid line) drops monotonically almost $30$ dB over the band, while the $|c(f_{10i})|$ component (dotted) first rises a few dB and then drops slightly. The changing pattern of the 3-tuple group differs for different values of $m_b$; this suggests that $m_b$ might be estimated from measurements of widely spaced clusters.

### 3.3.2 Finite observation window

Following Section 3.2.2, we have

$$H_w(f) = \sum_{i=-\infty}^{\infty} \sum_{k=-\infty}^{\infty} \sum_{l=-\infty}^{\infty} c(f_{\mathbf{z}}) \cdot W(f - f_{\mathbf{z}}). \tag{3.8}$$

for transmitted impulses, and

$$Y_w(f) = \sum_{i=-\infty}^{\infty} \sum_{k=-\infty}^{\infty} \sum_{l=-\infty}^{\infty} P(f_{\mathbf{z}}) c(f_{\mathbf{z}}) \cdot W(f - f_{\mathbf{z}}). \tag{3.9}$$

for transmitted UWB bursts with spectrum $P(f)$.

We calculate a very close approximation of $|Y_w(f)|$ for a rectangular window with $T_w = 32$ s and the same parameters as in the example in Section 3.3.1. This approximation is created from the 1600 most significant non-DC terms of (3.9), for the cluster centered at $i_0 f_r$, that is $i = i_0$ and $1 \leq |k|, |l| \leq 20$; these include the 17 most significant terms excluding the center component (DC after down conversion) in Fig. 3.5a. The calculated spectrum is shown in Fig. 3.1, where $\Delta f$ denotes the frequency relative to $i_0 f_r$, the cluster center location. The RR fundamental component and its harmonics, the HR fundamental, and some intermods are clearly observed. More details on truncation are given in Section 3.4.

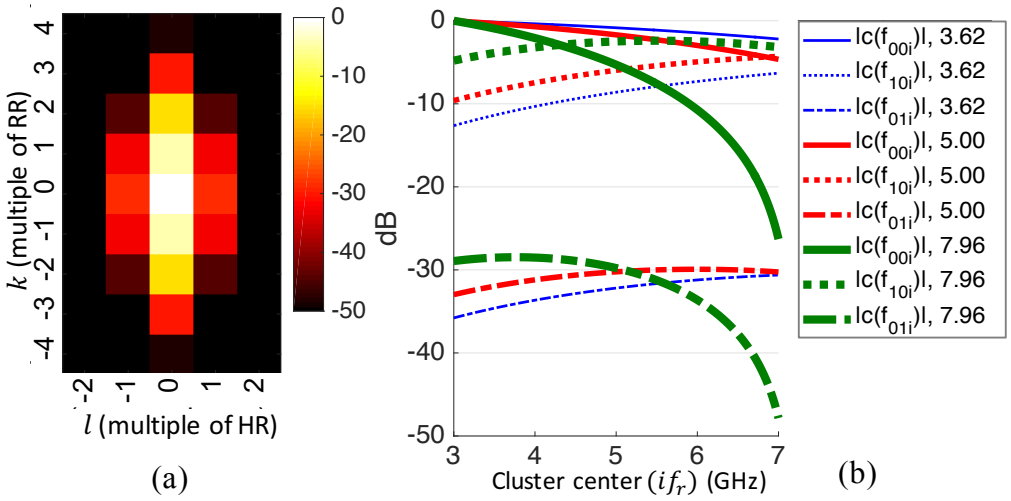


(a) (b)

Figure 3.5: (a) The spectrum coefficients $c(kf_b + lf_h + i_0 f_r)$, normalized to the cluster center and converted to dB, in the cluster centered at $i_0 f_r$ in Fig. 3.4. These coefficients correspond to the frequencies $kf_b + lf_h + i_0 f_r$. The normalized components that are less than $-50$dB are plotted in black. (b) Magnitude variation of the cluster center, $f_b$, and $f_h$ components (which are $|c(f_{00i})|, |c(f_{10i})|$, and $|c(f_{01i})|$, respectively) for different values of the maximum breathing-induced displacement $m_b$ (the maximum heartbeat-induced displacement $m_h = m_b/14$). The values of $m_b$ in mm are shown at the end of the legend items.

### 3.3.3 Features that differentiate our work from that of [8, 9, 10]

The authors of [8, 9, 10] describe their waveforms in terms of "slow time" and "fast time". The slow time axis indicates each pulse repetition, while the fast time index resolves waveform features within a pulse repetition period, as shown in Fig. 3.6a.

As in [8, 9, 10], we assume that the environment is static, so the only motion that modulates the UWB signal is from breathing and heart beating, and that a multipath profile, which is a waveform containing the reflected pulses from static clutter and the moving chest, is recorded every $T_s$. We note that $T_s$ must not be confused with the sampling period associated with the sampling within each multipath profile, which is a fraction of the pulse width and can be in the order of picoseconds. Although not mentioned in these papers, $T_s$ must be an integer multiple of the repetition period, $T_r$.

A "motion filter" [8, 9] passes the moving-chest-reflected pulses and suppresses the static clutter-reflected pulses [8, 9, 10]. The recorded waveforms after clutter removal are illustrated in the (slow time, fast time) coordinate system as in Fig. 3.6a. The samples at a given value of $\tau_1$ in the waveforms form the signal whose spectrum is analyzed in [8, 9, 10]. This can be seen, for example, in Eq. (7) of [9]. By unifying the slow time and fast time into the actual one-dimensional time, as in the two plots of Fig. 3.6b, it can be seen that the signal analyzed in [8, 9, 10] is obtained by sampling the received signal every $T_s$ with some sampling offset $\tau_1$ on the order of the pulse width. In other words, the sampling instants are $\tau_1, T_s+\tau_1, 2T_s+\tau_1, \ldots$ ($\tau_1$ should be thought as "fixed" in this context). This is an act of undersampling since the sampling rate is at most equal to the repetition frequency $f_r$, which is typically on the order of kHz or MHz and is smaller than the Nyquist rate which is on the order of GHz, thus causing aliasing, explained further as follows.

To compare with the aliased model in [8, 9, 10], infinite observation window case is used, since it is assumed in these papers. The spectrum of a sampled signal is well known

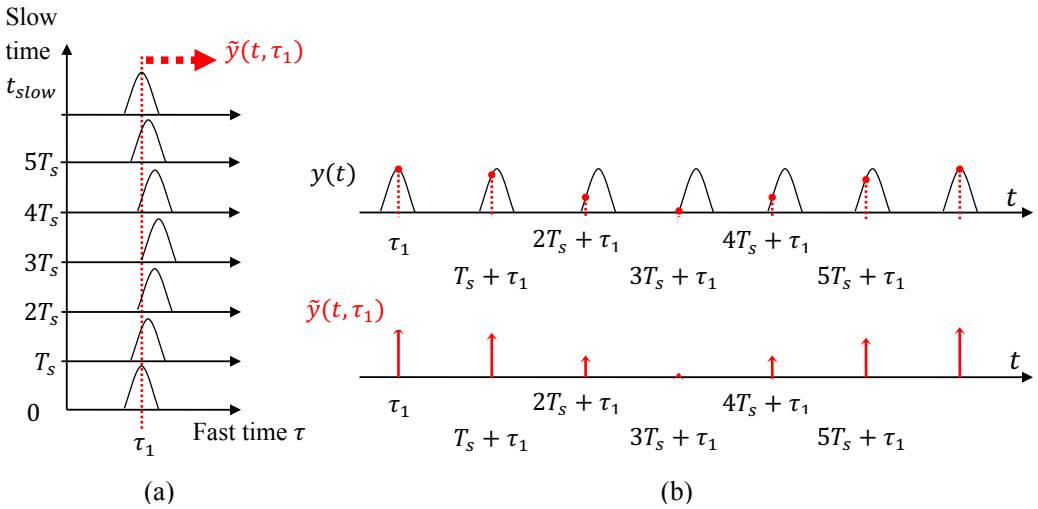


Figure 3.6: (a) Illustration of the signal analyzed in [8, 9, 10] in the (slow time, fast time) coordinate system: $\tilde{y}(t,\tau)$ for a given $\tau$ is the signal whose CTFT is computed in [8, 9, 10]. (b) Illustration of how it is related to the whole radar received signal on the 1D time axis.

to be

$$Y_a(f) = \frac{1}{T_s}\sum_{m=-\infty}^{\infty} Y\left(f - \frac{m}{T_s}\right), \tag{3.10}$$

which is periodic with period $\frac{1}{T_s}$. When $\frac{1}{T_s}$ is less than the Nyquist rate of $Y(f)$, the copies $Y(f - \frac{m}{T_s})$ for different $m$ overlap each other (this is aliasing), causing $Y_a(f) \neq Y(f)$ for at least some $f$ in every $\frac{1}{T_s}$ period [27]. Generally, we cannot use the spectrum expression in [8], [9], or [10] to construct the non-aliased spectrum of the whole radar received signal.

We can make the aliased spectrum using (3.10) and investigate numerically the differences between the aliased and un-aliased spectra. In order to avoid truncating the sum in a numerical evaluation, we assume $p(t)$ is a complex-exponentially-weighted sinc pulse such that its spectrum is a rectangle that spans 3GHz $- f_r/2$ to 7GHz $+ f_r/2$. Considering Fig. 3.4[3], the aliasing would not distort the spectrum of a single cluster if the clusters were identical. However, since the clusters are not identical, as explained in Section 3.3.1, there is some distortion in the aliased spectra of [8, 9, 10].

[3] $Y(f) = P(f)H(f)$ has similar magnitude plot as in Fig. 3.4

For simplicity, suppose $T_s = T_r$. Then the aliased spectrum is

$$Y_a(f) = \frac{1}{T_r} \sum_{m=m_{\min}}^{m_{\max}} Y(f - \frac{m}{T_r}),$$

where $m_{\min} = i_0 - \lceil 7 \times 10^9 / f_r \rceil$ and $m_{\max} = i_0 - \lfloor 3 \times 10^9 / f_r \rfloor$. The range $[m_{\min}, m_{\max}]$ ensures that all the clusters from 3GHz to 7GHz are included in the summation when it is evaluated in the neighborhood of $i_0 f_r$, i.e., all these unaliased clusters contribute to the aliased cluster centered at $i_0 f_r$. Next, we compute

$$\text{diffdB}(\Delta f) = 20 \log_{10} \frac{|Y(i_0 f_r + \Delta f)|}{|Y_a(i_0 f_r + \Delta f)|}$$

for selected values of $\Delta f$, and for 100 trials of breathing- and heartbeat-induced maximum displacements, including the $m_b$ and $m_h$ of the particular case of Fig. 3.4 and 99 random trials such that $m_b$ and $m_h$ are uniformly distributed, with $m_b \sim \mathcal{U}(2, 8)$ [mm] and $m_h \sim \mathcal{U}(2/128, 8/14)$ [mm]. $|Y(f)|$ and $Y_a(f)$ are normalized so their ratio is 1 at $f = i_0 f_r$, or $\text{diffdB}(0) = 0$ dB, which corresponds to the second cluster from the left in Fig. 3.4. If the aliased spectrum is identical to the unaliased spectrum, $\text{diffdB}(\Delta f) = 0$ for all values of $\Delta f$.

Fig. 3.7 displays diffdB for various values of $\Delta f$, comprising harmonics and intermods. For a particular harmonic or intermod, the graph shows diffdB values for two examples of the random $m_b$ and $m_h$, indicated by an open circle and an open triangle. Also included is the particular case of Fig. 3.4, indicated by a green "x". For example, at $\Delta f = f_b = 0.3199$ Hz, the two random trials yield spectrum magnitude differences of about 5 dB and 14.4 dB, and the Fig. 3.4 case gives a difference of about $-4.5$ dB. All the other random trial outcomes are plotted as blue dots, which for $\Delta f = f_b = 0.3199$ Hz, extend from about $-19$ dB to 20 dB. Finally, for each harmonic or intermod, the mean of the 100 diffdB values is plotted as a solid red square, and the first standard deviations away from the mean are indicated by red bars. We observe that for a given trial, e.g., indicated by triangles

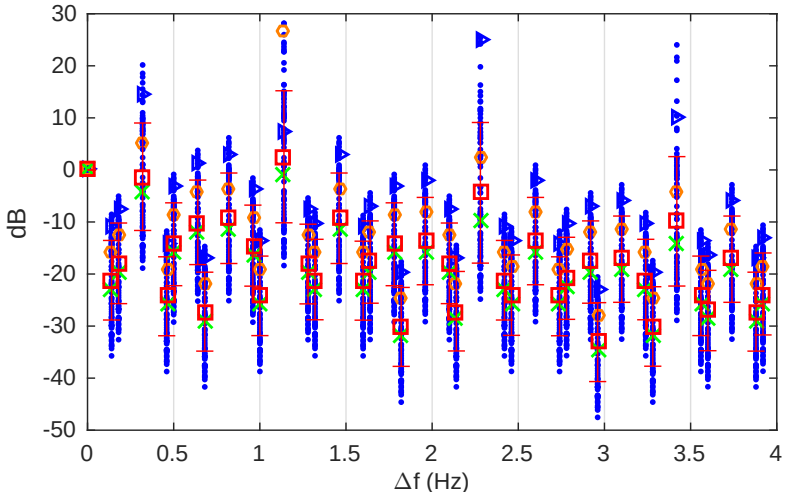


Figure 3.7: The relative power difference between the normalized un-aliased cluster centered at $i_0 f_r$ and the normalized aliased cluster over a frequency range for the example in Section 3.3.1 (shown by the green "x") and 99 random trials of $m_b$ and $m_h$. The relative power difference corresponding to two of these trials are shown with the triangle symbols and circle symbols respectively, and the other trials are represented by the small dots. The mean and standard deviation of the differences are also shown at each frequency location by a square and horizontal red bars.

for instance, the diffdB values vary across harmonics and intermods. We also observe diffdB values as large in magnitude as $47$ dB, indicating significant differences between the aliased spectrum of [8, 9, 10] and the un-aliased spectrum presented in this chapter. We have recomputed Fig. 3.7 for different kinds of representative UWB pulses (Gaussian monocycles of various orders and widths) [68] and similar differences are observed.

Fig. 3.7 displays diffdB for various values of $\Delta f$, comprising harmonics and intermods. For a particular harmonic or intermod, the graph shows diffdB values for two examples of the random $m_b$ and $m_h$, indicated by an open circle and an open triangle. Also included is the particular case of Fig. 3.4, indicated by a green "x". For example, at $\Delta f = f_b = 0.3199$ Hz, the two random trials yield spectrum magnitude differences of about 5 dB and 14.4 dB, and the Fig. 3.4 case gives a difference of about $-4.5$ dB. All the other random trial outcomes are plotted as blue dots, which for $\Delta f = f_b = 0.3199$ Hz, extend from about $-19$ dB to $20$ dB. Finally, for each harmonic or intermod, the mean of the 100 diffdB

values is plotted as a solid red square, and the first standard deviations away from the mean are indicated by red bars. We observe that for a given trial, e.g., indicated by triangles for instance, the diffdB values vary across harmonics and intermods. We also observe diffdB values as large in magnitude as $47$ dB, indicating significant differences between the aliased spectrum of [8, 9, 10] and the un-aliased spectrum presented in this chapter. We have recomputed Fig. 3.7 for different kinds of representative UWB pulses (Gaussian monocycles of various orders and widths) [68] and similar differences are observed.

These results in Fig. 3.7 show that neither [9, 8, 10] nor any works by others, to our knowledge, provide the closed-form formulas for the unaliased spectrum, even for displacement defined by only a few sinusoids. Furthermore, because [9, 8, 10] only give one aliased cluster, variations across clusters caused by breathing patterns of clinical relevance cannot be known from existing works. Finally, we note that for a given pulse shape, the amplitudes $g(f_{\mathbf{z}})$ in our model are functions of $f_b, f_h, f_r, A_b, A_h$ whereas the amplitudes in the model of [9]–Eq.(15) depend on only $A_b$ and $A_h$.

### 3.4 Practicality of the presented model

In this section, we discuss the practicality of our spectrum model and perform a numerical check on the accuracy of the mathematical derivation. Again, we start with the case of transmitted impulses. Extending the comparison to the case when UWB bursts are transmitted is straightforward and will be discussed at the end of this section.

Without loss of generality, assume the observation window is rectangular over $[-T_w/2, T_w/2]$. In this case, $h_w(t) = \sum_{n=-N}^{N} \delta(t - nT_r - \tau_{d,n})$, where $N = \lceil f_r T_w/2 \rceil$, and $\tau_{d,n} = \tau_d(nT_r)$, where we use the delay model $\tau_d(t)$ in (3.6). Therefore,

$$H_w(f) = \sum_{n=-N}^{N} e^{-j2\pi f(nT_r + \tau_{d,n})}. \tag{3.11}$$

The spectrum computed using (3.11) serves as ground truth, as it is based purely on the

definition of the CTFT of a time-domain signal. Ideally, the spectrum computed using our synthesis formula (3.8) should be the same as the spectrum computed by (3.11). However, this is not feasible for two reasons. First, (3.8) requires evaluating the summations over unbounded integer indices $(k, l, i)$. Another reason is the presence of numerical computation error of the computing software used. Calculations of both the truth and the synthesized spectra include floating-point errors and numeric precision limitations. All computation is implemented with double-precision floating-point arithmetic in MATLAB. The error also depends on the accuracy of the algorithm used by the computing software to compute the Bessel functions in (3.7). Fortunately, as we will show shortly, a synthesized spectrum that accurately matches the ground truth can be achieved with very small ranges of the integer indices, i.e., with a very small number of spectral components or terms.

As seen in Fig. 3.4, the clusters are separated by $f_r$, which is on the order of kHz or MHz, and as Fig. 3.5a exemplifies, the spectrum components in each cluster decay precipitously just a dozen Hz away from the cluster center. Such sparsity indicates that, in the case of a practical finite window length, one cluster has negligible overlap or interference from other clusters. Therefore, although (3.8) indicates (through the outermost summation) that the spectrum is a superposition of the clusters, the spectrum, when evaluated in the neighborhood of a cluster, can be computed using the contribution of that cluster only. Furthermore, the decay of the high order harmonics and intermods as shown in Fig. 3.5a encourages the use of finite limits of $k$ and $l$ in the two innermost summations of (3.8). The decay is rapid, thus (the absolute value of) those limits should be small. In summary, the ground-truth spectrum can be well approximated by a truncated version of (3.8):

$$\widehat{H_w}(f) = \sum_{k=-K}^{K} \sum_{l=-L}^{L} c(f^*) \cdot W(f - f^*), \tag{3.12}$$

for $f$ is in the vicinity of $i_0 f_r$, where $f^* = k f_b + l f_h + i_0 f_r$ and $K, L \ll \infty$.

As an example, suppose $T_w$, $f_r$, $f_b$, $f_h$, $m_b$, $m_h$ take the values in Table 3.3. Assume

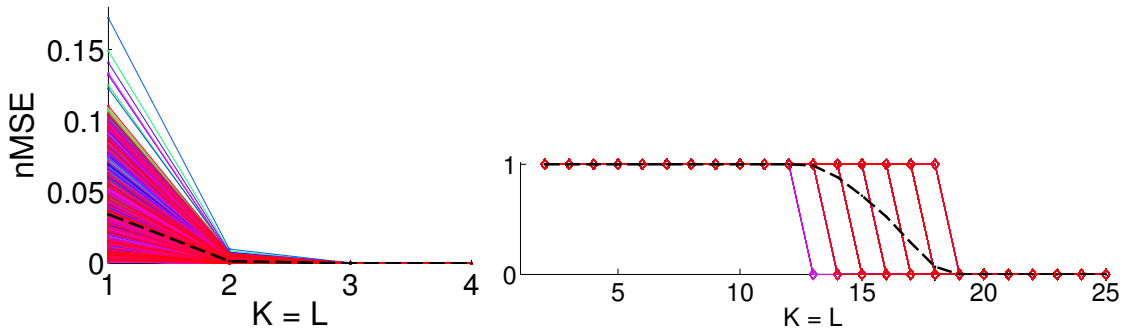


(a) (b)

Figure 3.8: Numerical error analysis. (a) Normalized MSE (mean squared error normalized to the variance of the true spectrum) over random trials for the $m_h = m_b/14$ case. The plot is an overlay of 1000 curves and their average, which is represented by the dashed line. (b) Indication of whether the spectrum synthesized with a value of $K$ is different from that synthesized with $K-1$ for the $m_h = m_b/14$ case. The plot is an overlay of 1000 curves and their mean, which is represented by the dashed line.

$A_0 = 0$ s. Although zero is not a practical value for $A_0$, it simplifies computation while not invalidating the comparison, because $A_0 > 0$ represents the same term $e^{-j2\pi A_0 f}$ in both expressions (3.8) and (3.11). The frequencies at which the ground truth spectrum and the synthesized spectrum are compared are chosen to be $af_b + bf_h + i_0 f_r$, where $a = -5:5, b = -5:5$ and $i_0 = 20,000$. In other words, we are interested in up to the $5^{\text{th}}$ order RR harmonic, the $5^{\text{th}}$ order HR harmonic, and their intermods in the cluster centered at 5 GHz; this is basically a narrow band of frequencies centered at 5 GHz. The true spectrum is computed using (3.11) with $N = \lceil f_r T_w/2 \rceil = 4 \times 10^6$, and its approximation is computed using the synthesis formula (3.12) with $K = L = 20$, i.e., with only $41 \times 41$ terms.

The error, $|H_w(f) - \widehat{H_w}(f)|$ does not exceed $1.04$, while the maximum value of $|H_w(f)|$ is about $1.2 \times 10^5$. The errors normalized to the standard deviation of the true spectrum are smaller than $0.71 \times 10^{-4}$ in magnitude. The mean squared error normalized to the variance of the true spectrum (nMSE) is $2.5 \times 10^{-9}$. Thus, our synthesized spectrum, using only a small number of terms, is extremely accurate.

We next present nMSE of the spectrum synthesis as a function of number of terms

kept in a truncated version (3.12). As in the example above, $T_w$ and $f_r$ are selected as in Table 3.3, and $A_0 = 0$. We generate 1000 random realizations of $[f_b, f_h, m_b]$, where $f_b \sim \mathcal{U}(0.2, 0.7)$ [Hz], $f_h \sim \mathcal{U}(0.8, 3.0)$ [Hz], and $m_b \sim \mathcal{U}(2, 8)$ [mm] , for each of four cases: $m_h = m_b/14$, $m_h = m_b/32$, $m_h = m_b/64$, $m_h = m_b/128$ (thus, a total of four independent 1000-trial sets). For each trial, the true spectrum and synthesized spectrum are computed at the frequencies $af_b + bf_h + i_0 f_r$, where $a = -5 : 5$, $b = -5 : 5$, and $i_0 = 20,000$, as in the example above. For simplification, we set $L = K$. The nMSE versus $K = L$ for the random trials of the $m_h = m_b/14$ case is plotted in Fig. 3.8a. The dashed line is obtained by averaging the nMSE curves. At $K = L = 1$ the worst case and average nMSEs are 17% and 4%, respectively. The nMSE quickly decreases as K and L increase and reduces to approximately $10^{-9}$ for $K = L \geq 3$. The nMSE graphs for the other three $m_b/m_h$ ratios are very similar qualitatively, hence are not shown.

Fig. 3.8b indicates whether the spectrum synthesized with some value of $K$ is, under the equality test of MATLAB ("isequal" function), different from that synthesized with $K - 1$, for each random trial of the $m_h = m_b/16$ case. A "1" indicates difference and a zero value indicates equality. The dashed curve is the mean of the indicator functions. The graphs for the other three $m_b/m_h$ ratios are very similar, and it is observed that the synthesized results stop changing for $K \geq 19$ in all of the 4000 random trials. Since increasing $K$ and $L$ does not change the synthesized spectrum and therefore the error, we think that the error is caused by numerical computation.

When the pulse shape in Fig. 3.2 is used, the synthesis formula is easily obtained by replacing $c(f^*)$ in (3.12) by $c(f^*)P(f^*)$. The formula is then evaluated at more finely spaced frequencies and the resulting spectrum is plotted in Fig. 3.1. Here the synthesis excludes the $(k = 0, l = 0, i = i_0)$ component in the synthesis formula, which would be the "DC" component after frequency down conversion [69]. The graphs of the true spectrum and synthesized spectrum cannot be visually distinguished, and hence the former is not shown.

We have demonstrated that an accurate spectrum can be achieved by synthesizing with only a relatively small number of terms. These numerical results also validate the correctness of our mathematical derivation in this chapter. The MATLAB code used in this chapter will be published on `http://www2.ece.gatech.edu/research/labs/sarl/`.

### 3.5 Computational complexity comparison

This section compares the computational complexity in terms of the number of multiplications of the CTFT formula and that of our model. Here we use $N_b'$ and $N_b''$ to distinguish the number of sines and the number of cosines in the breathing-induced delay model. Similarly, $N_h'$ and $N_h''$ are the number of sines and the number of cosines in the heart-beating-induced delay model. Thus, in Eq. (3.1), $N_b = \max(N_b', N_b'')$ and $N_h = \max(N_h', N_h'')$. Our synthesis model is obtained by setting finite limits for the integer variables in (3.2) (or its variations) as follows: let $[i_{min}, i_{max}]$ be the range of $i$, $[-K, K]$ be the range of the integer variables $k_m$'s and $k_m'$'s, and $[-L, L]$ be the range of the integer variables $l_m$'s and $l_m'$'s.

The number of multiplications in the CTFT formula is $(f_r T_w + 1)(5N_b' + 5N_b'' + 5N_h' + 5N_h'' + 4)$. The number of multiplications in our model of $H_w(f)$ is $(i_{\max} - i_{\min} + 1)(2N_b' + 2N_b'' + 2N_h' + 2N_h'' + 11)(2K+1)^{(N_b'+N_b'')}(2L+1)^{(N_h'+N_h'')}$.

The complexity of the CTFT formula linearly increases with $f_r, T_w, N_b, N_b', N_h, N_h'$. The complexity of our model exponentially increases with $N_b, N_b', N_h, N_h'$ but does not depend on $f_r$ and $T_w$. $[i_{\min}, i_{\max}]$ is the range of cluster indices $i$ that contribute to the spectrum at a frequency of interest. However, for practical value of $f_r$ (on the order of kHz or MHz) and $T_w$ (on the order of seconds), $i_{\min} = i_{\max} = i^*$ where $i^*$ is the cluster of the frequency range of interest.

*Example 1*: $f_r$ and $T_w$ are as in Table 3.3, $K = L = 20, i_{\max} = i_{\min}$. For the delay model used is Eq. (3.6), $N_b' = N_h' = 1, N_b'' = N_h'' = 0$. The number of multiplications in the CTFT formula and our model are $1.12 \times 10^8$ and $2.5 \times 10^4$, respectively. In this case, the complexity of our model is three order of magnitudes less than that of the CTFT

formula.

*Example 2*: However, when there are five sinusoids in the model, the complexity of our model is 10 times higher than the CTFT formula.

The ratio between the complexity of our model and that of the CTFT is plotted in Fig. 3.9 for various values of the pulse repetition frequency $f_r$. These $f_r$ values are manually collected from experimental settings of IR-UWB radar systems of many different groups [9, 70, 71, 72, 73, 74]. The horizontal bold dashed line indicates where our model has the same complexity with that of the CTFT. A value below this line indicates that our model has less complexity than the CTFT formula, and a value above this line indicates otherwise. Our model is able to achieve computational complexity reduction of several orders of magnitudes compared to the CTFT formula when the displacement model has a small number of sinusoids, but becomes more computationally expensive with more complex displacement functions. Additionally, the ratio curves when plotted in logarithmic scale almost linearly increase with the number of sinusoids in the displacement model. For a given number of sinusoids, the ratio decreases as $f_r$ increases, since the complexity of the CTFT formula increases with $f_r$ whereas our complexity does not depend on $f_r$. As a numerical check for this, computation time of the two formulas is measured with MATLAB 2015b on an Intel(R) Core(TM) i7-4870HQ CPU @ 2.50GHz laptop computer. Table 3.4 shows the computation time for the displacement model (3.6) for various values of $f_r$.

Table 3.4: Computation time of the CTFT formula and that of our model for a two-sinusoid displacement model

| $f_r$ | Our model | CTFT formula |
|---|---|---|
| 250 kHz | 0.0249 s | $141.3$ s |
| 500 kHz | 0.0233 s | $277.1$ s |
| 2 MHz | 0.0239 s | $1,102.8$ s |
| 10 MHz | 0.0238 s | $5,351.0$ s |
| 53 MHz | 0.0242 s | $27,510.0$ s |

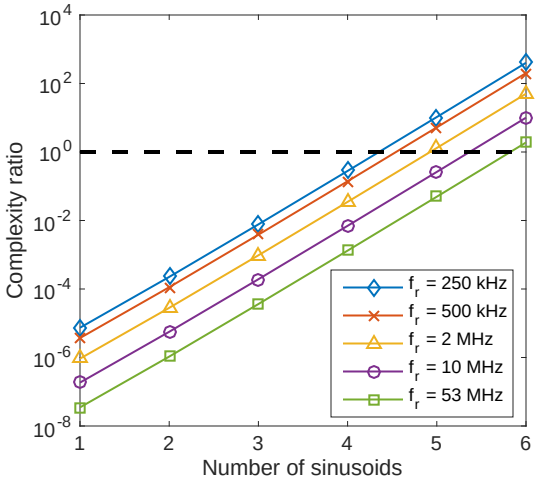


Figure 3.9: The ratio between the complexity of our model and that of the CTFT. The horizontal bold dashed line indicates where our model has the same complexity with that of the CTFT. A value below this line indicates that our model has less complexity than the CTFT formula, and a value above this line indicates otherwise.

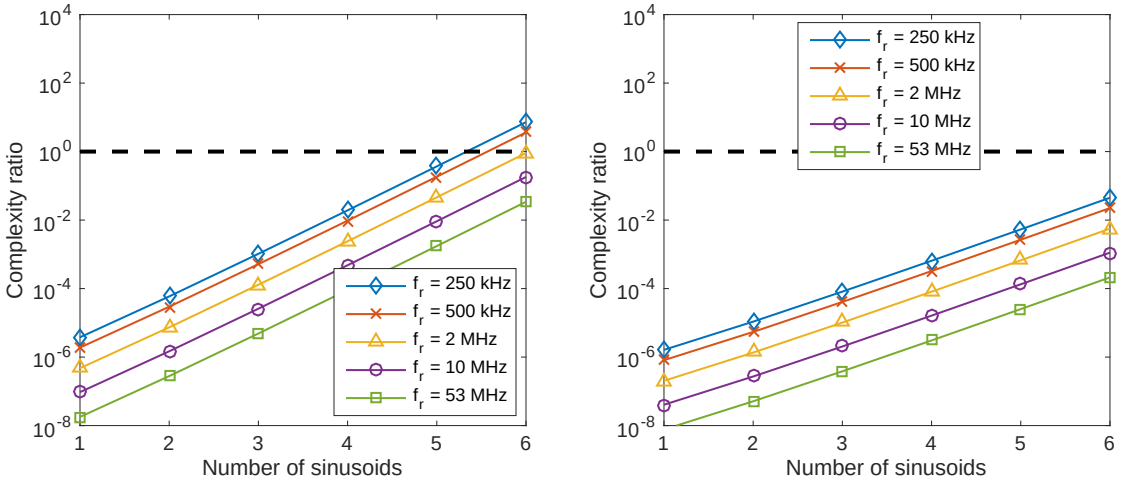


(a) (b)

Figure 3.10: Complexity ratio when $K = L$ is reduced to (a) 10, and (b) 4.

Based on the complexity formulas given above, it is obvious that the slope of the logarithmic complexity ratio increases with $K$ and $L$. Fig. 3.10 plots the complexity ratio as $K = L$ is reduced from 20, as in Fig. 3.9, to 10 and 4. The graph shows that our model can achieve further complexity reduction over the CTFT with fewer terms retained, or equivalently with higher synthesis error tolerance.

We conclude that for a small number of sines and cosines in the delay model, our spectrum model has less computational complexity. Exact complexity difference depend on system variables including $f_r$, $T_w$, the number of sinusoids in the displacement model, and synthesis error tolerance.

## 3.6 Conclusion

In this chapter, we have developed the first generic modeling framework for the reflected IR-UWB signal as it arrives at the radar receive antenna, for chest displacement due to arbitrary periodic heart and lungs motion. No assumption on the phase of these periodic movements has been made. Closed-form expressions of both the complex amplitude and frequency of each spectral component are provided. Our analysis shows that the radar received signal spectrum has components located at multiples of RR, multiples of HR, multiples of the burst repetition frequency, and their intermodulation products. Although the analysis is done assuming only a planar air-skin interface, extension to a multi-layered planar thorax model is straightforward through superposition.

For the sum-of-two-sinusoids chest displacement model, our analysis shows that the radar received signal spectrum comprises sparsely-located clusters, each of which has only a few significant components. The relative amplitudes of the components within a cluster are shown to vary significantly from cluster to cluster over the UWB band of 3 to 10 GHz and are a function of maximum chest displacement. Also, the previously reported aliased spectrum is shown to differ significantly from the un-aliased spectrum presented in this chapter. Practicality and usage of our analytical model is discussed in terms of the number of significant terms and numerical precision.

The presented model has several advantages over just using the CTFT. The CTFT expression does not reveal the locations of spectral components nor, because of the nonlinear nature of delay modulation, does it clarify how a particular sinusoidal component of the displacement function contributes to the spectrum. The cluster structure of our model al-

lows convenient inspection of cluster-to-cluster variations. This provides a foundation for the detection of particular patterns of breathing by comparing clusters. However, a limitation of our model is that the total number of multiplications in our model will exceed that of the CTFT for more complex displacement functions.

# CHAPTER 4
# HEURISTIC ALGORITHMS FOR HEART RATE AND RESPIRATION RATE ESTIMATION

When the HR fundamental frequency component is distorted or canceled by interference, such as RR harmonics, significant error in the estimation of the fundamental frequency occurs. Specifically, the strong RR harmonics often fall into the frequency band of the weaker HR fundamental, causing the the HR fundamental peak to be displaced or even canceled. In UWB-based vital signs estimation regime, most existing methods try to identify the fundamental component to estimate the HR and/or RR and overlook the harmonics [30, 31, 32, 11]. This chapter describes the Harmonic Path (HAPA) algorithm and the Spectrum-averaged Harmonic Path (SHAPA) algorithm that take advantage of the HR harmonics, where there is less interference, to achieve more reliable and robust estimation of the fundamental frequency.

## 4.1 Harmonic Path (HAPA) algorithm

In vital signs estimation with UWB radar, HAPA is the first reported algorithm to take advantage of the HR harmonics, where there is less interference, to achieve more reliable and robust estimation of the fundamental frequency. The HAPA algorithm is developed based on two simple yet fundamental observations: (1) the HR fundamental and its harmonics, which will be referred to in the sequel as the heart components, are equidistant and are separated by a frequency equal to the HR fundamental; and (2) each heart component is at a multiple of that inter-peak distance. In particular, HAPA will first detect in the spectrum a *path*, defined as a set of three or more consecutive approximately equally spaced spectral peaks, such that their frequencies are approximately an integer multiple of the average inter-peak distance in terms of frequency. Such a path is called a *harmonic path*.

Specifically, if the path has at least $\eta$ nodes whose frequencies are approximately a multiple $k$ of the average inter-peak distance (where "approximately" means the offset is within a specified margin $M_k$), this path is determined to be a *harmonic path*. The name comes from the fact that the path is formed with the harmonics of some fundamental frequency (the fundamental frequency may or may not be a part of the path). $\eta$ is an integer greater than or equal to 3 and is user-defined. The average inter-peak distance of the most powerful harmonic path is the rate estimate. A more detailed description of HAPA algorithm is given in Fig. 4.1.

HAPA takes advantage of all the significant heart components (the fundamental and the first few harmonics) to improve accuracy of the fundamental frequency estimate. The HR harmonics have less interference from the RR harmonics, therefore they can help average out the peak location error due to leakage and provide an accurate estimate of the HR even when the HR fundamental is completely missing. Another advantage of HAPA is its low processing complexity.

### 4.1.1 Methods and results

The measurement was conducted with a male subject of 200 lbs and age 42 at rest lying on his back on the top of a mattress. The UWB-based sensing device used was placed underneath the mattress.

In the digital signal processing step, eight consecutive samples are averaged to reduce noise, producing an effective sampling rate of 16 Hz. We then compute the DFT of each data block containing 256 such 16 Hz samples after DC removal and Hamming windowing. A data block overlaps with its previous block by 75%. The squared-magnitudes of the DFT of two consecutive blocks are averaged, and the average spectrum is interpolated using cubic spline interpolation with ratio four to alleviate the inherent coarseness in spectrum sampling of DFT, providing an approximation of a more finely-sampled version of the true spectrum. Therefore, an interpolated bin $n$ is equivalent to frequency $(60/64)n$ beats/min

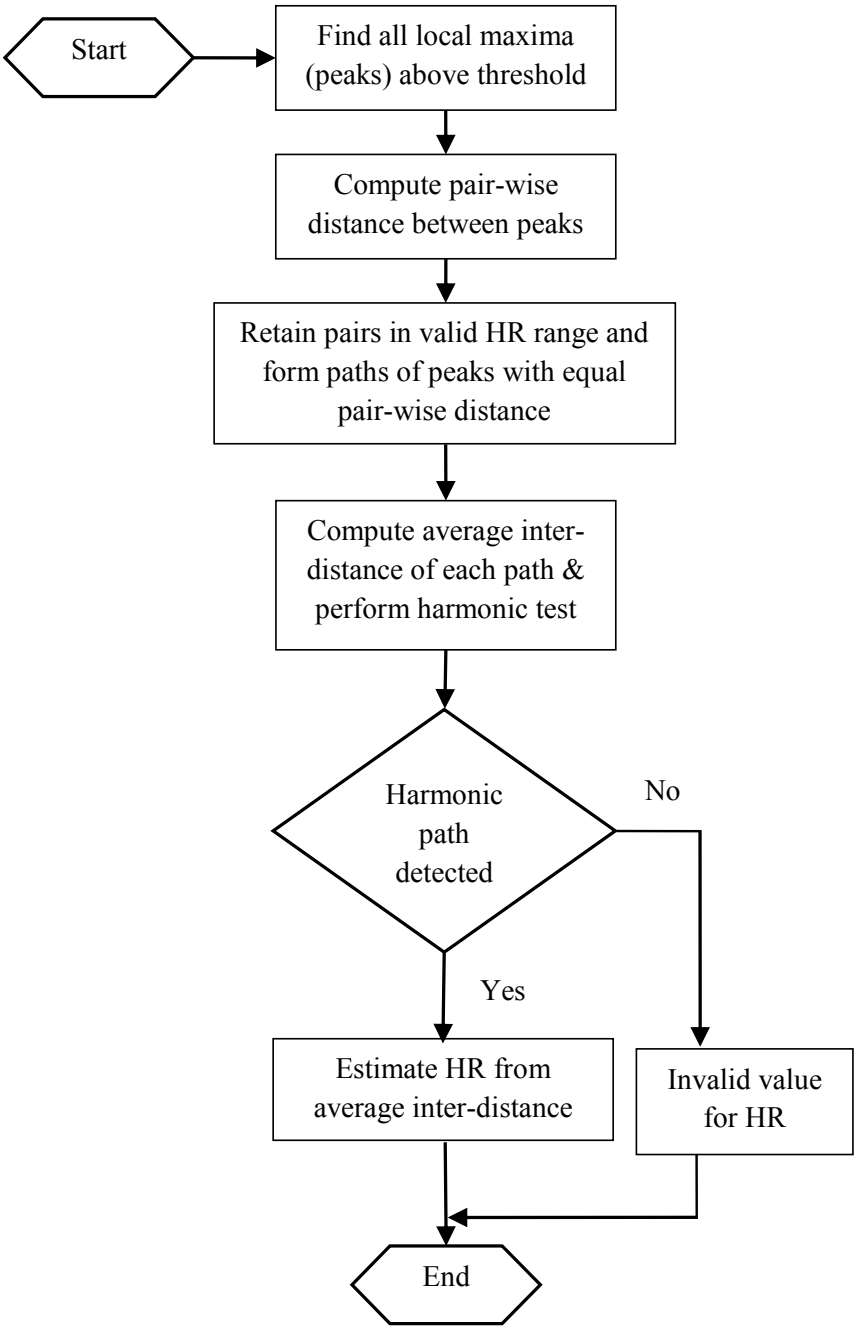


Figure 4.1: HAPA algorithm

or bpm. The time interval that spanned two consecutive blocks is called a *frame*.

HAPA is applied to the interpolated, averaged time-dependent spectra, providing real-time estimates of the HR. The preselected power threshold in the first step of HAPA (Fig. 4.1) is chosen to be the 75% percentile of all the interpolated averaged spectrum

points. We allow the disparity between the pair-wise (frequency) distances to be within 12 interpolated bins for them to be considered "almost equal" in the path-detecting step of Fig. 4.1. Such disparity margin accounts for the peak location error due to leakage from other spectral components in the spectrum and quantization error. In the next step, we choose $\eta$ to be 3, $M_1 = 5$ and $M_k = k + 1$ for $k = 2, 3, \ldots$ and the harmonic test is performed with the rounded average inter-peak distance in unit of interpolated bins. Examples of the interpolated, averaged spectra computed at different time instants are given in Fig. 4.2. The filled arrow represents the location of the HR fundamental obtained from the pulse-oximeter, the unfilled arrows represent its harmonics, and the horizontal line represents the preselected threshold in the HAPA algorithm. In Fig. 4.2a, the heart fundamental component happens to be the highest peak in the HR range, and both the global peak selection method and HAPA provide accurate estimates. In this case, the heart harmonic path detected by HAPA has frequencies (58, 116, 171, 229), yielding a HR estimate of bin 57 or about 53 bpm. However, in Fig. 4.2b, the HR fundamental component is not resolved from the nearby strong RR harmonic, and the global peak approach falsely selects this RR harmonic to be the HR estimate. In contrast, HAPA is still able to provide an estimate of the fundamental component. HAPA first detects two harmonic paths whose frequencies are (112, 170, 227) and (112, 227, 335), respectively, and then selects the former since it has highest average power per peak. In Fig. 4.2c, the HR fundamental component is severely attenuated due to leakage from other nearby spectral components, including RR harmonics. In this case, the first HR harmonic is the highest peak and therefore selected to be the HR estimate by global peak approach. In contrast, HAPA successfully detects the path (54, 108, 160, 213, 261), formed by the HR fundamental and its harmonic peaks, yielding the correct HR.

The HR estimates given by HAPA and the common global peak approach for the entire 132 seconds of recorded data are shown in Fig. 4.3. This data is from a male subject of 200 lbs and age 42 at rest lying on his back on the top of a mattress. The UWB radar sensing

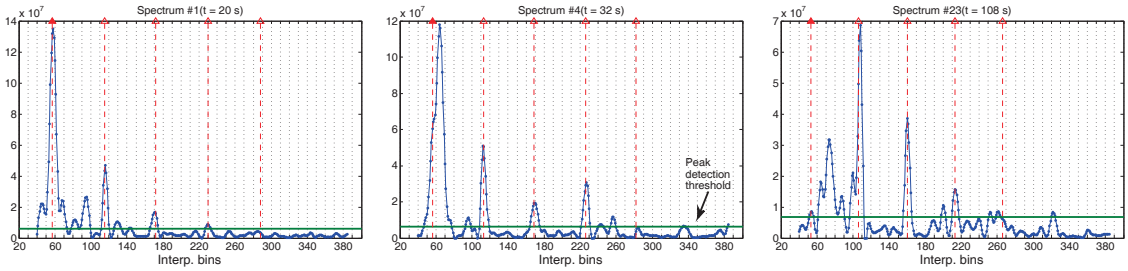


(a) (b) (c)

Figure 4.2: Examples of interpolated averaged spectrum of heart signal. The y-axis is the squared magnitude of DFT values. 1 bpm $= \frac{64}{60}$ interpolated bin. (a) "Clean" HR fundamental and harmonics, (b) Missing HR fundamental, and (c) HR fundamental is severely attenuated.

device was placed underneath the mattress. The synchronously obtained pulse-oximeter readings provide ground truth for evaluation of estimation accuracy, and are also shown. It is observed that the HAPA algorithm provides accurate estimates of the HRs whereas the global peak method provides many inaccurate estimates. Specifically, the RMSE and RMS normalized error (RMSnE) of HAPA are respectively 0.74 bpm and 1.43% compared to 26.38 bpm or 51.83% of the peak selection approach. The RMSnE is computed by first normalizing each estimation error by the its corresponding HR truth and then applying the root-mean-square operation on these normalized estimation errors.

RR estimation can also benefit from HAPA. In case of an otherwise motionless person, there is negligible spectral leakage from the HR fundamental since the RR fundamental is located in the lower band and is much stronger, thus we do not expect that HAPA will give much different estimation accuracy compared to the common global peak approach. However, regular body motion can induce a large amplitude and low frequency component [5] which can cause interference with the RR fundamental. For example, the global peak approach will select body motion component as the RR estimate if it happens to be stronger than the RR fundamental, unless the body motion component is cancelled in advance. In contrast, we predict that HAPA will provide accurate estimate of the RR without the need for body movement cancellation, at least in the moderate body movement case.

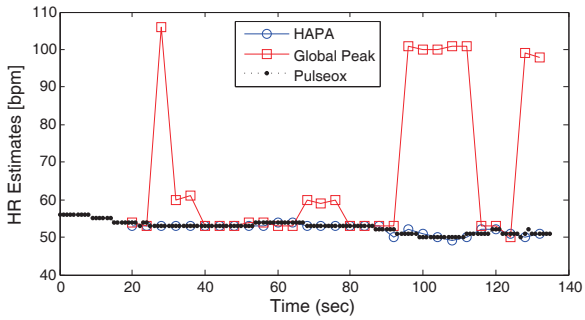


Figure 4.3: Heart rate estimates by HAPA and the global peak approach.

## 4.2 Spectrum-averaged Harmonic Path (SHAPA) algorithm

The HAPA algorithm requires the presence of at least three consecutive heart components to form a path. However, in some spectra, a path cannot be established due to nonappearance of one or a collection of harmonic peaks because they are masked by noise or interference. I term such a peak as *ghost peak*. Fig. 4.4 plots a heart spectrogram. The (normalized) spectrum points that are -40 dB from the highest peak are plotted with same color in Fig. 4.4a while in Fig. 4.4b the total power in a spectrum is normalized. It can be observed that the HR fundamental component and second harmonic vary rather smoothly with time, whereas the traces of the higher-order harmonics are occasionally broken. The HR harmonic path detected will often contain the HR components up to the fourth harmonic as the higher order harmonics are weak and will fall below the selection threshold. Hence, if either the second or third order harmonic is canceled or is visible but falls below the threshold, the correct path will not exist. The SHAPA algorithm fixes this shortcoming and recovers such ghost peaks by merging the current spectrum with a virtual spectrum synthesized from the past spectra to establish a path. The algorithm thus maintains a reference list of peak positions and powers of such a synthesized spectrum.

A more detailed description of SHAPA is given in Fig. 4.2. The algorithm starts by detecting harmonic paths in the spectrum as in the HAPA algorithm. HR is estimated from the average inter-peak distance of the most powerful harmonic path, and a reference list is updated with the peak positions and their respective magnitudes from the maxima list

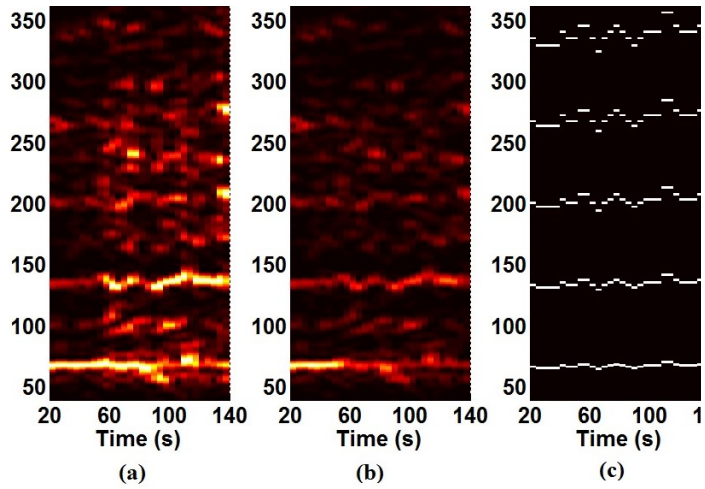


Figure 4.4: Heart rate spectrogram (a) Each spectrum normalized to its highest peak (b) Each spectrum is normalized so that the normalized spectrum points add up to a constant (c) Synthesized spectrogram of the ground-truth HR.

of the spectrum under consideration. If no harmonic path is found, information from the reference list is merged with the current maxima list. The process of merging is done by taking the average of peak positions which are close to each other. Specifically, the peak positions within 5 interpolated bins of each other are merged while others are kept without any change. The magnitude of the resultant merged peak takes the highest value of the constituent peaks. The almost equi-distant peak pairs are detected from the merged list and the process of detecting a harmonic path is repeated. If still no harmonic path is observed, an invalid value is assigned to the HR estimate. If two or more harmonic paths are found, the rate is estimated to be the average inter-distance of the path with highest average power per peak. As the procedure above repeats over time, the reference list will carry the information of all the spectra in the past up to the last spectrum from which a harmonic path is found without merging until SHAPA can detect a harmonic path from another spectrum without merging. In this case, the reference list will only contain the information (maxima list) from this successful spectrum.

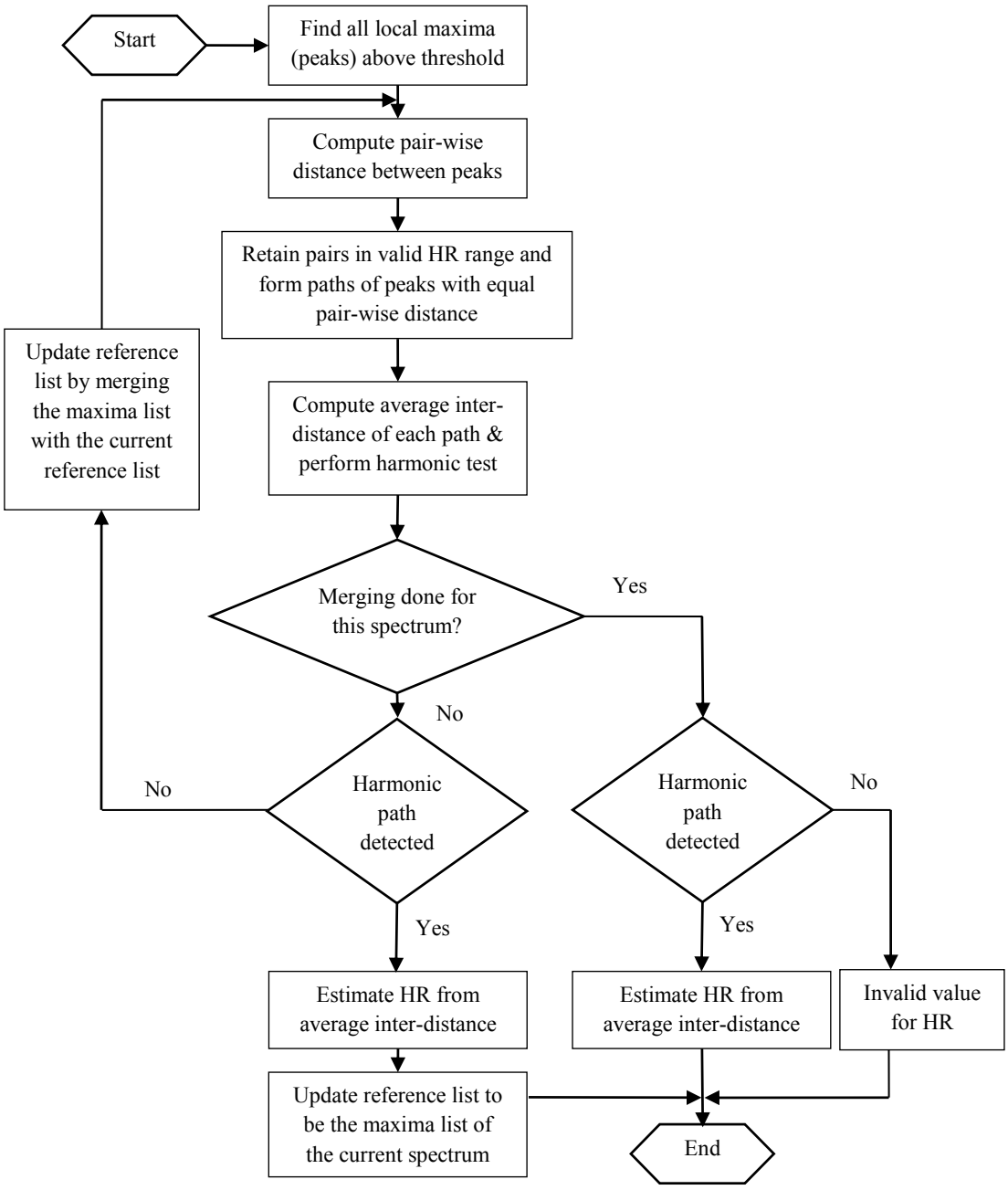


Figure 4.5: SHAPA algorithm

### 4.2.1 Methods

Measurements were conducted with eight subjects, aged $33.25 \pm 7.78$ and with BMI $29.39 \pm 4.91$, at rest lying on the top of a mattress. Among those, five lay on their back and three lay on their left side. The UWB radar sensing device was placed underneath the mattress.

Description of hardware and recorded heart and respiration signal channels is given in Section 1.4. Preprocessing of the recorded digital signals is described in Section 4.1.1.

### 4.2.2 Results

Two consecutive spectra are shown in Fig. 4.6. The dashed red vertical lines represent the locations of the HR fundamental and its harmonics, obtained from pulse-oximeter, while the horizontal line represents the threshold. In Fig. 4.6a, all the heart components are correctly detected in the harmonic path (68, 136, 204, 273), yielding an HR estimate of 64 bpm. The true HR is 64 bpm. The harmonics in the spectrum of Fig. 4.6b are masked by noise. The correct harmonic path is not detected in this case. However, the reference list containing information about peak positions in the previous spectrum (spectrum of Fig. 4.6a) is merged with the current spectrum's maxima list. SHAPA detects from the merged maxima list the correct harmonic path (69, 137, 208, 276), giving an HR estimate of 65 bpm and the true HR is 65 bpm. SHAPA algorithm is thus capable of recovering the missing components required for the harmonic test.

The HR estimates given by HAPA, SHAPA, and Global Peak (GP) algorithms and synchronously obtained pulse-oximeter readings, used as ground truth, of one subject are shown in Fig. 4.7. Note that an invalid estimate of HAPA or SHAPA is assigned a value of $-1$. Both HAPA and SHAPA are observed to outperform GP, and SHAPA makes possible a HR estimate when HAPA cannot find a harmonic path.

The RMSnE values of HAPA, SHAPA and GP algorithms with respect to pulse-oximeter readings for eight subjects are shown in Table 4.1. The total number of data frames of each subject is given in second column. The percentage of frames out of the whole data length for each subject where HAPA and SHAPA algorithms successfully detected a harmonic path are also shown in Table 4.1. Both algorithms produce comparable error performance and significantly outperform the GP method. The most notable improvement of SHAPA over HAPA is in terms of the 16% to 60% increase in performance from the HAPA algo-

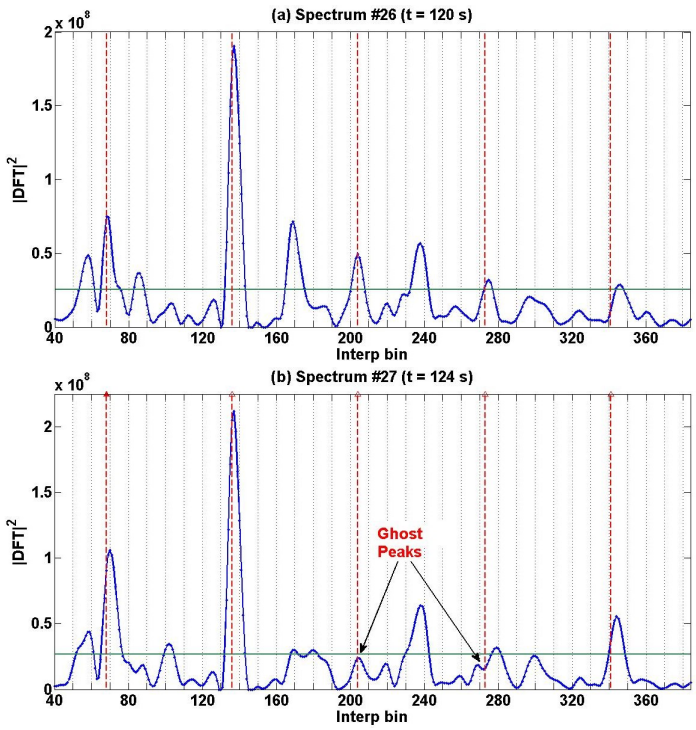


Figure 4.6: Examples of two consecutive averaged interpolated spectra (i.e., two consecutive frames). 1 bpm $= 64/60$ interpolated bins. (a) The fundamental and harmonics form a path (b) Ghost peaks are indicated.

rithm in terms of the percentage of data frames where a harmonic path is detected and an estimate is displayed. The SHAPA algorithm was designed under the assumption that the heart rate does not change abruptly. If that is the case and merging is required, it might yield an erroneous estimate. Both HAPA and SHAPA are practical for a real-time IR-UWB radar system. While we focus on only HR estimation here, RR estimation or any fundamental frequency estimation problem can also benefit from these algorithms.

## 4.3 Conclusion

In this chapter, two novel low-complexity algorithms, HAPA and SHAPA, have been proposed for HR and RR estimation. These two algorithms utilize harmonics to improve or provide the estimation of the fundamental frequency, which may be otherwise not possible, e.g. when the fundamental is missing or has peak location error due to interference. Exper-

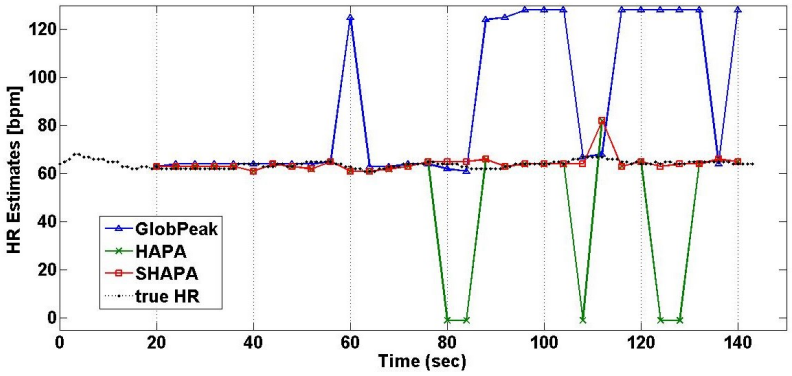


Figure 4.7: HR estimates by HAPA, SHAPA, and Global Peak algorithms of one subject

Table 4.1: RMSnE values for HAPA, SHAPA and Global Peak Algorithm for 8 subjects

| No. | Total frames | HAPA RMSnE | HAPA Detected (%) | SHAPA RMSnE | SHAPA Detected (%) | GP RMSnE |
|---|---|---|---|---|---|---|
| 1 | 29 | 0.013 | 100 | 0.013 | 100 | 0.518 |
| 2 | 31 | 0.049 | 83.87 | 0.046 | 100 | 0.617 |
| 3 | 56 | 0.234 | 82.14 | 0.268 | 100 | 0.322 |
| 4 | 32 | 0.120 | 56.25 | 0.113 | 87.5 | 0.359 |
| 5 | 29 | 0.254 | 58.62 | 0.241 | 96.55 | 0.327 |
| 6 | 30 | 0.086 | 63.30 | 0.089 | 90 | 0.130 |
| 7 | 28 | 0.266 | 39.29 | 0.222 | 96.43 | 0.188 |
| 8 | 28 | 0.132 | 21.43 | 0.130 | 82.14 | 0.132 |

imental results show that the proposed methods significantly outperform the global peak selection method, a common approach that suffers when the heart and respiration components interfere. Specifically, HAPA and SHAPA can provide an accurate HR estimate even when the HR fundamental is missing or has high peak location error due to leakage from nearby RR harmonics.

The SHAPA algorithm is an enhancement of the HAPA algorithm, incorporating information from the previous spectrum when the fundamental or harmonics are masked by noise. SHAPA produces errors that are comparable to HAPA, which does not utilize the previous spectrum. The most notable improvement of SHAPA over HAPA is in terms of the 16% to 60% increase in the number of valid estimates. These algorithms can also improve RR estimates and are practical for a real-time IR-UWB radar system.

# CHAPTER 5

# SEQUENTIAL BAYESIAN FILTERING FOR HEART RATE AND RESPIRATION RATE ESTIMATION

Tracking enhances robustness of an estimation algorithm. SHAPA is our early effort to move towards tracking, but it is a rather *ad-hoc* approach. In this chapter, application of sequential Bayesian filtering [75], a systematic tracking approach, to the tracking of HR and RR is presented.

The proposed algorithm leverages tracking, heart rate harmonics, respiration rate harmonics, and motion-artifacts removal to estimate the HR from the IR-UWB radar signal. For tracking, the grid-based method, a special case of sequential Bayesian filtering, is used. Unlike most existing works, state transition model and likelihood model are learned from data, making our approach data-driven. The algorithm suite comprises several steps: (1) preprocessing of data to remove motion-artifacts, (2) extraction of spectral features that a heart rate and respiration rate impose onto data, (3) learning the required densities for Bayesian filtering through training, (4) estimation of heart rate. Error performance is evaluated using cross-validation on experimental data collected from 26 subjects. A mean absolute error of $3.17$ bpm is achieved.

## 5.1 Introduction

Many problems require estimation of the state of a system that changes over time using noisy measurements on the system. The Bayesian recursive framework is suitable for these problems. Such a dynamic system can be described by a state-space model, where the state vector represents all relevant information required to describe the system of interest and the measurement vector contains noisy observations that are related to the state vector.

### 5.1.1 Nonlinear Bayesian tracking

Let $\mathbf{x}_k$ and $\mathbf{z}_k$ be, respectively, the state and measurement at time $k$. Bayesian filtering involves constructing the posterior density $p(\mathbf{x}_k|\mathbf{z}_{1:k})$ of the state $\mathbf{x}_k$ based on all available measurements $\mathbf{z}_{1:k}$. Here we use the notation $\mathbf{z}_{1:k} = \{\mathbf{z}_1, \mathbf{z}_2, \ldots, \mathbf{z}_k\}$. Various kinds of estimates of the state can be computed by taking certain statistics of the posterior such as the mean, mode, or median.

Sequential Bayesian filtering is a recursive approach that sequentially updates the posterior distribution of the state once a new measurement arrives rather than processing all measurements in batch. Recursive processing has advantages over batch processing since the former does not require storage of all available data and does not need to reprocess all data when a new measurement arrives.

The general state space model is expressed as

$$\mathbf{x}_k = f_k(\mathbf{x}_{k-1}, \mathbf{v}_{k-1}^x)$$

$$\mathbf{z}_k = h_k(\mathbf{x}_k, \mathbf{v}_k^z)$$

where $f_k(\cdot)$ and $h_k(\cdot)$ are possibly nonlinear functions. $\mathbf{v}_{k-1}^x$ is an independent process noise sequence with known statistics. $\mathbf{v}_k^z$ is an independent observation noise sequence with known statistics. Assume the initial prior $p(\mathbf{x}_0|\mathbf{z}_0) = p(\mathbf{x}_0)$ is known.

In principle, the posterior density $p(\mathbf{x}_k|\mathbf{z}_{1:k})$ can be obtained via the recursion:

$$\text{Prediction (a-priori): } p(\mathbf{x}_k|\mathbf{z}_{1:k-1}) = \int p(\mathbf{x}_k|\mathbf{x}_{k-1}) p(\mathbf{x}_{k-1}|\mathbf{z}_{1:k-1}) d\mathbf{x}_{k-1}$$

$$\text{Update (a-posteriori): } p(\mathbf{x}_k|\mathbf{z}_{1:k}) = \frac{p(\mathbf{z}_k|\mathbf{x}_k) p(\mathbf{x}_k|\mathbf{z}_{1:k-1})}{p(\mathbf{z}_k|\mathbf{z}_{1:k-1})} = \frac{p(\mathbf{z}_k|\mathbf{x}_k) p(\mathbf{x}_k|\mathbf{z}_{1:k-1})}{\int p(\mathbf{z}_k|\mathbf{x}_k) p(\mathbf{x}_k|\mathbf{z}_{1:k-1}) d\mathbf{x}_k}$$

The prediction step uses the state transition density $p(\mathbf{x}_k|\mathbf{x}_{k-1})$ associated with the state transition model (5.1.1) to predict forward. This in effect deforms and diffuses the state pdf. The update step incorporates the observation through the likelihood $p(\mathbf{z}_k|\mathbf{x}_k)$ to tighten this

diffused density.

In each recursion, the optimal estimate with respect to a particular criterion can be generated from the posterior. For example, the posterior mean gives the Minimum Mean-Squared Error (MMSE) estimate, and the posterior mode gives the Maximum a-posteriori (MAP) estimates.

In general, the posterior density cannot be determined analytically, and its approximation is sought using various algorithms such as the Extended Kalman Filter and particle filters. Closed-form solution of the posterior density exists for a restrictive set of cases including the Kalman filter [76] and the grid-based methods.

### 5.1.2 Grid-based methods

Exact closed-form expression of the posterior density $p(\mathbf{x}_k|\mathbf{z}_{1:k})$ can be obtained if the state space is discrete and consists of a finite number of states. This is the basic of the Grid-based methods [75].

Suppose the state space at time $k-1$ consists of discrete states $\mathbf{x}_{k-1}^i$, $i = 1, \ldots, N_s$. Let $w_{k-1|k-1}^i = \Pr(\mathbf{x}_{k-1} = \mathbf{x}_{k-1}^i|\mathbf{z}_{1:k-1})$, the conditional probability of a state $\mathbf{x}_{k-1}^i$ given measurements up to time $k-1$. Then the posterior density at time $k-1$ can be expressed as

$$p(\mathbf{x}_{k-1}|\mathbf{z}_{1:k-1}) = \sum_{i=1}^{N_s} w_{k-1|k-1}^i \delta(\mathbf{x}_{k-1} - \mathbf{x}_{k-1}^i)$$

where $\delta(.)$ is the Dirac delta function.

At time $k$, the prior density and posterior density are given as [75]

$$\begin{aligned} p(\mathbf{x}_k|\mathbf{z}_{1:k-1}) &= \sum_{i=1}^{N_s} w_{k|k-1}^i \delta(\mathbf{x}_k - \mathbf{x}_k^i) \\ p(\mathbf{x}_k|\mathbf{z}_{1:k}) &= \sum_{i=1}^{N_s} w_{k|k}^i \delta(\mathbf{x}_k - \mathbf{x}_k^i) \end{aligned} \tag{5.1}$$

where $w^i_{k|k-1} \triangleq \sum_{j=1}^{N_s} w^j_{k-1|k-1} p(\mathbf{x}^i_k|\mathbf{x}^j_{k-1})$, and

$$w^i_{k|k} \triangleq \frac{w^i_{k|k-1} p(\mathbf{z}_k|\mathbf{x}^i_k)}{\sum_{j=1}^{N_s} w^j_{k|k-1} p(\mathbf{z}_k|\mathbf{x}^j_k)} \tag{5.2}$$

## 5.2 Description of experimental data

The experimental data were taken from a total of 26 subjects under the Georgia Tech IRB Protocol H13206 and were provided by Sensiotec Inc. [5]. The subject population included both genders, with age range of 27-60 years old. Each subject was reclined on a mattress with an IR-UWB radar device placed underneath, as shown in Fig. 5.1. A schematic of such a radar system is shown in Fig. 6 of [5], and a simplified diagram of this schematic is shown in Fig. 1.4. During certain intervals of time the subject did certain activities. At some point they lay on their back. At other points in time they turned over onto their left side, right side, or stomach. Some of the subjects also did various other activities such as talking and making hand movements. Therefore, our data represent some natural behaviors of patients in bed. We were able to observe those activities and mark the time when they occurred. Pulse oximeter readings were used as an HR reference.


Figure 5.1: Experiment setup. The radar device is placed underneath the mattress.

Our recorded IR-UWB radar signal has the following challenging properties.

- Low SNR
- Intermittent patient motion
- Some un-modeled radar system characteristics including full characterization of the transmitted pulse, multiple layers of the body, and possible nonlinearities in the radar RF front-end and external interference
- Highly interfered by RR harmonics and body motion corruption

Fig. 5.2a and Fig. 5.2b show examples of clean and corrupted data. Each is a 20-second frame of our recorded data. In each figure, the heart signal, respiration signal, and the heart spectrum are plotted. In Fig. 5.2a, a clean example, the true HR (shown in red dashed line) is the highest peak in the spectrum, and the common highest-peak method works. However, in Fig. 5.2b, a corrupted example, there is no peak at the true HR and there are a plethora of strong peaks surrounding the true HR. Estimating the HR from the spectrum in this case is challenging; the simple highest-peak method gives an error of around 20 bpm.

## 5.3 Bayesian filtering applied to IR-UWB radar vital signs data

The IR-UWB radar signal contains a mixture of HR harmonics, RR harmonics, and possibly their intermodulation products, as analyzed in Chapter 3. These components can locate closely to each other in the frequency domain, causing much ambiguity if the HR is to be detected. In addition, HR estimation its vulnerable to body movement, such as limb movement, which is far greater in amplitude than the heart movement. Such motion makes the "torso-movement" reading corrupted and HR estimation prone to errors. Overall, the presence of multiple peaks due to HR harmonics, RR harmonics, noise, body movement, and unmodeled phenomena in the spectrum causes high ambiguity, hence, the simple method of using the highest peak to indicate the HR estimate is prone to errors. Therefore, finding features that accentuate the true HR fundamental component while dimming the non-HR components is desirable. Our observation model applies this principle.

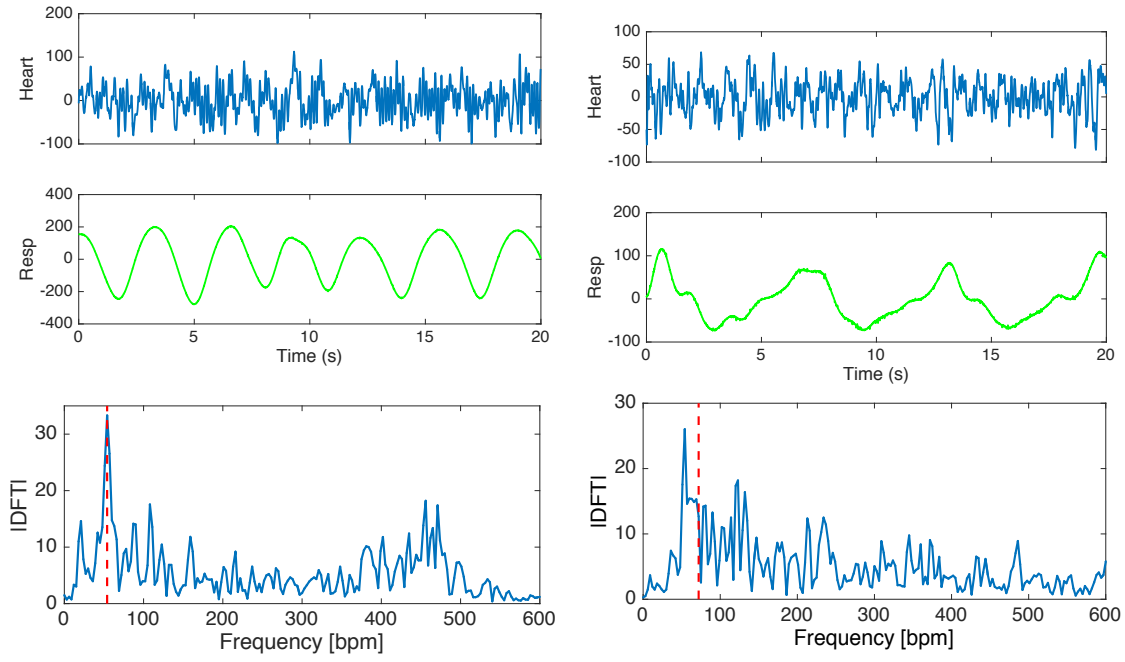


(a) (b)

Figure 5.2: (a) An example of relatively uncorrupted data. (b) An example of severely corrupted data. For both (a) and (b), (top) Heart signal, (middle) Respiration signal, (bottom) Heart spectrum

Typically, HR is quantified by bounded integers in unit of beats per minute (bpm). Therefore, if HR is chosen as the state of the dynamic system, the state space is discrete and consists of a finite number of states. For example, a reasonable choice for a state space of normal adult HR is $\{45, 46, \ldots, 120\}$ [bpm], and we will assume this state space in the remaining of this chapter, unless otherwise noted. Thus, we apply the grid-based method in Section 5.1.2 to recursively compute the posterior density.

As in Chapter 4, the sliding frame concept with step size of a fraction of the frame length is used. HR estimation is attempted in each frame. Sequential Bayesian tracking requires the state transition density and the likelihood model, which are obtained from the state transition model and the measurement model. The procedure below applies to the heart signal frames. Application to respiration signal frames is noted whenever applicable.

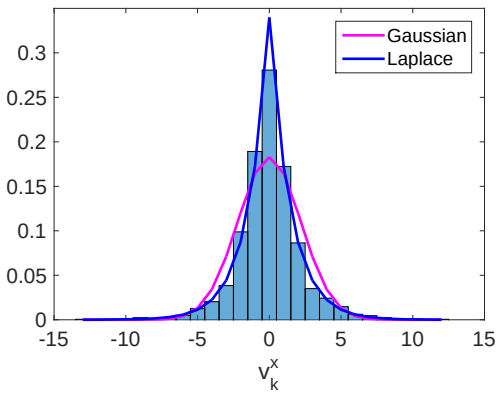


Figure 5.3: Process noise histogram and fitted densities.

### 5.3.1 State transition model

Let a scalar state $x_k$ be the HR in bpm. The state transition model is selected to be an AR-1 model [36, 38]:

$$x_k = x_{k-1} + v^x_{k-1}, \tag{5.3}$$

where $\{v^x_{k-1}; k = 1, 2, \ldots\}$ is an independent process noise sequence. In order to obtain the statistics of the process noise, the pulse oximeter readings are sampled every 4 seconds, the consecutive differences are computed, and the histogram of the difference population is formed as shown in Fig. 5.3. By inspection, two standard distribution families can approximate this histogram: a Gaussian distribution with zero mean and some variance, and a Laplacian distribution centered at zero and having the scale parameter determined by the variance. An approach to obtain the specific values for these parameters is maximum likelihood estimation (MLE). The two densities with parameters obtained by MLE are overlaid onto the histogram in Fig. 5.3. However, instead of subjectively selecting one of these densities to model the process noise distribution, we parameterize the choice of distribution and its variance parameter, and optimize them in a training phase.

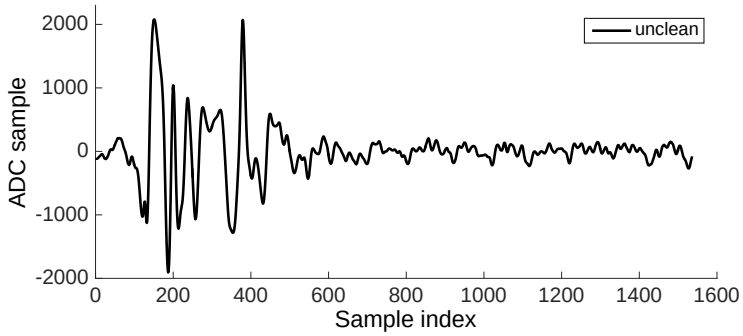


Figure 5.4: The IR-UWB radar received signal with motion corruption in the first quarter, indicated by the excessive amplitude.

### 5.3.2 Feature extraction

Since we have limited amount of data, we cannot use the big data approach available in some software packages to generate features for us. Therefore, we have to use our understanding of physical model to design a feature, and make it our observation. Our feature is determined from what we called a *score*.

*Motion-artifacts removal*

Body movements, such as limb movements, cause samples to have excessive amplitude, which can lead to errors in HR estimation. Two typical non-motion-corrupted frames are shown in Figures 5.2a and 5.2b, and a motion-corrupted heart signal frame is shown in Fig. 5.4. One approach is to discard a motion-corrupted data frames and cease estimation until a motion-free frame is observed, but this can lead to frequent interruption of HR estimation. To improve the continuity of HR estimation, a method to remove motion-artifacts from the signal is applied.

In each data frame, the average of the samples is subtracted from each sample. To remove motion artifacts, samples with excessive amplitude are set to 0. Specifically, a sample is set to zero if its absolute value exceeds a motion threshold $\lambda$, which is defined as

$$\lambda = \begin{cases} \lambda_{min} & \text{if } \lambda_\rho < \lambda_{min} \\ \lambda_\rho & \text{if } \lambda_{min} \leq \lambda_\rho \leq \lambda_{max} \\ \lambda_{max} & \text{if } \lambda_\rho > \lambda_{max} \end{cases} \tag{5.4}$$

where $\lambda_\rho$ is the $\rho^{\text{th}}$ percentile of the absolute samples, and $\rho,\ \lambda_{min}$, and $\lambda_{max}$ are tunable parameters. It is crucial to have an adaptive threshold to determine which amplitude is considered as motion corrupted, as the signal peak-to-peak amplitude can vary over time. For example, it is observed that the signal peak-to-peak amplitude is smaller when the patient lies on the side compared to laying on the back.

Next, the average of the non-zero samples in the resulting frame is computed, and the average is subtracted from these samples. If the ratio of the number of zeros and the total number of samples of the frame exceeds $\gamma$, where $\gamma$ is another tunable parameter, the frame is declared motion corrupted and no further computation is conducted. Otherwise, the power spectrum of the frame data is estimated as follows.

*Spectrum estimation*

A Hanning window is applied to the frame. The frame is then split into two windows overlapping by $50\%$. The DFT of each window is computed. The spectrum is computed by taking the average of the magnitudes of the two DFTs. A computed respiration spectrum and heart spectrum are shown in Figures 5.5a and 5.5b, respectively.

*Score*

A modified spectrum can be constructed by summing the amplitudes of the harmonics of each fundamental frequency *candidate* [35, 34]. We further modify this harmonic-sum spectrum by taking into account the possible presence of the RR harmonic. The modified

harmonic sum of a frequency $x$ is defined as

$$\tilde{S}(x) = b \cdot \text{spec}(x) + \sum_{l=2}^{H} \text{spec}(lx), \tag{5.5}$$

where spec$(lx)$ is the spectrum value at the frequency $lx$ [1] , and b is a function defined as

$$b(x, \hat{f}_b) = \begin{cases} 1 & \text{if } \min\limits_{n \in \{1,2,3,4\}} |x - n\hat{f}_b| > \delta \\ b_0 & \text{otherwise} \end{cases},$$

where $\hat{f}_b$ is the RR estimate of the frame, obtained by taking the highest peak in the respiration spectrum, and $\delta$ and $b_0 \in [0, 1)$ are two parameters. The function $b(x, \hat{f}_b)$ imposes a constraint that when a state $x$ is too close to a RR harmonic of up to order 4, only a fraction of the fundamental power contributes to its modified harmonic sum. This can prevent a strong RR harmonic in the heart spectrum (see Fig. 5.5b) from dominating other fundamental candidates. By weighing down the score of a frequency candidate if it is in the vicinity of a RR harmonic, this model can avoid mistakenly selecting a RR harmonic as the HR estimate. On the other hand, by incorporating the powers of the higher order harmonics, this model avoids the drawback of existing works [9, 29], which completely rules out a HR frequency candidate if it is at or near a RR harmonic.

A feature, called *score*, of a state $x$ is defined as

$$S(x, \hat{f}_b) = \frac{\tilde{S}(x, \hat{f}_b)}{\max\limits_{\nu \in \mathcal{X}} \{\tilde{S}(\nu, \hat{f}_b)\}}. \tag{5.6}$$

where $\mathcal{X}$ is the discrete, finite state space. The scores of all the states $\mathcal{X}$ form a score vector. Here $\mathcal{X} = \{45, 46, \ldots, 120\}$.

Fig 5.5 displays the spectral computations in a frame. Fig. 5.5a shows the respiration spectrum computed from the respiration signal. The RR estimate is selected to be the

[1] If $lx$ does not equal a DFT bin frequency, linear interpolation is used.

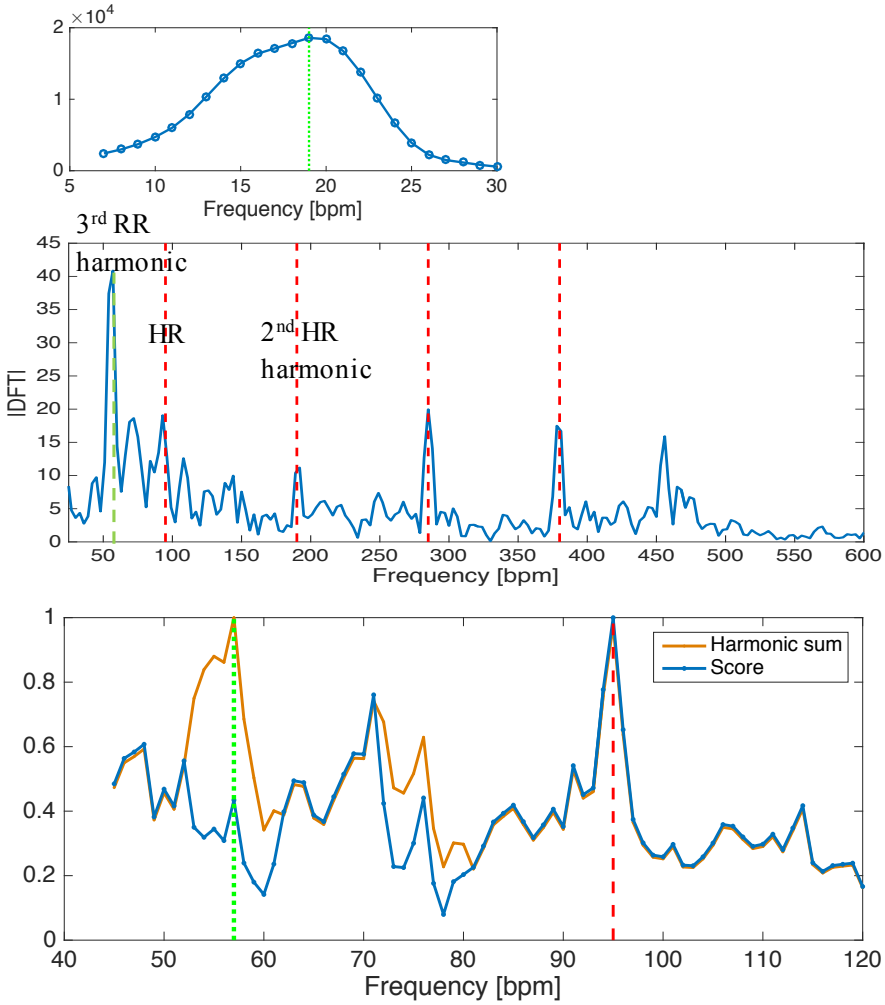


Figure 5.5: Spectral computations in a frame: (a) the respiration spectrum, with green dotted line indicating the RR estimate, (b) the heart spectrum with red dashed lines indicating the harmonics of the pulse oximeter reading and a green dotted line indicating the third-order RR harmonic, (c) The harmonic sum normalized to the highest value, and the score function. The red dashed line indicating the pulse oximeter reading.

highest peak in the spectrum and is shown in dashed green line. The heart spectrum is shown in Fig. 5.5b, where a strong third-order RR harmonic (dashed green line) is clearly observed at $59$ bpm. The harmonic sums of each state in the state space corresponding to the heart spectrum in Fig 5.5b is plotted by the light orange curve in Fig. 5.5c. Simply adding all harmonics of this peak including the first order (fundamental) harmonic will give this peak the highest score compared to other state candidates. The score model (5.6) takes into account the RR harmonic information and correctly penalizes this peak. Note that in

this figure the harmonic sum vector is normalized to the highest harmonic sum value. In the same plot, the scores are shown in bold blue. The harmonic sum function has the highest peak at a state different than the pulse oximeter HR (shown in red dashed line). In fact, this highest peak is located at the third-order RR harmonic (shown in green dashed line). In contrast, our score function maxes at the pulse oximeter HR. It can be observed that the score vector is a more robust spectral form than the conventional DFT.

### 5.3.3 Observation model

In this section, an observation model is proposed and a data-driven likelihood model is built from training data by investigating the statistics of the scores of the true HR.

The observation model is proposed as

$$z_k(x_k, \hat{f}_{b_k}) = \max_{u \in [x_k - E, x_k + E]} S(u, \hat{f}_{b_k}), \tag{5.7}$$

where $\hat{f}_{b_k}$ is the RR estimate at frame $k$, and $E$ is the maximum error of the pulse oximeter. The presence of $E$ in the observation model is because the pulse oximeter readings, although to be used as ground truth, have inherent measurement error, especially when its photoplethysmography signal contains motion artifacts from patient's body movements [77]. Pulse oximetry is known to be vulnerable to motion artifacts [77]. In many of our experimental data sets, the subjects moved. Fig. 5.6 illustrates the observation model correspond to the score vector in Fig. 5.5c.

To find the likelihood model $p(z_k|x_k)$, the statistics of $z_k(x_k, \hat{f}_b)$ are investigated for $x_k$ being the pulse oximeter reading of frame $k$. The histogram of $z_k(x_k, \hat{f}_b)$ is shown in Fig. 5.7. Based on this histogram, we model $z_k$ to follow a customized exponentiated

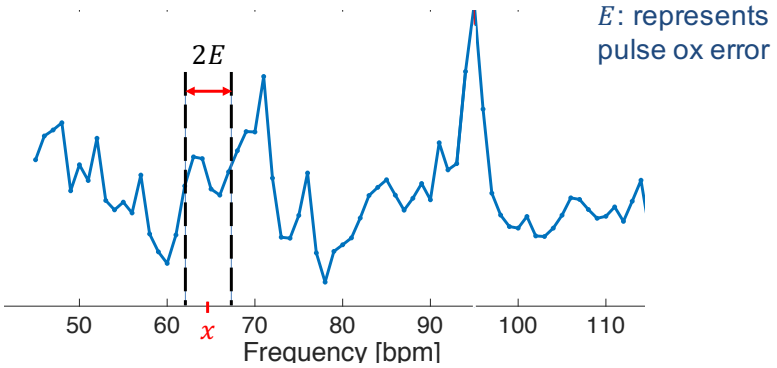


Figure 5.6: Illustration of the observation model (5.7)

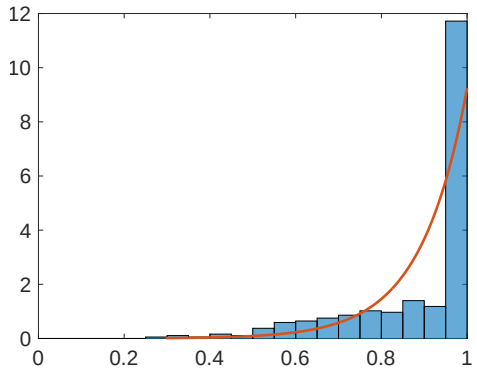


Figure 5.7: Histogram of $z_k$

exponential PDF with a finite region of support:

$$p_z(\zeta) = \begin{cases} C(\alpha, \beta, a, b) e^{\alpha \zeta^{\beta}} & , \zeta \in [a, b] \\ 0 & \text{otherwise} \end{cases}, \tag{5.8}$$

where $[a, b]$ is the region of support of all the $z_k$ values, $C(\alpha, \beta, a, b)$ is a deterministic term that ensures the pdf integrates to 1, and $\alpha$ and $\beta$ are tunable parameters.

When a new frame is observed and the associated score vector is computed, (5.7) is evaluated for all $x \in \mathcal{X}$, and the resulting values are substituted into (5.8) to get the likelihood of the states. Note that $C$ needs not be specified in (5.8), as the posterior density, which is proportional to the product of the prediction density and the likelihood, will eventually be normalized to integrate to 1 (Eq. (5.1) and (5.2)).

### 5.3.4 HR estimation

The posterior density is computed recursively for every frame using the grid-based methods. The HR estimate is selected as the median of the posterior density.

### 5.3.5 Parameter selection and performance evaluation method

A set of parameters are needed in the presented algorithm. We use the sliding frame of length $T = 20$ s with a step size of $\Delta T = 4$ s. The other parameters, listed in the first two columns of Table 5.1, are optimized using a search heuristic such as the genetic algorithm [78] rather than assigned with heuristic values.

However, optimizing a vector of parameters on all the data and reporting the error of the algorithm with the optimized parameter vector might be prone to overfitting, a phenomenon where an algorithm performs very well on the data that are used to train it but consistently fails with unseen data [79, 80]. To determine the generality of an algorithm, it needs to be tested on an independent data set which has not been used to specify its models and parameters. This is usually done by the method of cross-validation [79, 80].

Among various cross-validation implementations, we use the approach that consists of three phases: training, validation, and testing. The subjects are grouped into 6 exclusive subsets such that their data are of almost equal length (since data lengths of different subjects are different). One subset is randomly selected and set aside as the unseen set, or test set. The remaining 5 subsets, which will be referred to as "folds" in the sequel, are used for training and validation.

In one round, one fold is selected to be the validation set, and the other four are chosen to be the training set. The genetic algorithm, which is an iterative search heuristic, is applied to the training set. In each iteration, the proposed HR estimator is evaluated with a number of values of the parameter vector, and the one that gives the lowest cost, which we choose to be the mean absolute error (MAE), is selected to be the best parameter vector of the current iteration. Using this best parameter vector, the HR estimator is then applied

Table 5.1: Trained parameters

| Description | Parameter | Search range | Genetic algorithm output |
|---|---|---|---|
| Min motion ratio | $\gamma$ | [0.05 0.60] | 0.1328 |
| Percentile | $\rho$ | [70 99] | 88 |
| Lower bound | $\lambda_{min}$ | [100 400] | 298 |
| Upper bound | $\lambda_{max}$ | [200 800] | 527 |
| No. harmonics | $H$ | [1 6] | 4 |
| RR separation | $\delta$ | [0 6] | 4 |
| Fundamental weight | $b_0$ | [0 1] | 0.1270 |
| Max pulse ox error | $E$ | [0 9] | 2 |
| Transition PDF | $D$ | [Laplacian, Gaussian] | Gaussian |
| Variance | $Q$ | [0.1 16] | 2.5102 |
| LLH parameter | $\alpha$ | [0.05 10] | 6.8880 |
| LLH parameter | $\beta$ | [0.05 10] | 1.2286 |

on the validation set, and the resulting MAE is the validation error of this iteration. Once either the maximum number of iterations is reached or the genetic algorithm converges, the iteration with the smallest validation error is identified, and the best parameter vector of that iteration is selected for evaluating the HR estimator with the test set, which we had set aside in the beginning. The resulting MAE is the test error of this round.

The procedure is repeated for the other four rounds, in each of which a different fold is selected as the validation set and the remaining four folds become the training set. The overall performance can be quantified as the average test error, computed by averaging the test errors of the five rounds. The search ranges of the trained parameters are given in the third column of Table 5.1.

## 5.4 Results and discussion

Table 5.2 shows the test error (i.e., the MAE) and its associated error standard deviation of each of the five rounds described in Section 5.3.5. Fig. 5.8 shows the HR estimates of the subject with the longest data record in the test set for the "best" round and "worst"

Table 5.2: Test error (MAE) and the associated standard deviation

| Round | Test error (MAE, bpm) | Stdev (bpm) |
|---|---|---|
| 1 | 2.54 | 4.22 |
| 2 | 2.78 | 3.65 |
| 3 | 3.56 | 5.40 |
| 4 | 3.27 | 4.22 |
| 5 | 3.68 | 3.81 |
| Average | 3.17 | 4.26 |

round in Table 5.2. During the experiment, this subject performs a series of activities including talking, arm movements and turns, as listed in Table 6.1. Here "best" and "worst" means that the sum of the test error and the error standard deviation is lowest and highest, respectively. Thus, rounds 2 and 3 are the best and worse rounds, respectively. The HR estimates of rounds 2 and 3 are shown in Fig. 5.8a and Fig. 5.8b, respectively. It can be observed that, in both cases, the proposed HR estimator starts at an incorrect HR value. Recall that in the proposed algorithm, in the first frame, which corresponds to the first Bayesian recursion, the posterior density is the likelihood function scaled by a constant, because the state transition density is a constant. Thus, the first estimate is solely dependent on the likelihood function, and in this case, leads to an estimate of 78 bpm whereas the truth is 64 bpm. However, as more recursion steps occur, equivalently as more observations are made, the HR estimates approach the truth curve.

We observe that the pulse oximeter reading jumps 9 bpm, from 65 bpm at 1284 s to 74 bpm at 1292 s. This suggests that the pulse oximeter readings are erroneous at times. We, however, do not change these pulse oximeter readings when evaluating our HR estimator performance.

The average test error, computed by averaging the test errors of the five rounds, is 3.17 bpm. The pulse oximeter device datasheet indicates an accuracy of 2 bpm.

Regarding statistical significance of the reported error performance, note that the test set and the folds each contains approximately 600 frames of four to five subjects, thus the

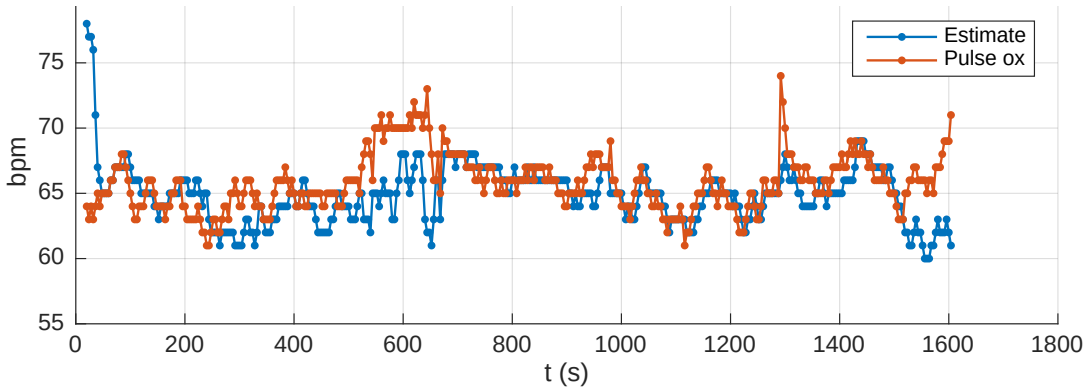


(a)

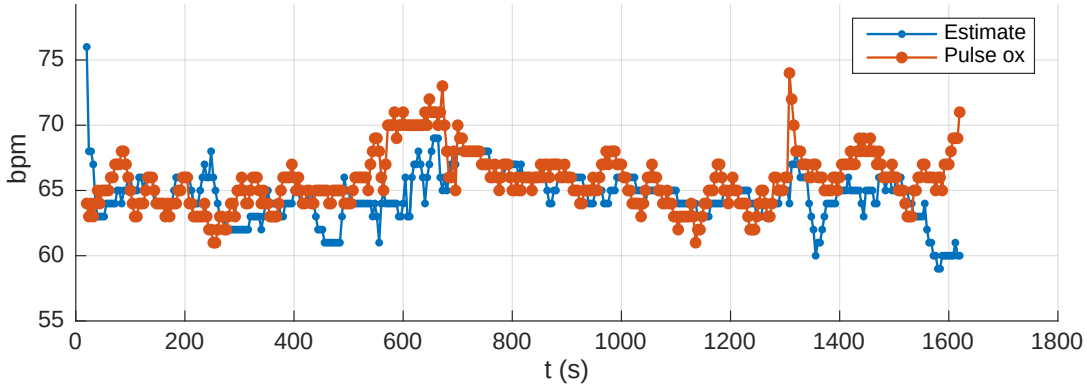


(b)

Figure 5.8: HR estimates of Rounds 2 (best) and 3 (worst) of Table 5.2

validation errors and test errors are computed over large sample sizes. The performance of published works on HR estimation with IR-UWB radar is presented in Table 5.3. Note that the accuracy reported in these works is instantaneous, because it is evaluated from only one frame per subject for one or only a few subjects.

The parameter values optimized by the genetic algorithm over all available data are given in the last column of Table 5.1, respectively.

The presented approach is feasible for the type of signal that carries multiple HR harmonics. The score feature, which defines the observation, is specifically designed to avoid mistakenly selecting a RR harmonic as the HR estimate, yet still be able to recognize a HR at or near a RR harmonic by incorporating the powers of the higher harmonics of the HR,

Table 5.3: Reported HR estimation accuracy in the literature

| Reference | No. subjects* | No. frames per subject | MAE (bpm) |
|---|---|---|---|
| This work | 26 | 138** | 3.17 |
| [9] | 3 | 1 | 1.11 |
| [81] | 3 | 1 | 1.56 |
| [8] | 4 | 1 | 5.00 |
| [14] | 2 | 1 | 0 |
| [31] | 3 | - | 3.68 |
| [70] | 4 | 1 | Only HR estimates reported, no truth given |
| [82] | 2 | 1 | Only HR estimates reported, no truth given |
| [83] | 4 | - | Only chest displacement reported |
| [84] | 1 | - | HR accuracy not reported |
| [11] | 5 | - | HR accuracy not reported |
| [10] | 3 | - | HR accuracy not reported |
| [45] | 2 | - | HR accuracy not reported |

* In some studies, the same subject participated in several experimental sessions. In this case, "No. subjects" is equal to the number of sessions.
** Average value

as has been demonstrated in Fig. 5.5. The feature definition can be modified to better suit the signal content.

A limitation of the proposed algorithm is that the current likelihood model is multi-modal, thus introduces ambiguity. Furthermore, it does not take into account the harmonic power (i.e., the score) of the other states not in its immediate vicinity of $[-E, E]$. Revisions of the feature definition and the likelihood model are therefore needed for improvement in performance.

## 5.5 Conclusion

A novel heart rate estimation algorithm that leverages sequential Bayesian tracking, HR harmonics, RR harmonics, and motion artifact removal has been proposed. The state-transition and likelihood models are data-driven, and the required density functions are learned through a training phase. A score feature that takes into account the respiration

harmonics interference onto the heart signal is proposed. The score feature, which defines the observation, is specifically designed to avoid mistakenly selecting a RR harmonic as the HR estimate, yet still be able to recognize a HR at or near a RR harmonic by incorporating the powers of the HR higher harmonics. Cross-validation is used to evaluate the performance of our algorithm on unseen data, i.e., in the production stage. Experimental results with 26 subjects show that the presented algorithm successfully integrates the Bayesian framework into the HR estimation problem from highly-interfered, low SNR non-contact vital signs signal obtained from the IR-UWB radar. We foresee that improvement is obtainable in several ways including finding better features, improving the likelihood model, and joint tracking of HR and RR.

# CHAPTER 6
# DETECTION OF MOTION AND POSTURE CHANGE

## 6.1 Introduction

Patients with limitted mobility, such as bed-ridden patients, are at risk of developing bed-sores or skin ulcers, the condition that can develop when a part of the skin is pressed against a surface for an extended period of time, causing prolonged poor blood circulation. This is most commonly due to lack of periodic change in posture. One preventative solution is to have body motion level and posture changes monitored, and notify the patient or caregivers when too little movement or no posture change has occured for a long time so that appropriate intervention is timely conducted. For example, such system can alarm the caregiver if a bed-ridden patient has not turned for the last several hours, and the caregiver can come in and help turn the patient. Therefore, an automatic, continuous motion quantifier and a posture change indicator are of clinical significance in prevention of skin ulcers.

The IR-UWB received signal carries information related to movements ranging from the micro movements of the heart and lungs to the large-scale (macro) body movements such as those incurred by a turn or moving limbs. Movements due to heart and lung motion induce quasi-periodic components in the radar received signal. On the other hand, macro body movements cause very large received signal amplitude.

Motion detection with UWB radar has several other uses. In a rescue application, victims trapped in ruins may still be able to move and their body movements should be much easier to detect than their vital signs by the IR-UWB radar. In a security and military application, an invisible and sensitive motion detector such as a UWB-based detector can protect an area from unauthorized access by detecting motion in the radar sensing coverage [85].

In this chapter, the effects of typical activities of a lying-in-bed patient on the radar

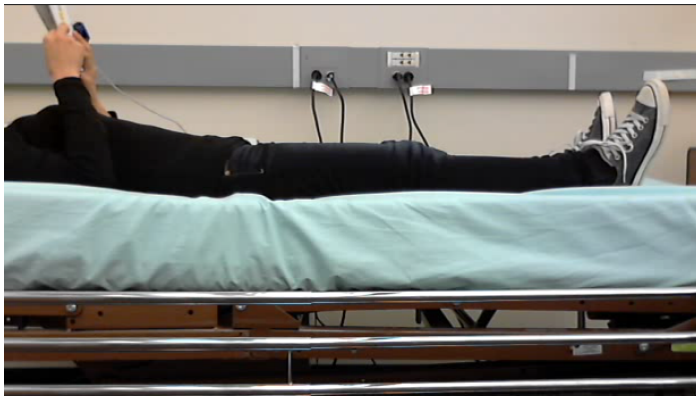

Figure 6.1: Subject was reading a book, occasionally turning pages. The radar was placed under the mattress.

received signal of a IR-UWB vital signs monitor is investigated, and a novel, simple algorithm that detects and quantifies motion events and also indicates if a macro-movement event has resulted in a posture change is presented. The algorithm is applied to the digital signal received from an IR-UWB radar HR and RR monitor. Thus, additional clinical parameters are extracted with only a modification in software and no hardware change is needed. The findings suggest that IR-UWB radar can be used for extracting posture related information in non-clinical enviroments for patients who are bed-ridden. The presented work serves as a first step for the development of more sophisticated methods to classify different types of movements, using IR-UWB radar, such as to identify if a period of movement corresponds to limb movement or a turn. The proposed methods can also be added to heart and respiration rate algorithms to improve the accuracy of the estimated parameters.

## 6.2 Methods

### 6.2.1 Protocol

The data for the study were collected from six adult subjects including 3 males and 3 females (demographics: age $40.2 \pm 13.6$ years, BMI $23.1 \pm 3.5$), under a protocol approved by Georgia Institute of Technology Institutional Review Board. Each subject lay still on his or her back for the first 10-12 minutes and performed a series of various daily activities

Table 6.1: Activities

| | |
|---|---|
| 1. Resting | 7. Turn onto left side |
| 2. Pick up book* | 8. Resting |
| 3. Turn pages | 9. Turn onto right side |
| 4. Put down book* | 10. Resting |
| 5. Count | 11. Turn onto stomach |
| 6. Arm movement & talk | 12. Resting |
| * Some arm movement and talk follow | |

including picking up and reading a book, talking, moving arms, turning to the sides and stomach. Specifically, the talking was counting from 1 to 20 and the arms moved round and round perpendicular with the chest. Table 6.1 lists the activities performed by each subject. Note that the footnote "* Some arm movement and talk follow" was not part of the protocol but was accidentally added by one subject. Hardware and analog signal processing are described in the previous chapters.

### 6.2.2 Motion and posture change detection

The complete motion and posture change detection algorithm is composed of two parts: (1) detecting and quantifying motion events, and (2) detecting if a posture change has taken place following a motion event. These are explained in detail below.

*Detection and quantification of motion events*

The radar-based motion detector works on the ADC samples from each of the heart and respiration bands. To detect motion in the heart band, for each ADC sample, we set an indicator function to 1 if the sample amplitude is outside the range $[L_h, U_h]$, and zero otherwise, where $L_h$ and $U_h$ are operator-specified lower and upper bounds in the heart signal channel, respectively. We sum the indicator function values over the temporal window of length $T$ (this counts the number of times the ADC value goes out of range) and divide that sum by the total number of samples in that window. If that ratio, denoted as $\rho$, is higher

than a threshold $\rho_{\text{th}}$, then we set a heart channel motion flag to one. A similar operation is done for the respiration band, but we change the bounds to $[L_r, U_r]$, where $L_r$ and $U_r$ are the lower and upper bounds in the respiration signal channel, respectively, and $L_r \leq L_h$ and $U_r \geq U_h$ since the respiration signal is stronger. The radar-based motion detector performs the OR operation on the heart-samples-based motion flag and the respiration-samples-based motion flag to compute the overall motion flag for the current temporal window. Then the window slides forward by $\Delta \leq T$ and the whole procedure is repeated to get the next overall motion flag. The values of all the above mentioned parameters, used in this work, are shown in Table 6.2.

In order to quantify motion, the out-of-range rates of the two channels are mapped to a score in a predefined scoring scale. Assume a motion scoring scale from 0 to $S$, where a score of 0 indicates no motion and a score of $S$ indicates that motion occurs during most or all of the duration of the window. One way to compute the motion score in a time window is through quantization:

$$\text{score}(\bar{\rho}) = \lceil \bar{\rho} S \rceil, \tag{6.1}$$

where $\bar{\rho}$ is the average of the out-of-range ratios from both heart and respiration channels in a window.

*Detection of postural change*

In order to quantify the changes in posture, the signal segments before and after a motion event are analyzed. If there is no motion event in $T_w$ second period ($T_w = 60s$), then local maxima and minima in this period are identified. The upper and lower envelopes, $E_u$ and $E_l$, are then determined by cubic inteprolation of the maxima and minima, respectively. The envelope difference sequence, $E_d$, is then estimated by subtracting the lower envelope from the upper envelope, i.e., $E_d = E_u - E_l$ [86]. The mean envelope difference, $\overline{E_d}$, is obtained by averaging $E_d$ over the number of samples in $T_w$ segment. $\overline{E_d}$ is then chosen as a reference and denoted by $\alpha_r$. Whenever a motion event is detected, the algorithm checks

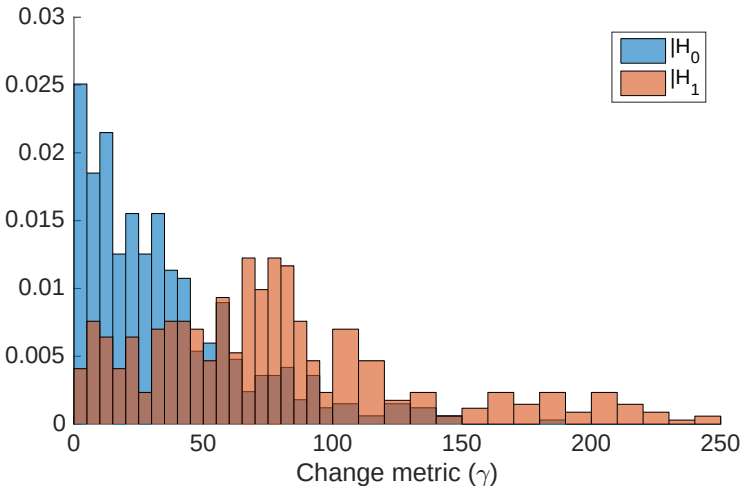


Figure 6.2: Histograms of the change metric $\gamma$ conditioned on the null hypothesis $H_0$ (i.e. no posture change) and the alternative hypothesis $H_1$ (i.e. there is a change in posture). The change metric $\gamma$ is the difference in $\overline{E_d}$ for pairs of $T_w$ segments from the data.

if there is no motion event in $T_w$ seconds of data that follows the motion event. Once such a segment is found, $\overline{E_d}$ is calculated for this new segment and compared with the reference $\alpha_r$. If the difference between estimated and reference value is greater than a threshold $\gamma_{th}$, then posture flag is set to one, indicating that a posture change has occured. The new value of $\overline{E_d}$ now becomes the new reference $\alpha_r$. The value of $\gamma_{th}$ is determined from the data by plotting two histograms shown in Fig. 6.2. Specifically, one histogram ($H_0$) is plotted for difference $\gamma$ in $\overline{E_d}$ values for two non-overlapping $T_w$ segments during periods without motion of the same posture. The second histogram ($H_1$) is for the difference $\gamma$ in $\overline{E_d}$ values of pairs of $T_w$ segments without motion, one belongs to one posture and the other belongs to the next posture. A threshold $\gamma_{th}$ can be defined as a point of intersection of the two histograms. By inspection, a value around 45 is appropriate for $\gamma_{th}$. For our data, $\gamma_{th} = 43$ works best in terms of maximizing the detection rate and minimizing the false alarm rate.

## 6.3 Results

### 6.3.1 Motion detection and quantification

Fig. 6.3a-b show the output of the respiration and heart bands of the system, respectively. The resting periods (Activities 1, 8, and 10) are clearly indicated by the regular change in the signal amplitude in both channels. In contrast, strong activities (Activities 2, 4, 7,9,11) cause large peak-to-peak amplitude fluctuation including saturated ADC samples (the "clips" in Fig. 6.3a-b), usually in both signal channels. Talking (Activity 5) however appears to have little effect on the radar received signal. The individual motion detector output for the heart channel and the respiration channel are indicated also on these plots (the dots at the top and bottom of each plot). In these plots, the motion flags are multiplied by 4250 for ease of viewing. The vertical bars between Fig. 6.3a and Fig. 6.3b delimit periods corresponding to different activities as listed and numbered in Table 6.1. The overal motion flag is plotted in Fig. 6.3c. For example, at $t = 664$ seconds the heart channel flag is set to 1 and the respiration channel motion flag is set to 0, hence the overall motion flag is 1, and we say motion is detected in the time window $[t - T, t]$ or [660 seconds - 664 seconds]. It is worth noting that a heuristic selection of the out-of-range threshold $\rho_{\text{th}}$ has been made. Let $F_s$ be the ADC sampling rate, here $F_s = 128$ Hz, then $\rho_{\text{th}} = 0.15$ means that a window must contain at least $\rho_{\text{th}} T F_s = 0.6 * F_s$ or $0.6$ seconds of out-of-range ADC samples to set the motion flag to 1. A typical body movement typically lasts longer than 0.6 seconds. This motion detector can be made more or less sensitive by varying the heart bounds and respiration bounds or by changing the out-of-range threshold. The radar-based motion flags are observed to agree well with the subject's time-stamped series of movements.

The motion score is shown in Fig. 6.3d. In order to quantify different types of motion events, we considered two movement events, "Pick up a book" and "Put down the book", and another two movement events that result in a posture change. The other activities are located very close to each other in time and hence are not included in the analysis.

Table 6.2: Motion detection parameters and values

| Parameter | Value |
|---|---|
| Window length (T) | 4 s |
| Window step ($\Delta$) | 2 s |
| $[L_h, U_h]$ | $[1000, 3000]$ |
| $[L_r, U_r]$ | $[500, 3500]$ |
| $\rho_{\text{th}}$ | $0.15$ |

The motion score values were averaged over the duration of the activities. The mean and standard deviation for all subjects for the above mentioned activities is shown in Fig. 6.4. It can be observed that motion events that correspond to a posture change have high motion score.

### 6.3.2 Detection of posture change from the radar signal

The results for detection of posture change in one subject are shown in Fig. 6.3e-f. Since the radar records data in both the respiration and heart band, posture change flag was calculated with heart channel alone in Fig. 6.3e. The algorithm accurately detects the three posture changes for this subject. Fig. 6.3f shows value for posture flag if information from respiration channel is also combined with the heart channel. Specifically, the posture change flag was calculated from both channels and an OR operation was performed between them. All the posture changes are also correctly detected.

The results for posture change for all subjects are summarized in Table 6.3. A ✓ indicates a correct detection while $\times$ represents a missed detection. The number of false alarms is included in the last column. The red symbols or numbers correspond to when using the heart channel data only. The black symbols or numbers correspond to when using both heart and respiration channels. When using the heart channel data only, the algorithm was able to detect correct posture change 77.8% of the time for all subjects, with a false alarm rate of 20%. When both channels are used in posture detection, the detection rate is increased to 88.9% but the false alarm rate is also increased to 26.7%.

Table 6.3: Posture detection results

| Subject No. | B→ L | L → R | R → S | FA |
|---|---|---|---|---|
| 1 | ✓ ✓ | ✓ ✓ | ✓ ✓ | 4, 5 |
| 2 | ✓ ✓ | × × | × ✓ | 0, 1 |
| 3 | × ✓ | ✓ ✓ | ✓ ✓ | 1, 1 |
| 4 | ✓ ✓ | ✓ ✓ | ✓ ✓ | 0, 0 |
| 5 | ✓ ✓ | × × | ✓ ✓ | 1, 1 |
| 6 | ✓ ✓ | ✓ ✓ | ✓ ✓ | 0, 0 |
| B: Back, L: Left, R: Right, S: Stomach, FA: False alarm | | | | |

## 6.4 Discussion

The results derived indicate that IR-UWB can be used to detect motion and postural changes. The motion detection algorithm operates on small time windows ($T = 4s$) and the time sensivity of the detector can be changed by changing the window size. On the other hand, the posture change is estimated from a window ($T_w$) of 60-seconds duration. The larger window size was chosen to decrease false alarm rate. Moreover, patients with limited mobility, such as those in nursing homes, who require posture change after periodic intervals, normally stay in a particular posture for a longer time.

As indicated by the results, both channels can accurately detect motion. Combining posture change information from both signals improves the detection probability but degrades the false alarm rate.

A limitation of this work is the extremely small sample size of 6 subjects. Future work should include data from patients of all ages and also from sick and bed-ridden patients in nursing homes. The algorithm presented can be augmented with other parameters related to heart and respiration rate to provide for more accurate detection of micro- and macro-movements. As indicated in Fig. 6.4, movements due to a posture change are associated with high motion score. Thus, future work should also focus on incorporation of motion score, as well as features other than those based on amplitude of the signal.

## 6.5 Conclusion

This chapter presents a method for motion detection and quantification, and postural change detection with IR-UWB radar. Motion detection is applied on both heart and respiration signal channels, followed by fusion of the outcomes to provide a more reliable result. The algorithm assigns a score value to each motion event and also utilizes signal statistics to determine if a motion event has caused a posture change. The accuracy of posture change determined by the algorithm is 88.9%.

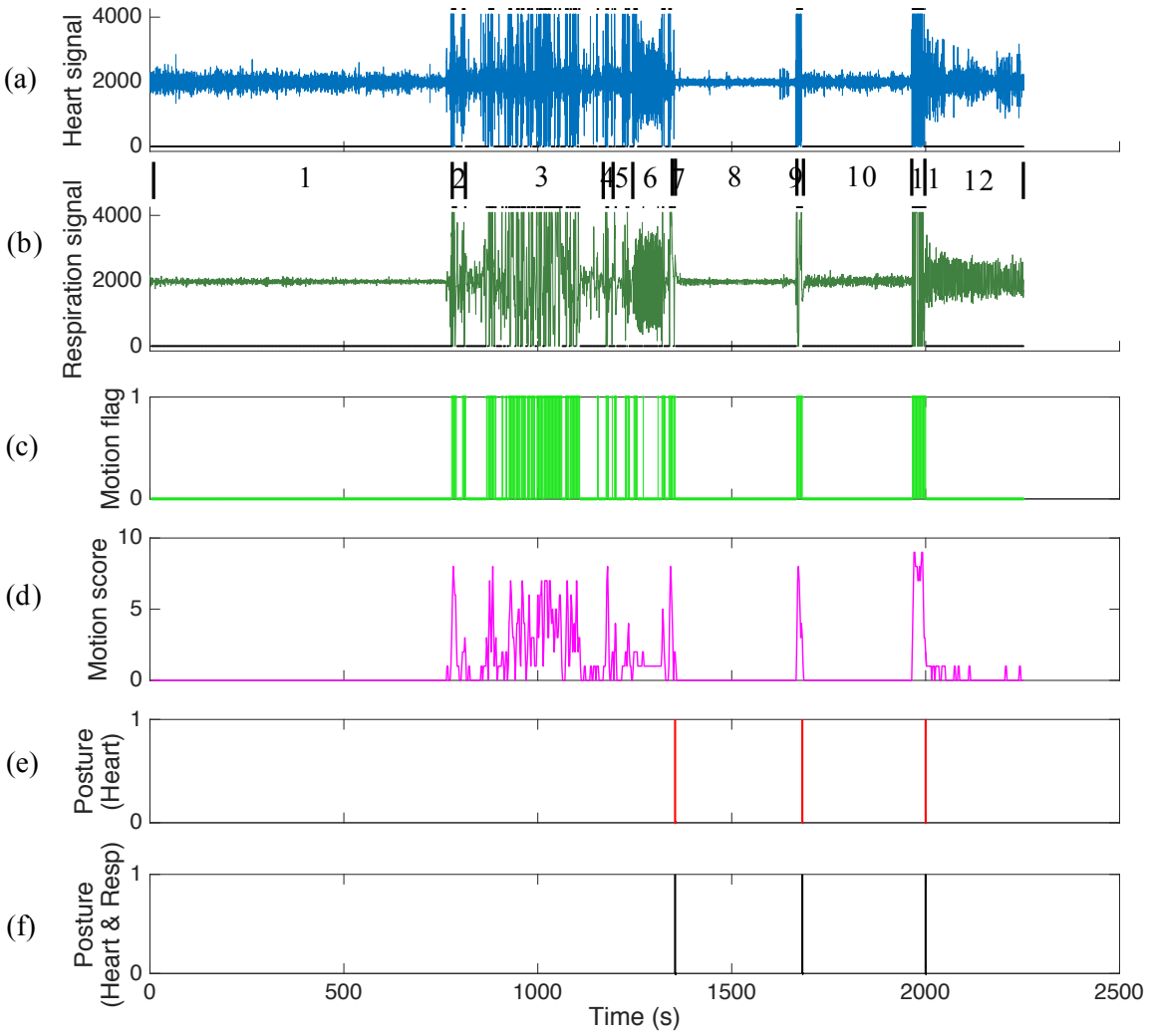


Figure 6.3: Data of one subject. (a) Heart signal. (b) Respiration signal. (c) Motion flag. (d) Motion score with $S = 10$. (e) Posture-change flag from heart channel only. (f) Posture-change flag from both heart and respiration channels. The "clips" occur at 0 and 4095, the quantization limits of a 12-bit ADC.

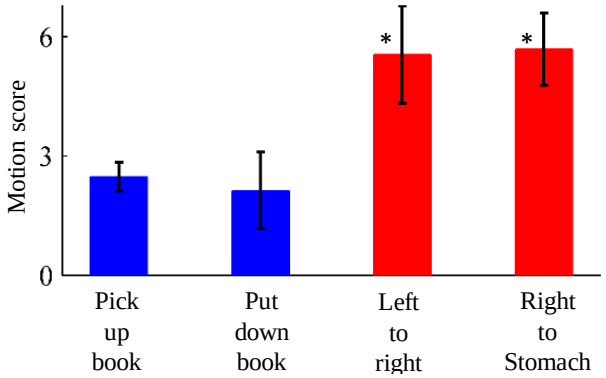


Figure 6.4: Motion scores for all subjects. The blue bars represent motions not resulting into a posture change while the red bars are for those that cause a change in posture. (*) indicates that $p < 0.05$ for the posture changing motion scores as compared to those that were caused by low intensity movements.

# CHAPTER 7
# MAXIMUM LIKELIHOOD ESTIMATION OF CHEST WALL DISPLACEMENT FROM A TINY FRACTION OF THE IR-UWB RECEIVED SPECTRUM

We present a novel method of extracting the chest wall displacement *in the frequency domain* from only a tiny fraction of the IR-UWB radar received spectrum. A maximum likelihood (ML) estimator of the displacement is designed, and the associated bias and Cramér Rao lower bound of the ML estimator are derived. To improve estimation accuracy, empirical mode decomposition is applied to denoise the ML estimated displacement. Simulation studies are conducted to evaluate the performance of the proposed methods under realistic system parameter values. The computational complexity of the proposed methods is low and equal to that of a discrete Fourier transform.

## 7.1 Introduction

Chest displacement is of clinical significance in identifying clinical disorders. Chest displacement recorded during sleep is a part of the polysomnogram (PSG), which is the gold standard diagnostic tool in sleep medicine. Chest displacement during sleep is valuable in diagnosis of sleep disorders such as sleep apnea [87, 88]. During unobstructed respiration, a linear relationship between tidal volume and chest wall displacement have been shown in a number of studies [89, 90, 91]. In addition, the complex intrathoracic motion of the heart also causes minute displacement of the chest wall, which if measurable could be useful in diagnosis of cardiac disorders.

Currently, respiratory monitoring is commonly performed by applying a nasal cannula or mask to the patients airway opening. Such obtrusive attachment tends to alter the patient's normal breathing patterns [90], thus prevents accurate breathing pattern monitoring. In order to avoid this problem, monitoring systems that can be applied on the chest wall sur-

face have been developed. The most common tool is a chest strap, or also called respiratory effort belt. As the authors in [90] point out, the chest strap does not provide absolute chest wall displacement directly, rather it measures the relative change in the ribcage circumference. While being low cost and simple, there are several concerns about this method. The sensitivity of the chest strap is strongly dependent on the tightness of its elastic band [92]. Lee [93] suggests that the validity of chest strap measurement, which is obtained by the interaction between the elastic chest strap and the chest wall, is questionable. Chest band measurement also has a clipping problem [87]. All these methods require attachments which can be restrictive, disrupt sleep, and cause discomfort or pain especially for long-term monitoring. Furthermore, burned patients or patients with skin ulcers cannot accept attachment, but will benefit from continuous monitoring.

These problems can be avoided with non-contact methods. Kondo and coworkers [90] propose a laser monitor that measures distance between the chest and the sensor; the chest displacement is obtained by plotting the change in such distance measurement. The proposed laser monitor must be placed within a few inches of the chest or abdomen surface, causing restriction in movement and not suitable for continuous monitoring. Recently, laser self-mixing interferometry has also been proposed as a means for sensing displacement of a generic target surface [94] and the chest wall in particular [95]. However, since laser sensors cannot sense through clothes, the patient needs to remove their upper body clothes, causing inconvenience and unsuitability for continuous monitoring.

Continuous wave (CW) Doppler radar can penetrate through clothes, and has been proposed for non-contact chest wall displacement sensing in a number of studies [96, 97, 98, 92]. These methods perform DC offset calibration to estimate the undesired DC offsets present in the two quadrature baseband signal channels, followed by arctangent demodulation [96] to obtain displacement information. Wavelet filtering and ensemble empirical mode decomposition [99] has also been added to improve estimation accuracy for the thorax cardiopulmonary displacement waveforms [98]. Good agreement with gold standard

method such as overnight PSG recordings for most cases has been demonstrated [92]. However, these methods face several challenges. Existing DC offset calibration methods have been shown to be strongly dependent on one or a combination of factors such as displacement amplitude, displacement morphology, and noise levels [100, 101, 92]. Examples include erroneous or arbitrary DC offsets estimation result for small breathing displacement amplitude or when the constellation diagram of the in-phase and quadrature baseband channels is not close enough to an arc shape [92]. In addition, phase imbalance and amplitude imbalance between the two channels can cause errors in the arctangent estimator of the displacement.

Although chest wall displacement is dominantly controlled by respiratory motion, it is also caused by heartbeating. Many methods have been proposed to reconstruct the heartbeat-induced displacement. Ramachandran [102] measures chest wall displacement through different phases of the cardiac cycle, in the absence of breathing, based on the capacitance variation between a fixed capacitive probe and the moving skin surface. Although the probe is not in contact with the skin, a probe holder is placed on skin, and distance between the probe and the thorax is adjusted to be less than 1mm. This causes complication in practical measurement such as in home healthcare. Truly non-contact sensing methods based on cardiokymography and laser have been proposed. The cardiokymograph, or displacement cardiograph (DCG), first proposed by Vas [103] measures the electromagnetic field interaction between a sensing coil and the moving chest surface. The transducer is located a few centimeters away from the chest, either hung from a stand or strapped to the body. However, this method is limited by low reproducibility, unstableness, and low rate of obtaining recordings of adequate quality for data analysis [104]. Laser speckle interferometry has been proposed to estimate heartbeat-induced chest wall displacement in the absence of breathing [105, 106, 107]. However, laser methods do not offer through-clothing sensing, as mentioned above.

Similar to Doppler radar, IR-UWB radar is a non-contact technique that has been

demonstrated as a promising tool for physiological sensing. While many studies exist for applying Doppler radar on chest wall displacement estimation, few exist for IR-UWB radar. For IR-UWB radar, some existing methods perform direct sampling of the backscattered RF waveforms, and then either detect the waveform peaks [11, 108] or compute the correlation with a reference waveform [13, 15] to obtain the absolute or relative pulse delays, which are associated with the chest displacement. However these methods require extremely high sampling rate (tens of GHz). Specialized radar system designs have been proposed [83, 82, 109, 14], where cross correlation is obtained by hardware, transforming the received RF pulses into a low-frequency equivalent which can be digitized at a much lower sampling rate.

Unlike these works, which are time domain approaches, an iterative time delay estimation algorithm based on the weighted Fourier transform has been proposed in [110]. The received signal consists of copies of a known signal with different amplitudes and delays. The delays are estimated from the received signal spectrum using an iterative algorithm. The number of steps is equal to the number of copies. Each step comprises of one or more one-dimensional search procedure which uses FFT followed by a fine search algorithm. The number of such search procedures grows quadratically with the number of copies, or equivalently, the number of time delays to be estimated. Possible convergence to local minima is also a problem. In addition, since this algorithm requires direct sampling of the backscattered signal, extremely high sampling rate is needed if applied to IR-UWB pulse delay estimation, as demonstrated in the work itself as well as mentioned earlier for [11, 108, 13, 15].

In this chapter, we propose a computationally efficient chest displacement estimator in the *frequency domain*. A striking feature that differs from the previously mentioned methods is that only a tiny fraction of the received UWB signal spectrum is needed to obtain the entire chest wall displacement waveform in an observation window. The estimator is based on the maximum likelihood principle, and the associated bias and Cramér Rao lower

bounds are provided. Theoretical limits for estimators developed with UWB radar signal have been either derived or formulated. Zhang [111] analyzes CRLBs for pulse delay estimation for UWB synchronization problem, but the pulses within an observation window are assumed to have the same roundtrip delay. This assumption is not valid for a moving reflecting interface, such as the chest surface. CRLBs of the parameters of a periodic chest displacement waveform are presented in [112]. An ML estimator that requires an exhaustive search over a multi-dimensional parameter space is formulated, and a sub-optimal solution based on matched filtering and least squares fitting are proposed. However, both the bounds and estimators are based on the assumption that the chest displaces according to some known parametric periodic analytical functional. In reality, the chest displacement can follow an irregular pattern such as during obstructed breathing, and is typically non-stationary even during normal breathing. In contrast, this chapter presents an ML estimator that directly estimates an arbitrary chest displacement waveform. The ML estimator complexity in [112] is prohibitive for practical applications due to the exhaustive search. In contrast, our ML estimator has conceptually and computationally simple closed-form expression.

In order to improve estimation accuracy, especially under low SNR, a denoising method is applied to the ML estimates. In this chapter, empirical mode decomposition (EMD) [99] is chosen as denoising technique, but other denoising techniques such as independent component analysis [113] can also be used.

Although chest displacement monitoring is the focused application of this chapter, the presented method could also be applied in monitoring of displacement of other targets, such as a bridge or civil structure. These structural health monitoring applications have been suggested for CW Doppler radar [100].

Since only a tiny fraction of the UWB bandwidth is needed, the proposed method offers significantly sampling rate reduction over the conventional digital correlation technique. Computational complexity of the ML estimator is on the order of a Discrete Fourier Trans-

form (DFT). Complexity with denoising is on the order of a DFT and the selected denoising method, whichever is larger. As shown in [114], the complexity of EMD is the same with that of an FFT, thus the denoised ML estimator (ML estimator followed by denoising) has a complexity of an FFT [1]. Thus, the proposed method is practical for real time systems.

## 7.2 Methods

The noiseless IR-UWB radar received signal can be expressed as

$$s(t) = \sum_{n=0}^{N-1} p_0 \left( t - nT_r - \frac{2D_0}{c} - \Delta_n \right), \tag{7.1}$$

where $N$ is the number of pulses received, $p_0(t)$ is the transmitted UWB pulse shape, $D_0$ is the nominal distance between the radar and the chest, $c = 3 \times 10^8$ m/s is the pulse propagation speed, $\Delta_n$ is the additional delay that the moving chest wall imposes on the $n^{th}$ pulse.

Let $p(t) = p_0\left(t - \frac{2D_0}{c}\right)$. Then Eq. (7.1) becomes

$$s(t) = \sum_{n=0}^{N-1} p(t - nT_r - \Delta_n), \tag{7.2}$$

The CTFT of this is

$$\begin{aligned} S(f) &= P(f) \sum_{n=0}^{N-1} e^{-j2\pi f(nT_r + \Delta_n)} \\ &= P(f) \sum_{n=0}^{N-1} e^{-j2\pi f \Delta_n} e^{-j2\pi f n T_r} \end{aligned}$$

[1] A procedure that performs several sequential tasks, each of which has complexity of $\mathcal{O}(N)$, also has complexity of $\mathcal{O}(N)$

Let $f = Mf_r + kf_r/N$, for $k \in [0, N-1]$. After some manipulation, we obtain

$$S\left(Mf_r + \frac{kf_r}{N}\right) = P\left(Mf_r + \frac{kf_r}{N}\right) \sum_{n=0}^{N-1} e^{-j2\pi(Mf_r + \frac{kf_r}{N})\Delta_n} e^{-j\frac{2\pi kn}{N}}. \tag{7.3}$$

For $f = Mf_r + kf_r/N$ in the GHz range, and since $f_r$ is typically on the order of kHz in practical IR-UWR radar systems, $\frac{kf_r}{N} < f_r \ll Mf_r$. Consequently, the $\frac{kf_r}{N}$ term in the first exponential term of Eq. (7.3) can be dropped. Denote $P[k] = P(Mf_r + \frac{kf_r}{N})$ and $x[n] = e^{-j2\pi Mf_r\Delta_n}$. A plot of the pulse spectrum samples $P[k]$'s is depicted in Fig. 7.1, showing $P[k]$ is nearly a constant as a function of $k$.

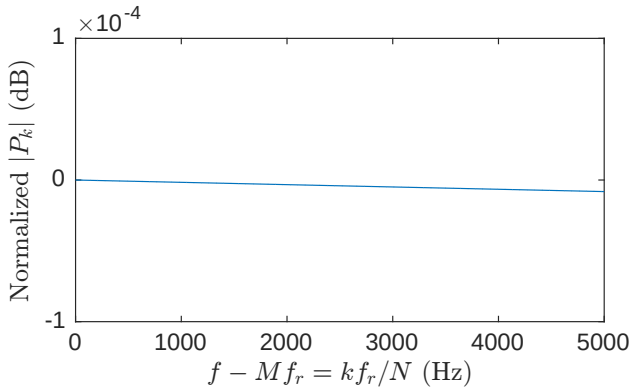


Figure 7.1: Samples $P[k]$'s of a pulse spectrum

Equation (7.3) becomes

$$S\left(Mf_r + \frac{kf_r}{N}\right) \approx P[k] \sum_{n=0}^{N-1} x[n] e^{-j\frac{2\pi kn}{N}} = P[k]X[k], \tag{7.4}$$

where $X[k]$ is the $N$-point DFT of the discrete time sequence $x[n], n = 0, \ldots, N-1$.

Let $z_k$ be the received signal spectrum at the frequency $f = Mf_r + \frac{kf_r}{N}$, for $k = 0, 1, \ldots, N-1$. Then,

$$z_k = P[k]X[k] + v_k, \tag{7.5}$$

where $\{v_k\}$ is an additive noise modeled as i.i.d. zero mean complex Gaussian random variables with variance $N_0$.

In order to simplify notation, we drop all the discrete time indexing in square brackets to become subscript. Then Eq. (7.5) is rewritten as

$$z_k = P_k X_k + v_k. \tag{7.6}$$

Denote

$$Y_k = z_k/P_k = X_k + v_k/P_k. \tag{7.7}$$

An example plot of $Y_k$'s is shown in Fig. 7.2. Fig. 7.2a depicts the entire frequency range of $kf_r/N$ for $k = 0, 1, \ldots, N-1$. Here $f_r = 5$ kHz, $Mf_r \approx 5.32$ GHz, so the range of frequency is the narrowband from 5.32 to 5.325 GHz, SNR = 6 dB. It is observed that the majority of the spectrum energy concentrates near the range edges. The spectrum corresponding to the first and last 25 Hz of the range is replotted in Fig. 7.2b and 7.2c, respectively.

Taking the IDFT of $Y_k$ (Eq. (7.7)) yields

$$\begin{aligned} y_n &= IDFT_N(Y_k) \\ &= x_n + w_n \end{aligned} \tag{7.8}$$

where $w_n = IDFT(v_k/P_k) \sim \mathcal{CN}(0, \sigma_w^2)$, with $\sigma_w^2 = N_0/(N|P_0|^2)$, since $\{v_k/P_k\}$ is a zero mean, white complex Gaussian random process with variance $N_0/|P_k|^2 \approx N_0/|P_0|^2$.

Denote

$$\theta_n = -2\pi M f_r \Delta_n \tag{7.9}$$

Then (7.8) becomes

$$y_n = e^{j\theta_n} + w_n \tag{7.10}$$

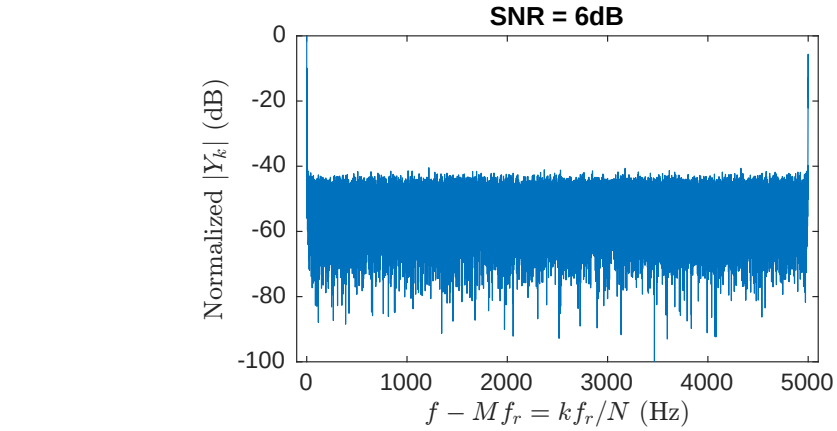


(a)

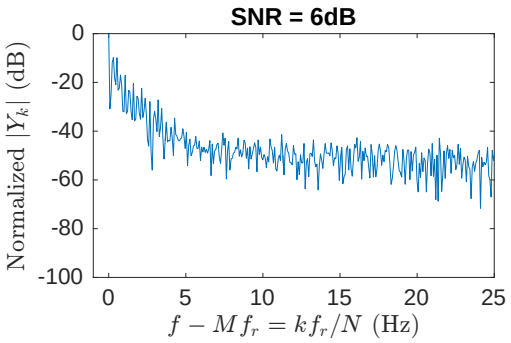


(b)

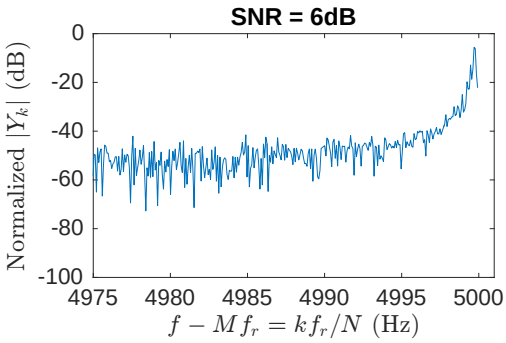


(c)

Figure 7.2: (a) Plots of $Y_k$'s over the entire frequency band of $f_r$ Hz starting from $Mf_r \approx 5.32$ GHz, and the close-up version of the (b) first and (c) last 25 Hz of the frequency band.

The following vector notation will be used:

$$\boldsymbol{\theta} = [\theta_0, \theta_1, \ldots, \theta_{N-1}]^T$$

$$\mathbf{y} = [y_0, y_1, \ldots, y_{N-1}]^T$$

$$\mathbf{w} = [w_0, w_1, \ldots, w_{N-1}]^T$$

Based on (7.10),

$$\mathbf{y} = \exp(j\boldsymbol{\theta}) + \mathbf{w}.$$

where $\mathbf{w} \sim \mathcal{CN}(0, \sigma_w^2 \mathbf{I})$.

The likelihood of $\theta$ corresponding to the measurement vector $\mathbf{y}$ is

$$\begin{aligned} p(\mathbf{y}|\theta) &= \frac{1}{(\pi\sigma_w^2)^N} \exp\left\{-\frac{1}{\sigma_w^2} ||\mathbf{y} - \exp(j\boldsymbol{\theta})||_2^2\right\} \\ &= \frac{1}{(\pi\sigma_w^2)^N} \exp\left\{-\frac{1}{\sigma_w^2} \sum_{n=0}^{N-1} \left|y_n - e^{j\theta_n}\right|^2\right\} \end{aligned}$$

The log likelihood is

$$\ln p(\mathbf{y}|\theta) = -N \ln(\pi\sigma_w^2) - \frac{1}{\sigma_w^2} \sum_{n=0}^{N-1} \left|y_n - e^{j\theta_n}\right|^2$$

After rather tedious manipulation, the partial derivatives of the log likelihood are derived as

$$\frac{\partial}{\partial\theta_m} \ln p(\mathbf{y}|\theta) = \frac{2}{\sigma_w^2} r_m \sin(\phi_m - \theta_m),$$

where $y_m = r_m e^{j\phi_m}, m = 0, 1, \ldots, N-1$.

Therefore, the ML estimate of the phase vector $\theta$ is

$$\hat{\boldsymbol{\theta}} = \boldsymbol{\phi}$$

where $\boldsymbol{\phi} = [\phi_0, \phi_1, \ldots, \phi_{N-1}]^T$

Let $\boldsymbol{\Delta} = [\Delta_0, \Delta_1, \ldots, \Delta_{N-1}]^T$ be the pulse delay vector. Its ML estimate is

$$\hat{\boldsymbol{\Delta}} = -\frac{1}{2\pi M f_r} \boldsymbol{\phi}$$

Let $d_n = c\Delta_n/2$ be the chest displacement corresponding to the $n^{th}$ pulse, and $\mathbf{d} = [d_0, d_1, \ldots, d_{N-1}]^T$. The displacement estimate is

$$\hat{\mathbf{d}} = -\frac{c}{4\pi M f_r} \boldsymbol{\phi}$$

Although the sequence of ML displacement estimates follows the waveform of the chest displacement, as will be shown in Section 7.4, it is noisy. In order to reduce noise from the estimates, a denoising method is applied. Examples of denoising methods include empirical mode decomposition (EMD) [115] and independent component analysis (ICA) [113]. In this dissertation, EMD is selected as the denoising method. The ML estimator followed by denoising will be referred to as the denoised ML estimator, or DML estimator.

## 7.3 Cramér-Rao lower bound of the maximum-likelihood chest displacement estimator

### 7.3.1 Fisher information matrix

The $mn^{th}$ element of the Fisher information matrix is $F_{mn} = E\left[-\frac{\partial^2 \ln p(\mathbf{y}|\boldsymbol{\theta})}{\partial\theta_m \partial\theta_n}\right]$ and can be derived or found directly in [116]

$$F_{ml} = \frac{2}{\sigma_w^2}\sum_{n=0}^{N-1}\frac{\partial\mu_n}{\partial\theta_m}\frac{\partial\mu_n}{\partial\theta_l} + \frac{\partial\nu_n}{\partial\theta_m}\frac{\partial\nu_n}{\partial\theta_l}$$

where $\mu_n = \cos(\theta_n)$ and $\nu_n = \sin(\theta_n)$. It can be easily shown that

$$\mathbf{F} = \frac{2}{\sigma_w^2}\mathbf{I}. \tag{7.11}$$

### 7.3.2 Bias

$$E[\hat{\boldsymbol{\theta}}] = E[\boldsymbol{\phi}] = [E[\phi_0], E[\phi_1], \ldots, E[\phi_{N-1}]]^T \tag{7.12}$$

$$E[\hat{\theta}_n] = \int_{-\pi}^{\pi}\phi_n p(\phi_n|\theta)d\phi_n = \int_{-\pi}^{\pi}\phi_n p(\phi_n|\theta_n)d\phi_n \tag{7.13}$$

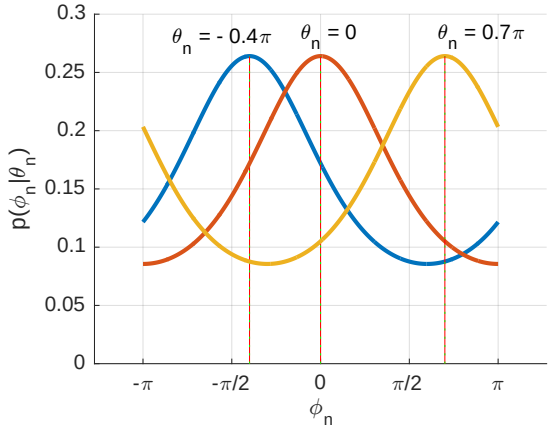


Figure 7.3: Plots of $p(\phi_n|\theta_n)$ for various values of $\theta_n$ and $\sigma_w^2 = 10$.

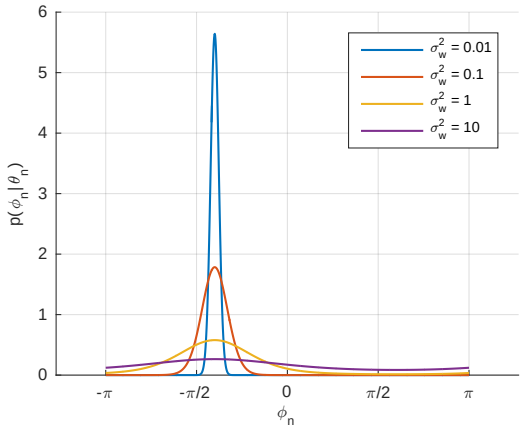


Figure 7.4: Plots of $p(\phi_n|\theta_n)$ for $\theta_n = -0.4\pi$ and various values of $\sigma_w^2$.

where the conditional density is obtained based on the general result in[117]

$$p(\phi_n|\theta_n) = \frac{1}{2\pi} e^{-\frac{1}{\sigma_w^2}} \left[1 - \sqrt{\pi}\alpha_n e^{\alpha_n^2} \text{erfc}(\alpha_n)\right],$$

where $\alpha_n = -\sqrt{\frac{1}{\sigma_w^2}} \cos(\phi_n - \theta_n)$ and erfc(.) is the complementary error function defined as $\text{erfc}(u) = \frac{2}{\sqrt{\pi}} \int_u^\infty e^{-t^2} dt$. Fig. 7.3 plots $p(\phi_n|\theta_n)$ for various values of $\theta_n$ for $\sigma_w^2 = 10$. Fig. 7.4 plots $p(\phi_n|\theta_n)$ for $\theta_n = -0.4\pi$ and various values of $\sigma_w^2$.

The bias of the estimator $\hat{\theta}_n$ is defined as

$$b(\theta_n) = E(\hat{\theta}_n) - \theta_n$$

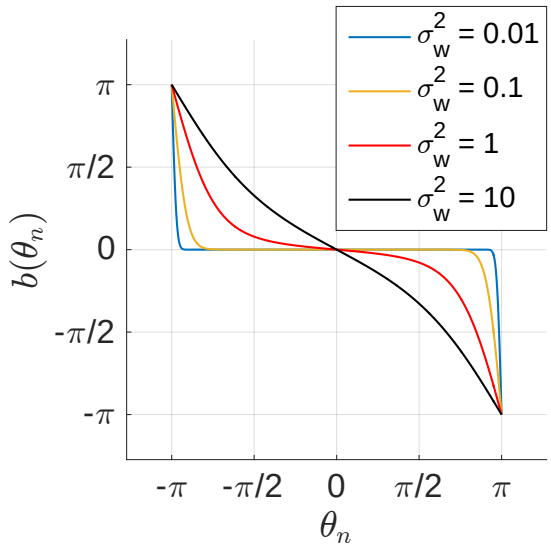


Figure 7.5: Bias of $\hat{\theta}_n$.

and is depicted in Fig. 7.5. It is observed that $\hat{\theta}$ is a biased estimator. The bias approaches zero when $\sigma_w^2 \to 0$ and approaches the line $b(\theta_n) = -\theta_n$ as $\sigma_w^2 \to \infty$.

The vector of the bias of all parameters in $\theta$ is defined as

$$\mathbf{b}(\boldsymbol{\theta}) = [b(\theta_0), b(\theta_1), \ldots, b(\theta_{N-1})]^T$$

### 7.3.3 Cramér-Rao lower bound

Let $\boldsymbol{\epsilon} = \hat{\boldsymbol{\theta}} - \boldsymbol{\theta}$. Since $\hat{\boldsymbol{\theta}}$ is a biased estimator, the CRLB on the mean squared error matrix is expressed as [118]

$$E[\boldsymbol{\epsilon}\boldsymbol{\epsilon}^T] \geq \mathbf{b}(\boldsymbol{\theta})\mathbf{b}^T(\boldsymbol{\theta}) + (\mathbf{I} + \nabla_{\boldsymbol{\theta}}\mathbf{b})\mathbf{F}^{-1}(\mathbf{I} + \nabla_{\boldsymbol{\theta}}\mathbf{b})^T \tag{7.14}$$

where $\nabla_\theta \mathbf{b}$ is the gradient matrix with elements of the form

$$[\nabla_\theta \mathbf{b}]_{mn} = \frac{\partial b_m}{\partial \theta_n}$$

A matrix is lower-bounded by a second matrix if the difference between the two is a positive semidefinite matrix.

It follows that the mean squared errors of $\hat{\theta}_n$'s are bounded by the diagonal elements of the right-hand-side of (7.14)

$$E[(\hat{\theta}_n - \theta_n)^2] \geq b^2(\theta_n) + [(\mathbf{I} + \nabla_{\boldsymbol{\theta}}\mathbf{b})\mathbf{F}^{-1}(\mathbf{I} + \nabla_{\boldsymbol{\theta}}\mathbf{b})^T]_{nn}$$

Fig. 7.6 shows the CRLB of the mean squared error of $\hat{\theta}_n$.

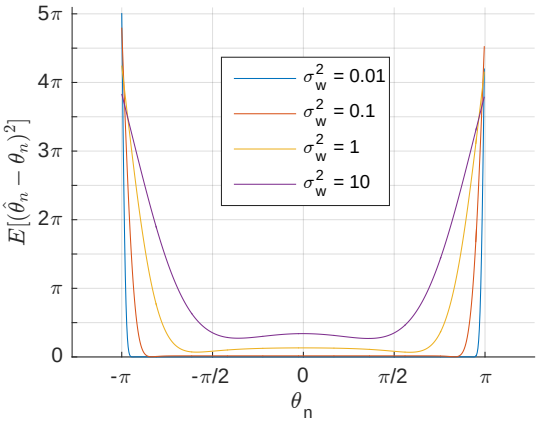


Figure 7.6: CRLB of the mean squared estimation error of $\theta_n$. Note that the presented CRLB is associated with the ML estimator $\hat{\theta}_n$. Only in the case of unbiased estimators is the CRLB independent of the estimator used [118].

Then the MSE of the chest displacement estimator is related to that of the phase estimator by

$$E[(\hat{\mathbf{d}} - \mathbf{d})(\hat{\mathbf{d}} - \mathbf{d})^T] = \left(\frac{c}{4\pi M f_r}\right)^2 E[\boldsymbol{\epsilon}\boldsymbol{\epsilon}^T], \tag{7.15}$$

where $c$ is the propagation speed of a pulse.

It follows that the CRLB of MSE of the $d_n$ estimate is

$$E[(\hat{d}_n - d_n)^2] \geq \left(\frac{c}{4\pi M f_r}\right)^2 \left\{b^2(\theta_n) + [(\mathbf{I} + \nabla_{\boldsymbol{\theta}}\mathbf{b})\mathbf{F}^{-1}(\mathbf{I} + \nabla_{\boldsymbol{\theta}}\mathbf{b})^T]_{nn}\right\}. \tag{7.16}$$

The CRLB is a function of the parameters to be estimated. Estimate of each displace-

ment sample has a lower bound as shown in Eq. 7.16. The mean squared error defined for the entire sequence of $N$ displacement samples is expressed as

$$E\left[\frac{1}{N}\sum_{n=0}^{N-1}(\hat{d}_n - d_n)^2\right] \geq \frac{1}{N}\sum_{n=0}^{N-1} B_n \tag{7.17}$$

where $B_n$ is the right hand side of Eq. (7.16), i.e., the CRLB of the estimate of $d_n$.

The sequence MSE is lower-bounded by the average of the individual CRLBs. The RMSE and its CRLB is defined by taking the square root of the left hand side and right hand side of Eq. (7.17), respectively.

### 7.3.4 Selection of $M$

As seen in Eq. (7.16), the CRLB of the displacement pattern is inversely proportional to the square of $Mf_r$, so $Mf_r$ should be large. However, it is also proportional to the CRLB of $\theta_n$. Based on Fig. 7.6, the CRLB of $\theta_n$ is low for small $|\theta_n|$, most notably for $|\theta_n| \leq \pi/2$. Based on (7.9), $Mf_r$ should therefore be upper-bounded. In addition, $|P(Mf_r)|$ should be large since it is desired that $\sigma_w^2$, which controls how much $\phi_n$ deviates from $\theta_n$, is small.

In summary, the cluster index $M$ is selected to have the following properties

1. $Mf_r$ is large
2. $Mf_r \leq \gamma c/(4D)$, where $0 < \gamma < 1$ and $D$ is the maximum human chest displacement magnitude. It can be easily shown that $|\theta_n| \leq \frac{4\pi M f_r D}{c}$. When $Mf_r \leq \gamma c/(4D)$, $|\theta_n| \leq \gamma\pi$.
3. $|P(Mf_r)|$ is large.

Based on these criteria, the integer $M$ is selected as

$$M = argmax_{M \leq \gamma c/(4f_r D)} Mf_r |P(Mf_r)| \tag{7.18}$$

where in this thesis, we choose $\gamma = 1/2$ and $D = 7$mm.

Table 7.1: Parameter values

| Description | Parameter | Value |
|---|---|---|
| Maximum magnitude | $m_b$ | 5 mm |
| Breathing period | $T_b$ | 3.75 s |
| IER | IER | 0.5 |
| Initial phase | $t_0$ | $\mathcal{U}[0, T_b]$ |
| Pulse repetition frequency | $f_r$ | 5 kHz |
| Number of received pulses | $N$ | 65,536 |
| Pulse shape | - | $7^{\text{th}}$-order monocycle with bandwidth scaling factor 0.3 ns [68] |
| Nominal distance | $D_0$ | 0.5 m |

## 7.4 Simulation results

Simulation is conducted to evaluate the estimation performance of the proposed method and compare with the CRLB. Without loss of generality, the chest displacement is assumed to be solely due to breathing. Simulated breathing parameters are chosen taking into account that in normal breathing, the IER is less than 1 and the arbitrary initial phase of the breathing displacement can be at any phase during one breathing cycle. The simulation parameters and values used are reported in Table 7.1. Among these parameters, $N = 65,536$ corresponds to an observation window length of $N/f_r = 13$ s, or about 3.5 breathing cycles. $M$ is selected according to Eq. (7.18), resulting in $Mf_r \approx 5.3$ GHz.

Fig. 7.7 shows the true chest displacement waveform and its estimate using the ML estimator (Fig. 7.7a) and using the DML estimator (Fig. 7.7b). The latter follows the true displacement waveform accurately. For the ML estimates, the MAE is 1.34 mm and the RMSE is 1.77 mm. For the DML estimates, the MAE is 0.17 mm and the RMSE is 0.22 mm.

The estimated chest displacement waveform for the case of SNR = 0dB is depicted in Fig. 7.8. It is observed that neither MLE or DMLE can accurately reconstruct the displacement, although the pattern of the true chest displacement can still be observed from the

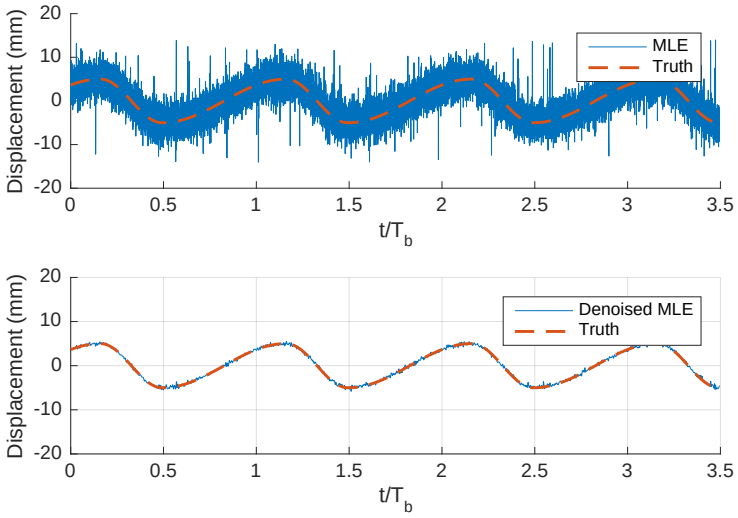


Figure 7.7: Displacement estimates with SNR = 6 dB. (a) Maximum likelihood displacement estimates. (b) Displacement estimates after denoising with EMD. The breathing displacement is simulated by concatenating two half cosines of different frequencies.

denoised waveform. The noisy MLE displacement is bounded because of phase wrapping in Eq (7.10). Although $M$ is selected so that $\theta_n$ is far away from $\pi$ or $-\pi$ as in Section 7.3.4, when the noise is large, $\phi_n$ can deviates away from the truth ($\theta_n$) so much that it wraps. For the ML estimates, the MAE is 3.59 mm and the RMSE is 4.91 mm. For the DML estimates, the MAE is 0.89 mm, and the RMSE is 1.09 mm.

Fig. 7.9 shows a different breathing waveform being accurately estimated by the proposed DMLE. Fig. 7.10 shows accurate estimation of a breathing pattern that exhibits a hypopnea event [119] from around the $5^{th}$ to around the $19^{th}$ breathing cycle. This demonstrates that the proposed method can recover an *arbitrary* displacement pattern.

The performance of the proposed methods for chest displacement due to heart beating during the absence of breathing is displayed in Fig. 7.11. This displacement is simulated based on the experimental measurements over the apex in [102]. In order to simulate the gradual changing of cardiac activity, we read the 10 values from the mean displacement curve at 10 phases along the R-R interval of ECG. In each cardiac cycle, zero-mean Gaussian noise samples are added to these values, and linear interpolation is performed to obtain

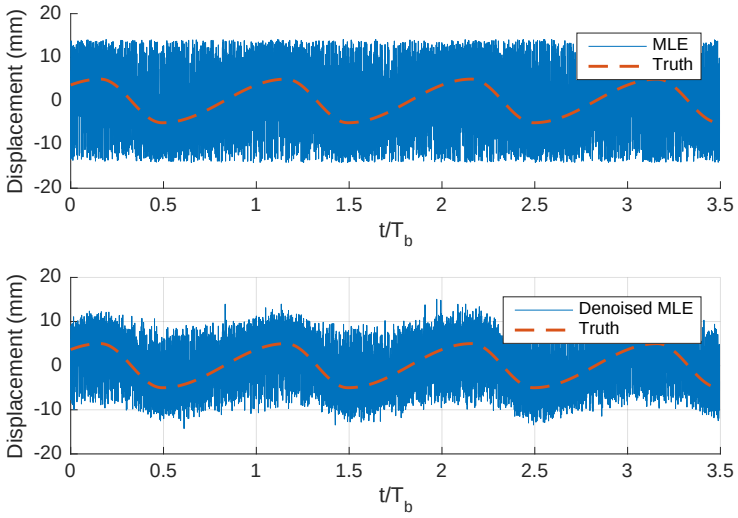


Figure 7.8: Displacement estimates with SNR = 0 dB. (a) Maximum likelihood displacement estimates. (b) Displacement estimates after denoising with EMD. The breathing displacement is simulated by concatenating two half cosines of different frequencies.

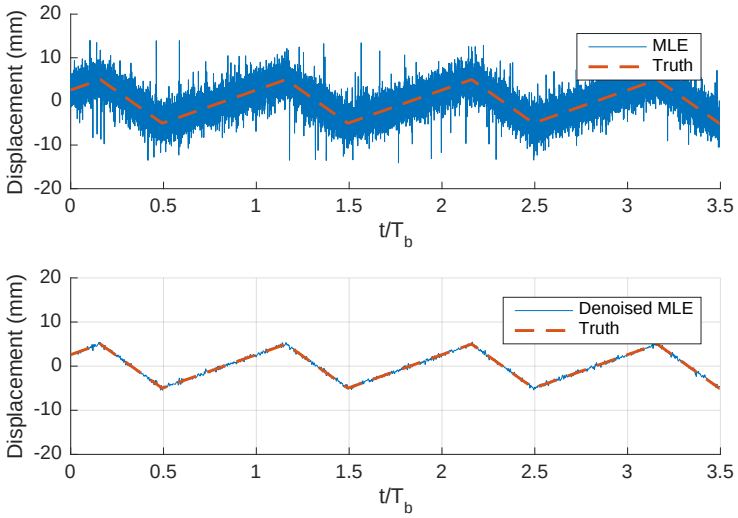


Figure 7.9: Displacement estimates with SNR = 6 dB. (a) Maximum likelihood displacement estimates. (b) Displacement estimates after denoising with EMD. The ground truth breathing displacement is simulated by concatenating triangles with sides of different slopes.

the displacement samples corresponding to every pulse repetition period. Heart rate variability [120] is also modeled by varying the heart beat period according to a Gaussian random process of mean 0.8 s and standard deviation 0.1 s. As expected, accurate estimation

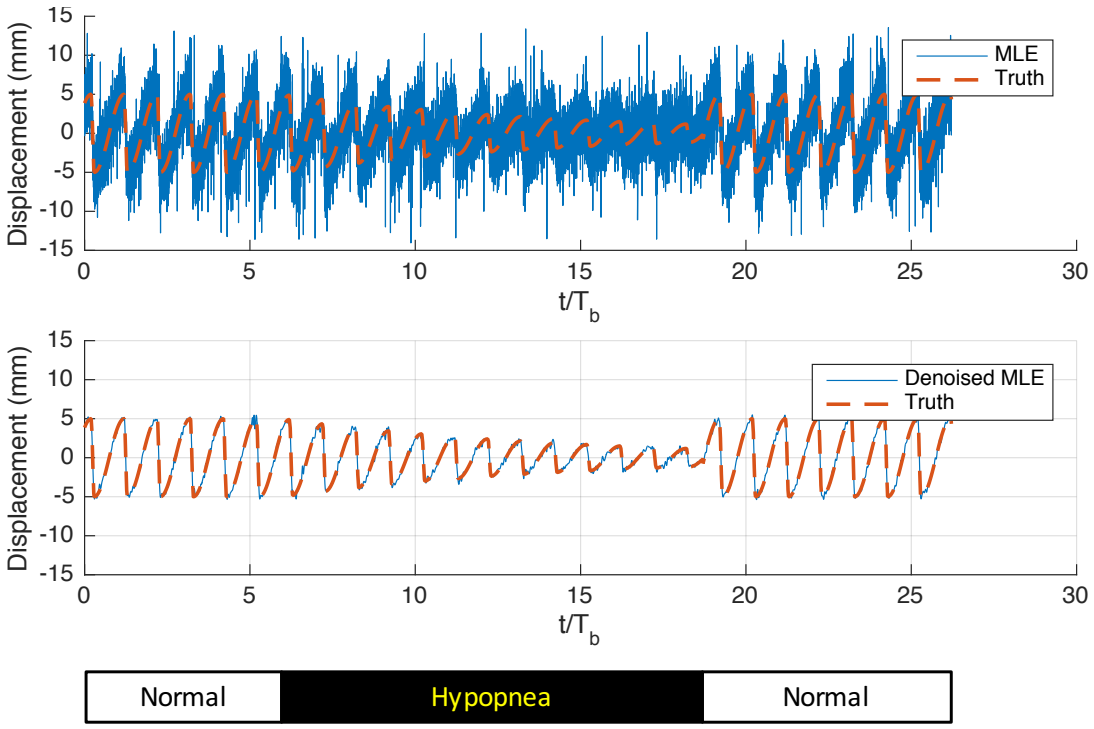


Figure 7.10: Estimate of a breathing pattern that exhibits a hypopnea event between two normal breathing events. (a) Maximum likelihood displacement estimates. (b) Displacement estimates after denoising with EMD.

of heartbeat-induced chest displacement needs a much higher SNR due to the much smaller displacement amplitude of the heart beating compared to that of breathing. The heart beats are discernible in the DMLE sequence, which is overlaid with the truth displacement in Fig. 7.11 or plotted alone in Fig. 7.12 for ease of viewing.

Fig. 7.13 plots the RMSE of the ML estimator and the CRLB (the square roots of two sides of (7.17)), and the RMSE of the DML estimator. A sequence of $N$ samples equally spaced over the range $[-7, 7]$ mm is used as the chest displacement sequence. The MSE values are averaged over 1000 random noise trials for each SNR value, before being taken square root of. As shown in Fig. 7.13, the ML estimator approaches the CRLB as SNR increases, and almost achieves the CRLB at SNR = 12 dB. It is also shown that denoising improves estimation accuracy for SNR greater than -3dB. For SNR = -3dB, the DML estimator produces the same estimates with those of MLE, hence the same RMSE

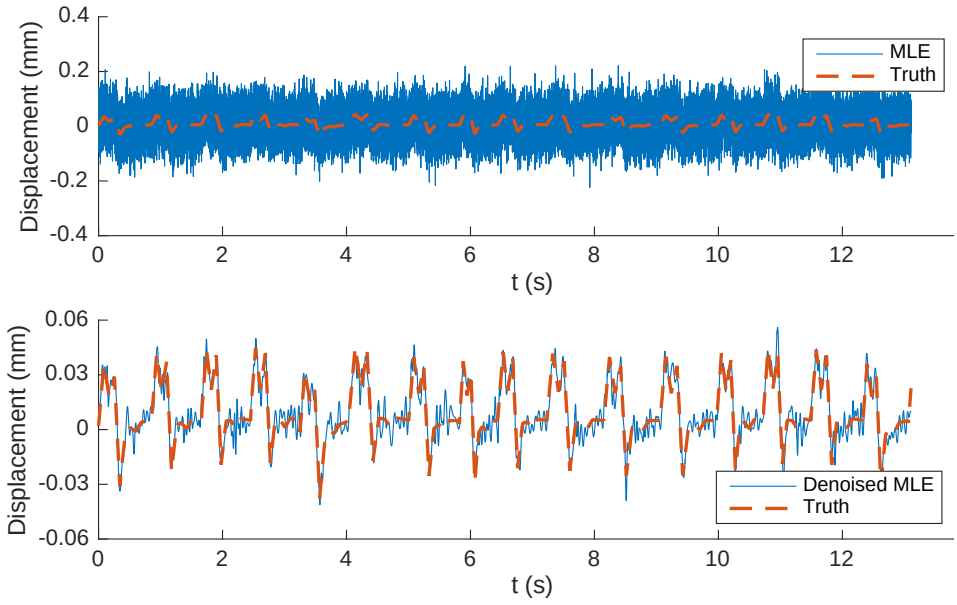


Figure 7.11: Estimate of a heartbeating-induced chest displacement during absence of breathing at SNR = 36dB. The mean cardiac cycle is 0.8 s. (a) MLE (b)DMLE

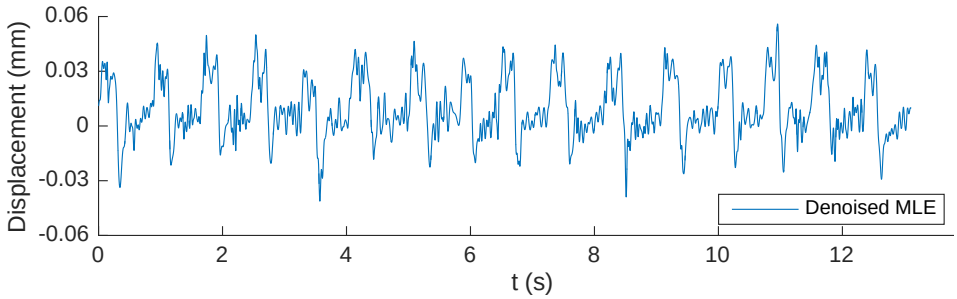


Figure 7.12: DML displacement estimate in Fig. 7.11

value on the plot. The RMSE curve of the DML estimator starts off higher than the CRLB, but strikingly gets below the CRLB at SNR $>$ 2 dB. This outperformance over the CRLB is justified, since the CRLB is associated with the ML estimator, not the DML estimator.

The CRLB of the ML estimator for a displacement time sample is given in Fig. 7.14. The displacement magnitude is selected to be from 0 to 7 mm, which is a practical range for the human chest displacement. It is observed that the bound becomes smaller as the displacement magnitude gets larger, although this relationship becomes less dramatic as the SNR increases.

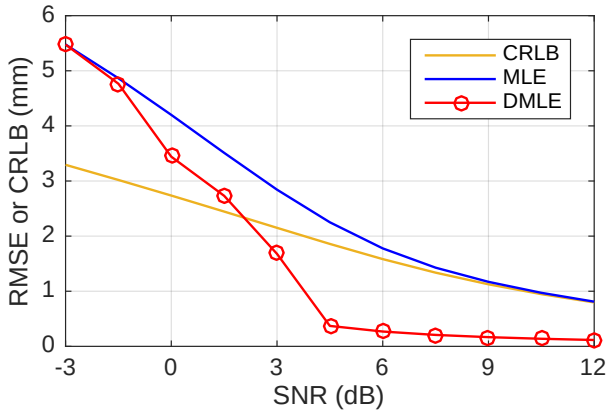


Figure 7.13: RMSE of the ML estimator and its associated CRLB, and RMSE of the DML estimator.

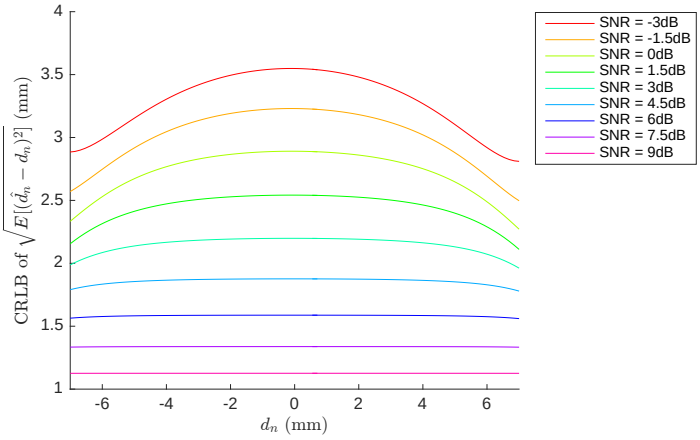


Figure 7.14: CRLB of the ML estimator of a displacement sample

## 7.5 Discussion

In the proposed MLE and DMLE methods, the required captured bandwidth is as small as $f_r$, whose practical values are in the order of kHz, thus there is no need to capture the whole bandwidth of the UWB pulse, which is in the order of GHz. Benefits include significant reduction of sampling rate by several orders of magnitude and of in-band noise.

## 7.6 Conclusion

In this chapter, a novel denoised ML (DML) estimator for estimation of the chest displacement from only a fraction of an IR-UWB radar received spectrum has been proposed. The method comprises of an ML estimator followed by denoising to further improve estimation accuracy. The ML displacement estimator is shown to be a biased estimator. The Cramér-Rao lower bound for the MLE has been derived.

Simulation studies are performed to evaluate the performance of the ML and DML approaches. Realistic simulated chest displacement due to normal and obstructed breathing, and due to heart beating in the absence of respiration can be accurately reconstructed by the proposed method. The ML estimator is observed to approach the bound as SNR increases. Strikingly, the DML estimator is shown to outperform this bound for sufficient SNR.

Significant advantages of the proposed approach over the commonly used correlation method includes (1) that only a fraction of the UWB spectrum is needed and (2) significantly lower computational complexity. Specifically, the computational complexity of the DML estimator is equal to that of a DFT, or that of the denoising method such as empirical mode decomposition, whichever larger. When empirical mode decomposition is used for denoising, the complexity is that of a DFT.

A topic of future work is to combine multiple spectral clusters to improve estimation accuracy.

# CHAPTER 8

# CONCLUSIONS AND SUGGESTED FUTURE WORKS

In this dissertation, the use of Impulse Radio Ultrawideband (IR-UWB) radar on non-contact sensing of physiological parameters has been investigated. The research brings several contributions into the field, ranging from analytical modeling to algorithm development, with more emphasis on the latter. In the analytical modeling part, a model for the radar received signal spectrum has been proposed. In the algorithm development part, algorithms for estimating a range of physiological parameters from the chest-reflected radar received signal have been developed.

In the theoretical analysis part of the thesis, a generic spectral model of the chest-reflected IR-UWB radar signal due to arbitrary periodic heart and lungs motion is derived. This spectrum model, which analyzes the continuous signal as it arrives at the receive antenna, distinguishes itself from previous works whose models are for only an undersampled version of this signal. In other words, we provide an unaliased spectrum model, in contrast to the previous aliased models. Closed-form expressions of both the complex amplitude and frequency of each spectral component are provided. Our analysis shows that the received spectrum has spectral components located at multiples of the respiration rate (RR), multiples of the heart rate (HR), multiples of the burst repetition frequency, and their intermodulation products. Although the analysis is done assuming only a planar air-skin interface, extension to a multi-layered planar thorax model is straightforward through superposition.

For the sum-of-two-sinusoids chest displacement model, the spectrum has a clustered structure with great sparsity, where each cluster is centered at a multiple of the burst repetition frequency and contains only a few significant components. The relative amplitudes of the components within a cluster are shown to vary significantly from cluster to cluster over

the UWB band of 3 to 10 GHz and are a function of maximum chest displacement. This is not a trivial dependence for the type of delay modulation inherent in the IR-UWB radar received signal. The previously reported aliased spectrum is shown to differ significantly from the unaliased spectrum presented in this dissertation. Practicality and usage of our analytical model is discussed in terms of the number of significant terms and numerical precision.

The presented model has several advantages over just using the CTFT. The CTFT expression does not reveal the locations of spectral components nor, because of the nonlinear nature of delay modulation, does it clarify how a particular sinusoidal component of the displacement function contributes to the spectrum. However, a limitation of our model is that the total number of multiplications in our model will exceed that of the CTFT for more complex displacement functions.

In the algorithm development part, various methods have been designed to estimate a range of physiological parameters of clinical significance. These include HR, RR, cardiopulmonary chest wall displacement waveform, body macro movement level, and posture change.

Several algorithms have been proposed for estimation of HR and RR. While RR is relatively easy to detect, the HR estimation is challenging due to low signal-to-noise-and-interference ratio (SINR). Two novel low-complexity algorithms, HAPA and SHAPA, have been proposed for HR estimation. These two methods utilize harmonics to improve or provide the estimation of the fundamental frequency, which may be otherwise not possible, e.g. when the fundamental is missing or has peak location error due to interference. Experimental results show that the proposed methods significantly outperform the highest-peak selection method, a common approach that suffers when the heart and respiration components interfere. Specifically, HAPA and SHAPA can provide an accurate HR estimate even when the HR fundamental is missing or has high peak location error due to leakage from nearby RR harmonics. The SHAPA algorithm is an enhancement of the HAPA algorithm,

incorporating information from the previous spectra when the fundamental or harmonics are masked by noise. SHAPA produces errors that are comparable to HAPA, which does not utilize the previous spectra. The most notable improvement of SHAPA over HAPA is in terms of the 16% to 60% increase in the number of valid estimates. These algorithms can also improve RR estimates and are practical for a real-time IR-UWB radar system.

The above algorithms, although are able to obtain noticeable improvement over the commonly used highest-peak selection method, have several limitations. These include lack of systematic tracking and motion artifacts removal. To overcome these limitations, a novel HR estimation algorithm that leverages sequential Bayesian tracking, HR harmonics, RR harmonics, and motion artifact removal is proposed. A score feature that takes into account the interference from respiration harmonics onto the heart signal is proposed. The score feature, which defines the observation, is specifically designed to avoid mistakenly selecting an RR harmonic as the HR estimate, yet still be able to recognize an HR at or near an RR harmonic by incorporating the powers of the HR higher harmonics. The state-transition and likelihood models are data-driven, and the required density functions are learned through a training phase. In order to determine the generality of the algorithm on unseen data, i.e., in production state, a cross-validation method is applied for performance evaluation. The algorithm is evaluated with real-world experimental data from the largest reported number of subjects of different genders and ages. The experimental results show that the presented algorithm has successfully integrated the Bayesian framework into the HR estimation problem from the highly-interfered, low SNR chest-reflected signal obtained from the non-contact IR-UWB radar.

Compared to HR and RR alone, the chest wall displacement due to respiratory and cardiac activities could give more information on cardiopulmonary disorders. A key contribution of this dissertation is a novel method that estimates the chest displacement waveform from only a fraction of an IR-UWB radar received spectrum. The estimator, called Denoised Maximum Likelihood (DML) estimator, consists of the ML displacement estimator

followed by denoising. In this dissertation, empirical mode decomposition is chosen to be the denoising method, but other denoising methods such as Independent Component Analysis is also applicable. The ML displacement estimator is shown to be a biased estimator, and its Cramér-Rao lower bound (CRLB) is derived. Simulation studies are conducted to evaluate the performance of the ML and DML estimators. Realistic simulated waveforms of chest displacement due to normal and obstructed breathing, and due to heart beating in the absence of respiration are shown to be accurately reconstructed by the DML method. The ML estimator is observed to approach its CRLB as SNR increases. Strikingly, the DML estimator is observed to outperform this bound for sufficient SNR. Significant advantages of the proposed approach over the commonly used correlation method includes (1) that only a fraction of the UWB spectrum is needed and (2) significantly lower computational complexity. Specifically, the computational complexity of the DML estimator is equal to that of a DFT, or that of the denoising method, whichever larger. When empirical mode decomposition is used for denoising, the complexity of the DML estimator is that of a DFT.

Another algorithm development problem addressed is the quantification of body macro movements and detection of posture change from the chest-reflected UWB radar signal. Our proposed algorithm assigns a score value to each motion event and also utilizes signal statistics to determine if a motion event has caused a posture change. Motion detection is based on amplitude thresholding in both the heart and respiration signal channels. Posture change detection is formulated as a hypothesis test problem, where the detection threshold is obtained based on signal statistics. Performance metrics in terms of detection probability and false alarm rate are evaluated with experimental data from human subjects that performed a series of arm movements and turns. The accuracy of posture change determined by the algorithm is 88.9%. Howevever, the false alarm rate is 26.7%, which is relatively high.

In the following, a list of possible directions for future research is presented.

1. In the HR estimation algorithm based on sequential Bayesian filtering, the RR is treated as a nuisance parameter and is estimated using the highest peak method. Joint tracking of HR and RR using sequential Bayesian filtering will potentially improve estimation accuracy for both HR and RR. Improvement is also obtainable by finding better features and improving the likelihood model.

2. Currently, the DML pattern estimator only utilizes a particular cluster in the received spectrum. As shown in the theoretical analysis part of the thesis, the complex amplitudes of the spectral components in each cluster are functions of the Fourier series coefficients of the displacement waveform. Thus, there is duplicate information about the displacement across clusters. Consequently, leveraging signal from multiple clusters will improve estimation accuracy. Further accuracy improvement could also be obtained with ensemble EMD [121], which has been shown to be an improvement of the conventional EMD.

3. The reported detection probability and false alarm rate of the posture change detector are evaluated from only six subjects. A larger number of subjects will be better for determining the detection threshold and make the performance less sensitive to the choice of parameter values.

4. Estimation of IER from the time variation pattern of RR harmonics power is an open problem.

## REFERENCES


[1] L. Rose and S. P. Clarke, "Signs," *The American Journal of Nursing*, vol. 110, no. 5, p. 11, 2010.

[2] C. H. Lund and J. A. Tucker, "Adhesion and newborn skin," *Neonatal Skin: Structure and Function. 2nd ed. New York, NY: Marcel Dekker*, pp. 299–324, 2003.

[3] FCC, "Revision of part 15 of the commissions rules regarding Ultrawideband transmission systems, first report and order," *ET Docket*, pp. 98–153, 2002.

[4] E. M. Staderini, "UWB radars in medicine," *IEEE Aerospace and Electronic Systems Magazine*, vol. 17, no. 1, pp. 13–18, 2002.

[5] S. Foo, *Ultra wideband monitoring systems and antennas*, US Patent 8,428,696, 2013.

[6] V. Nguyen, A. Q. Javaid, and M. A. Weitnauer, "Harmonic Path (HAPA) algorithm for non-contact vital signs monitoring with IR-UWB radar," in *IEEE Biomed. Cir. Sys. Conf. (BioCAS)*, 2013, pp. 146–149.

[7] ——, "Spectrum-averaged Harmonic Path (SHAPA) algorithm for non-contact vital sign monitoring with ultra-wideband (UWB) radar," in *IEEE Int. Conf. Eng. Medicine and Biology Society (EMBC)*, 2014, pp. 2241–2244.

[8] S. Venkatesh *et al.*, "Implementation and analysis of respiration-rate estimation using impulse-based UWB," in *IEEE Mil. Comm. Conf.*, 2005, pp. 3314–3320.

[9] A. Lazaro, D. Girbau, and R. Villarino, "Analysis of vital signs monitoring using an IR-UWB radar," *Progress In Electromagnetics Research*, vol. 100, pp. 265–284, 2010.

[10] M. Mabrouk *et al.*, "Model of human breathing reflected signal received by PN-UWB radar," in *IEEE Int. Conf. Eng. Medicine and Biology Society (EMBC)*, 2014, pp. 4559–4562.

[11] J. C. Lai *et al.*, "Wireless sensing of human respiratory parameters by low-power Ultrawideband impulse radio radar," *IEEE Trans. on Instrumentation and Measurement*, vol. 60, no. 3, pp. 928–938, 2011.

[12] V. Nguyen and M. A. Weitnauer, "UWB impulse radar for vital signs sensing - a modeling framework for arbitrary periodic heart and lung motion," in *IEEE Biomed. Circ. Sys. Conf. (BioCAS)*, 2015.

[13] G. Ossberger, T. Buchegger, E. Schimbäck, A. Stelzer, and R. Weigel, "Non-invasive respiratory movement detection and monitoring of hidden humans using ultra wideband pulse radar," in *Ultra Wideband Systems, 2004. Joint with Conference on Ultrawideband Systems and Technologies. Joint UWBST & IWUWBS. 2004 International Workshop on*, IEEE, 2004, pp. 395–399.

[14] M. Leib, W. Menzel, B. Schleicher, and H. Schumacher, "Vital signs monitoring with a uwb radar based on a correlation receiver," in *Antennas and Propagation (EuCAP), 2010 Proceedings of the Fourth European Conference on*, IEEE, 2010, pp. 1–5.

[15] M. Baldi, F. Chiaraluce, B. Zanaj, and M. Moretti, "Analysis and simulation of algorithms for vital signs detection using uwb radars," in *Ultra-Wideband (ICUWB), 2011 IEEE International Conference on*, IEEE, 2011, pp. 341–345.

[16] Y. Sun and N. Thakor, "Photoplethysmography revisited: From contact to noncontact, from point to imaging," *IEEE Tran. Biomed. Eng.*, vol. PP, no. 99, pp. 1–1, 2015.

[17] M.-Z. Poh, D. J. McDuff, and R. W. Picard, "Non-contact, automated cardiac pulse measurements using video imaging and blind source separation," *Optics express*, vol. 18, no. 10, pp. 10 762–10 774, 2010.

[18] H.-Y. Wu, M. Rubinstein, E. Shih, J. V. Guttag, F. Durand, and W. T. Freeman, "Eulerian video magnification for revealing subtle changes in the world.," *ACM Trans. Graph.*, vol. 31, no. 4, p. 65, 2012.

[19] Philips Vital Signs Camera, `http://www.vitalsignscamera.com/`.

[20] R.-Y. Huang and L.-R. Dung, "A motion-robust contactless photoplethysmography," in *IEEE Biomed. Cir. Sys. Conf. (BioCAS)*, 2015.

[21] Y. K. Lai and Y. Fu, *Method and system for reliable inspiration-to-expiration ratio extraction from acoustic physiological signal*, US Patent App. 12/800,932, 2010.

[22] O Postolache, P. Girao, G Postolache, and M Pereira, "Vital signs monitoring system based on emfi sensors and wavelet analysis," in *IEEE Instrumentation and Measurement Technology Conference Proceedings*, IEEE, 2007, pp. 1–4.

[23] W. SpillmanJr, M Mayer, J Bennett, J Gong, K. Meissner, B Davis, R. Claus, A. MuelenaerJr, and X Xu, "A'smart'bed for non-intrusive monitoring of patient physiological factors," *Measurement Science and Technology*, vol. 15, no. 8, p. 1614, 2004.

[24] I. Immoreev and T.-H. Tao, "Uwb radar for patient monitoring," *Aerospace and Electronic Systems Magazine, IEEE*, vol. 23, no. 11, pp. 11–18, 2008.

[25] M. Baldi, F. Appignani, B. Zanaj, and F. Chiaraluce, "Body movement compensation in UWB radars for respiration monitoring," in *Proc. IEEE First AESS Euro. Conf. on Satellite Telecomm., Italy*, 2012, pp. 2–5.

[26] J. P. Tupin Jr, J. P. Tupin, and S. Stephansen IV, *Fetal monitoring device and methods*, US Patent 9,078,582, 2015.

[27] A. V. Oppenheim and R. W. Schafer, *Discrete-time signal processing*. Pearson, 2010, pp. 153–163.

[28] J. Tu and J. Lin, "Respiration harmonics cancellation for accurate heart rate measurement in non-contact vital sign detection," in *Microwave Symposium Digest (IMS), 2013 IEEE MTT-S International*, IEEE, 2013, pp. 1–3.

[29] ——, "Fast acquisition of heart rate in noncontact vital sign radar measurement using time-window-variation technique," *Instrumentation and Measurement, IEEE Transactions on*, vol. 65, no. 1, pp. 112–122, 2016.

[30] L. Anitori, A. de Jong, and F. Nennie, "Fmcw radar for life-sign detection," in *Radar Conference, 2009 IEEE*, IEEE, 2009, pp. 1–6.

[31] M. Baboli, A. Sharafi, A. Ahmadian, and M. Nambakhsh, "An accurate and robust algorithm for detection of heart and respiration rates using an impulse based uwb signal," in *Biomedical and Pharmaceutical Engineering, 2009. ICBPE'09. International Conference on*, IEEE, 2009, pp. 1–4.

[32] A. Sharafi, M. Baboli, and M. Eshghi, "A new algorithm for detection motion rate based on energy in frequency domain using UWB signals," in *Bioinformatics and Biomedical Engineering (iCBBE), 2010 4th International Conference on*, IEEE, 2010, pp. 1–4.

[33] F. J. Harris, "On the use of windows for harmonic analysis with the discrete fourier transform," *Proceedings of the IEEE*, vol. 66, no. 1, pp. 51–83, 1978.

[34] M. R. Schroeder, "Period histogram and product spectrum: New methods for fundamental-frequency measurement," *The Journal of the Acoustical Society of America*, vol. 43, no. 4, pp. 829–834, 1968.

[35] P. J. Walmsley, "Signal separation of musical instruments," *Signal Processing Group, Department of Engineering, University of Cambridge*, 2000.

[36] S. Kim, L. Holmstrom, and J. McNames, "Multiharmonic tracking using marginalized particle filters," in *Engineering in Medicine and Biology Society, 2008. EMBS 2008. 30th Annual International Conference of the IEEE*, IEEE, 2008, pp. 29–33.

[37] S. Edla, N. Kovvali, and A. Papandreou-Suppappola, "Electrocardiogram signal modeling with adaptive parameter estimation using sequential bayesian methods," *Signal Processing, IEEE Transactions on*, vol. 62, no. 10, pp. 2667–2680, 2014.

[38] S. Kim, L. Holmstrom, and J. McNames, "Tracking of rhythmical biomedical signals using the maximum a posteriori adaptive marginalized particle filter," *British Journal of Health Informatics and Monitoring*, vol. 2, no. 1, 2015.

[39] M. Boloursaz Mashhadi, E. Asadi, M. Eskandari, S. Kiani, and F. Marvasti, "Heart rate tracking using wrist-type photoplethysmographic (ppg) signals during physical exercise with simultaneous accelerometry," *IEEE Signal Processing Letters*, vol. 23, no. 2, pp. 227–231, 2016.

[40] Z. Zhang, Z. Pi, and B. Liu, "Troika: A general framework for heart rate monitoring using wrist-type photoplethysmographic signals during intensive physical exercise," *IEEE Transactions on Biomedical Engineering*, vol. 62, no. 2, pp. 522–531, 2015.

[41] Z. Zhang, "Photoplethysmography-based heart rate monitoring in physical activities via joint sparse spectrum reconstruction," *IEEE Transactions on Biomedical Engineering*, vol. 62, no. 8, pp. 1902–1910, 2015.

[42] N. K. Lakshminarasimha Murthy, P. C. Madhusudana, P. Suresha, V. Periyasamy, and P. K. Ghosh, "Multiple spectral peak tracking for heart rate monitoring from photoplethysmography signal during intensive physical exercise," *IEEE Signal Processing Letters*, vol. 22, no. 12, pp. 2391–2395, 2015.

[43] S. F. Cotter, B. D. Rao, K. Engan, and K. Kreutz-Delgado, "Sparse solutions to linear inverse problems with multiple measurement vectors," *IEEE Transactions on Signal Processing*, vol. 53, no. 7, pp. 2477–2488, 2005.

[44] `https://www.physionet.org/`.

[45] M. Baboli, O. Boric-Lubecke, and V. Lubecke, "A new algorithm for detection of heart and respiration rate with UWB signals," in *Engineering in Medicine and Biology Society (EMBC), 2012 Annual International Conference of the IEEE*, IEEE, 2012, pp. 3947–3950.

[46] R. Kohavi *et al.*, "A study of cross-validation and bootstrap for accuracy estimation and model selection," in *Ijcai*, vol. 14, 1995, pp. 1137–1145.

[47] M. Muller and G. I. Abib, "Ultra wideband radar system for human chest displacement," in *New Circuits and Systems Conference (NEWCAS), 2015 IEEE 13th International*, IEEE, 2015, pp. 1–4.

[48] M. Reddy, S. S. Gill, and P. A. Rochon, "Preventing pressure ulcers: A systematic review," *Jama*, vol. 296, no. 8, pp. 974–984, 2006.

[49] D. Bluestein and A. Javaheri, "Pressure ulcers: Prevention, evaluation, and management.," *American family physician*, vol. 78, no. 10, 2008.

[50] J. J. Liu *et al.*, "Sleep posture analysis using a dense pressure sensitive bedsheet," *Pervasive and Mobile Computing*, vol. 10, pp. 34–50, 2014.

[51] W.-Y. Chang, C.-C. Chen, C.-C. Chang, and C.-L. Yang, "An enhanced sensing application based on a flexible projected capacitive-sensing mattress," *Sensors*, vol. 14, no. 4, pp. 6922–6937, 2014.

[52] R Yousefi *et al.*, "Bed posture classification for pressure ulcer prevention," in *IEEE Int. Conf. Eng. Med. Bio.*, 2011.

[53] C. Hsia *et al.*, "Analysis and comparison of sleeping posture classification methods using pressure sensitive bed system," in *IEEE Int. Conf. Eng. Med. Bio.*, 2009, pp. 6131–6134.

[54] H. Yoon *et al.*, "Estimation of sleep posture using a patch-type accelerometer based device," in *IEEE Int. Conf. Eng. Med. Bio.*, IEEE, 2015, pp. 4942–4945.

[55] K.-M. Chang and S.-H. Liu, "Wireless portable electrocardiogram and a tri-axis accelerometer implementation and application on sleep activity monitoring," *Telemedicine and e-Health*, vol. 17, no. 3, pp. 177–184, 2011.

[56] T. Pawar, N. Anantakrishnan, S. Chaudhuri, and S. P. Duttagupta, "Transition detection in body movement activities for wearable ecg," *IEEE Trans. Biomed. Eng.*, vol. 54, no. 6, pp. 1149–1152, 2007.

[57] H. J. Lee *et al.*, "Estimation of body postures on bed using unconstrained ECG measurements," *IEEE J. Biomedical and Health Informatics*, vol. 17, no. 6, pp. 985–993, 2013.

[58] F. Khan, J. W. Choi, and S. H. Cho, "Vital sign monitoring of a non-stationary human through ir-uwb radar," in *Network Infrastructure and Digital Content (IC-NIDC), 2014 4th IEEE International Conference on*, IEEE, 2014, pp. 511–514.

[59] K. Ota, Y. Ota, M. Otsu, and A. Kajiwara, "Elderly-care motion sensor using uwb-ir," in *Sensors Applications Symposium (SAS), 2011 IEEE*, IEEE, 2011, pp. 159–162.

[60] X. Li, D. Qiao, and Y. Li, "An analytical model for regular respiratory signal," in *IEEE Int. Conf. Eng. Medicine and Biology Society (EMBC)*, 2014, pp. 102–105.

[61] Y. Lai and Y. Fu, *Method and system for reliable inspiration-to-expiration ratio extraction from acoustic physiological signal*, US Patent App. 12/800,932, 2011.

[62] K. Matsuo, K. M. Hiiemae, M. Gonzalez-Fernandez, and J. B. Palmer, "Respiration during feeding on solid food: Alterations in breathing during mastication, pharyngeal bolus aggregation, and swallowing," *Journal of Applied Physiology*, vol. 104, no. 3, pp. 674–681, 2008.

[63] K. Pandia, O. T. Inan, G. T. Kovacs, and L. Giovangrandi, "Extracting respiratory information from seismocardiogram signals acquired on the chest using a miniature accelerometer," *Physiological measurement*, vol. 33, no. 10, p. 1643, 2012.

[64] W. B. Thompson, M. B. Rappaport, and H. B. Sprague, "Ballistocardiography ii. the normal ballistocardiogram," *Circulation*, vol. 7, no. 3, pp. 321–328, 1953.

[65] E. M. Staderini and G. Varotto, "Optimization criteria in the design of medical UWB radars in compliance with the regulatory masks," in *IEEE Biomed. Circ. Sys. Conf. (BioCAS)*, 2007, pp. 53–58.

[66] A. Christ, A. Klingenbock, T. Samaras, C. Goiceanu, and N. Kuster, "The dependence of electromagnetic far-field absorption on body tissue composition in the frequency range from 300 mhz to 6 ghz," *IEEE Trans. Microwave Theory and Techniques*, vol. 54, no. 5, pp. 2188–2195, 2006.

[67] G. Varotto and E. M. Staderini, "On the UWB medical radars working principles," *International Journal of Ultra Wideband Communications and Systems*, vol. 2, no. 2, pp. 83–93, 2011.

[68] B. Hu and N. C. Beaulieu, "Pulse shapes for ultrawideband communication systems," *IEEE Transactions on wireless communications*, vol. 4, no. 4, pp. 1789–1797, 2005.

[69] J. R. Barry, E. A. Lee, and D. G. Messerschmitt, *Digital communication*. Springer Science & Business Media, 2004.

[70] W. Z. Li, Z. Li, H. Lv, G. Lu, Y. Zhang, X. Jing, S. Li, and J. Wang, "A new method for non-line-of-sight vital sign monitoring based on developed adaptive line enhancer using low centre frequency UWB radar," *Progress In Electromagnetics Research*, vol. 133, pp. 535–554, 2013.

[71] Y. Xu, S. Dai, S. Wu, J. Chen, and G. Fang, "Vital sign detection method based on multiple higher order cumulant for ultrawideband radar," *IEEE Transactions on Geoscience and Remote Sensing*, vol. 50, no. 4, pp. 1254–1265, 2012.

[72] I. Y. Immoreev, "Practical applications of uwb technology," *IEEE Aerospace and Electronic Systems Magazine*, vol. 25, no. 2, pp. 36–42, 2010.

[73] C.-H. Hsieh, Y.-F. Chiu, Y.-H. Shen, T.-S. Chu, and Y.-H. Huang, "A uwb radar signal processing platform for real-time human respiratory feature extraction based on four-segment linear waveform model," *IEEE Transactions on Biomedical Circuits and Systems*, vol. 10, no. 1, pp. 219–230, 2016.

[74] E. Pittella, S. Pisa, and M. Cavagnaro, "Breath activity monitoring with wearable uwb radars: Measurement and analysis of the pulses reflected by the human body," 2015.

[75] M. S. Arulampalam, S. Maskell, N. Gordon, and T. Clapp, "A tutorial on particle filters for online nonlinear/non-gaussian bayesian tracking," *Signal Processing, IEEE Transactions on*, vol. 50, no. 2, pp. 174–188, 2002.

[76] R. E. Kalman, "A new approach to linear filtering and prediction problems," *Journal of basic Engineering*, vol. 82, no. 1, pp. 35–45, 1960.

[77] B. S. Kim and S. K. Yoo, "Motion artifact reduction in photoplethysmography using independent component analysis," *IEEE Transactions on Biomedical Engineering*, vol. 53, no. 3, pp. 566–568, 2006.

[78] D. E. Goldberg, *Genetic algorithms*. Pearson Education India, 2006.

[79] C. M. Bishop, "Pattern recognition," *Machine Learning*, 2006.

[80] B. Ripley, "Pattern recognition and neural networks," 1996.

[81] L. Ren, Y. S. Koo, H. Wang, Y. Wang, Q. Liu, and A. E. Fathy, "Noncontact multiple heartbeats detection and subject localization using uwb impulse doppler radar," *IEEE Microwave and Wireless Components Letters*, vol. 25, no. 10, pp. 690–692, 2015.

[82] M. Chia, S. Leong, C. Sim, and K. Chan, "Through-wall uwb radar operating within fcc's mask for sensing heart beat and breathing rate," in *European Radar Conference, 2005. EURAD 2005.*, IEEE, 2005, pp. 267–270.

[83] B. Schleicher, I. Nasr, A. Trasser, and H. Schumacher, "Ir-uwb radar demonstrator for ultra-fine movement detection and vital-sign monitoring," *IEEE transactions on microwave theory and techniques*, vol. 61, no. 5, pp. 2076–2085, 2013.

[84] Y. Xu, S. Wu, C. Chen, J. Chen, and G. Fang, "A novel method for automatic detection of trapped victims by ultrawideband radar," *IEEE Transactions on Geoscience and Remote Sensing*, vol. 50, no. 8, pp. 3132–3142, 2012.

[85] I. Y. Immoreev, "Practical application of ultra-wideband radars," *Ultrawideband and Ultrashort Impulse Signals*, pp. 18–22, 2006.

[86] A. Q. Javaid, C. M. Noble, R. Rosenberg, and M. A. Weitnauer, "Towards sleep apnea screening with an under-the-mattress IR-UWB radar using machine learning," in *IEEE 14th Int. Conf. Machine Learning and Applications*, 2015, pp. 837–842.

[87] R. B. Berry, R. Budhiraja, D. J. Gottlieb, D. Gozal, C. Iber, V. K. Kapur, C. L. Marcus, R. Mehra, S. Parthasarathy, S. F. Quan, *et al.*, "Rules for scoring respiratory events in sleep: Update of the 2007 aasm manual for the scoring of sleep and associated events," *J Clin Sleep Med*, vol. 8, no. 5, pp. 597–619, 2012.

[88] R. B. Berry, R. Brooks, C. E. Gamaldo, S. M. Harding, C. Marcus, and B. Vaughn, "The aasm manual for the scoring of sleep and associated events," *Rules, Termi-*

*nology and Technical Specifications, Darien, Illinois, American Academy of Sleep Medicine*, 2012.

[89] K. Konno and J. Mead, "Measurement of the separate volume changes of rib cage and abdomen during breathing," *Journal of Applied Physiology*, vol. 22, no. 3, pp. 407–422, 1967.

[90] T Kondo, T Uhlig, P Pemberton, and P. Sly, "Laser monitoring of chest wall displacement," *European Respiratory Journal*, vol. 10, no. 8, pp. 1865–1869, 1997.

[91] W. Massagram, N. Hafner, V. Lubecke, and O. Boric-Lubecke, "Tidal volume measurement through non-contact doppler radar with dc reconstruction," *IEEE Sensors Journal*, vol. 13, no. 9, pp. 3397–3404, 2013.

[92] M. Zakrzewski, A. Vehkaoja, A. S. Joutsen, K. T. Palovuori, and J. J. Vanhala, "Noncontact respiration monitoring during sleep with microwave doppler radar," *IEEE Sensors Journal*, vol. 15, no. 10, pp. 5683–5693, 2015.

[93] Y. S. Lee, P. N. Pathirana, C. L. Steinfort, and T. Caelli, "Monitoring and analysis of respiratory patterns using microwave doppler radar," *IEEE journal of translational engineering in health and medicine*, vol. 2, pp. 1–12, 2014.

[94] M. Norgia and S. Donati, "A displacement-measuring instrument utilizing self-mixing interferometry," *IEEE Transactions on Instrumentation and Measurement*, vol. 52, no. 6, pp. 1765–1770, 2003.

[95] I. Milesi, M. Norgia, P. P. Pompilio, C. Svelto, and R. L. Dellaca, "Measurement of local chest wall displacement by a custom self-mixing laser interferometer," *IEEE Transactions on Instrumentation and Measurement*, vol. 60, no. 8, pp. 2894–2901, 2011.

[96] B.-K. Park, O. Boric-Lubecke, and V. M. Lubecke, "Arctangent demodulation with dc offset compensation in quadrature doppler radar receiver systems," *IEEE Transactions on Microwave Theory and Techniques*, vol. 55, no. 5, pp. 1073–1079, 2007.

[97] X. Gao, A. Singh, E. Yavari, V. Lubecke, and O. Boric-Lubecke, "Non-contact displacement estimation using doppler radar," in *Annual International Conference of the IEEE Engineering in Medicine and Biology Society*, IEEE, 2012, pp. 1602–1605.

[98] W. Hu, Z. Zhao, Y. Wang, H. Zhang, and F. Lin, "Noncontact accurate measurement of cardiopulmonary activity using a compact quadrature doppler radar sensor," *IEEE Transactions on Biomedical Engineering*, vol. 61, no. 3, pp. 725–735, 2014.

[99] Z. Wu and N. E. Huang, "Ensemble empirical mode decomposition: A noise-assisted data analysis method," *Advances in adaptive data analysis*, vol. 1, no. 01, pp. 1–41, 2009.

[100] S. Guan, J. A. Rice, C. Li, and C. Gu, "Automated dc offset calibration strategy for structural health monitoring based on portable cw radar sensor," *IEEE Transactions on Instrumentation and Measurement*, vol. 63, no. 12, pp. 3111–3118, 2014.

[101] M. Zakrzewski, H. Raittinen, and J. Vanhala, "Comparison of center estimation algorithms for heart and respiration monitoring with microwave doppler radar," *IEEE Sensors Journal*, vol. 12, no. 3, pp. 627–634, 2012.

[102] G Ramachandran, S Swarnamani, and M Singh, "Reconstruction of out-of-plane cardiac displacement patterns as observed on the chest wall during various phases of ecg by capacitance transducer," *IEEE transactions on biomedical engineering*, vol. 38, no. 4, pp. 383–385, 1991.

[103] R. Vas, C. R. Joyner, D. E. Pittman, and T. C. Gay, "The displacement cardiograph," *IEEE Transactions on Biomedical Engineering*, no. 1, pp. 49–54, 1976.

[104] M. Okada, T. Nakajima, N. Eizuka, Y. Saitoh, and M. Yakata, "Isochronal map of chest wall vibration with cardiokymography," *Computer methods and Programs in Biomedicine*, vol. 26, no. 2, pp. 105–113, 1988.

[105] A Periasamy and M. Singh, "Reconstruction of cardiac displacement patterns on the chest wall by laser speckle interferometry," *IEEE transactions on medical imaging*, vol. 4, no. 1, pp. 52–57, 1985.

[106] G Ramachandran and M Singh, "Three-dimensional reconstruction of cardiac displacement patterns on the chest wall during the p, qrs and t-segments of the ecg by laser speckle inteferometry," *Medical and Biological Engineering and Computing*, vol. 27, no. 5, pp. 525–530, 1989.

[107] M. Singh and G Ramachandran, "Reconstruction of sequential cardiac in-plane displacement patterns on the chest wall by laser speckle interferometry," *IEEE transactions on biomedical engineering*, vol. 38, no. 5, pp. 483–489, 1991.

[108] Y. Nijsure, W. P. Tay, E. Gunawan, F. Wen, Z. Yang, Y. L. Guan, and A. P. Chua, "An impulse radio ultrawideband system for contactless noninvasive respiratory monitoring," *IEEE Transactions on Biomedical Engineering*, vol. 60, no. 6, pp. 1509–1517, 2013.

[109] M. Leib, E. Schmitt, E. Gronau, J. Dederer, B. Schleicher, H. Schumacher, and W. Menzel, "A compact ultra-wideband radar for medical applications," *Frequenz*, vol. 63, no. 1, p. 2, 2009.

[110] J. Li and R. Wu, "An efficient algorithm for time delay estimation," *IEEE Transactions on Signal Processing*, vol. 46, no. 8, pp. 2231–2235, 1998.

[111] J Zhang, R. A. Kennedy, and T. D. Abhayapala, "Cramer-rao lower bounds for the time delay estimation of uwb signals," in *IEEE International Conference on Communications*, IEEE, vol. 6, 2004, pp. 3424–3428.

[112] S. Gezici, "Theoretical limits for estimation of periodic movements in pulse-based uwb systems," *IEEE Journal of Selected Topics in Signal Processing*, vol. 1, no. 3, pp. 405–417, 2007.

[113] A. Hyvärinen, J. Karhunen, and E. Oja, *Independent component analysis*. John Wiley & Sons, 2004, vol. 46.

[114] Y.-H. Wang, C.-H. Yeh, H.-W. V. Young, K. Hu, and M.-T. Lo, "On the computational complexity of the empirical mode decomposition algorithm," *Physica A: Statistical Mechanics and its Applications*, vol. 400, pp. 159–167, 2014.

[115] N. E. Huang, Z. Shen, S. R. Long, M. C. Wu, H. H. Shih, Q. Zheng, N.-C. Yen, C. C. Tung, and H. H. Liu, "The empirical mode decomposition and the hilbert spectrum for nonlinear and non-stationary time series analysis," in *Proceedings of the Royal Society of London A: Mathematical, Physical and Engineering Sciences*, The Royal Society, vol. 454, 1998, pp. 903–995.

[116] D. Rife and R. Boorstyn, "Single tone parameter estimation from discrete-time observations," *IEEE Transactions on information theory*, vol. 20, no. 5, pp. 591–598, 1974.

[117] P. Dharmawansa, N. Rajatheva, and C. Tellambura, "Envelope and phase distribution of two correlated gaussian variables," *IEEE Transactions on Communications*, vol. 57, no. 4, pp. 915–921, 2009.

[118] Don H. Johnson, `www.ece.rice.edu/~dhj/courses/elec531/notes.pdf`.

[119] J. Durán, S. Esnaola, R. Rubio, and Á. Iztueta, "Obstructive sleep apnea–hypopnea and related clinical features in a population-based sample of subjects aged 30 to 70 yr," *American Journal of respiratory and critical care medicine*, vol. 163, no. 3, pp. 685–689, 2001.

[120] M. Malik, "Heart rate variability," *Annals of Noninvasive Electrocardiology*, vol. 1, no. 2, pp. 151–181, 1996.

[121] Z. Wu and N. E. Huang, “Ensemble empirical mode decomposition: A noise-assisted data analysis method,” *Advances in adaptive data analysis*, vol. 1, no. 01, pp. 1–41, 2009.